INTERNATIONAL DOCTORAL SCHOOL OF THE USC

Paula
Sánchez Gascón

PhD Thesis

IC-TAGGING SYSTEM: FROM PROTEIN TRACKING TO THERAPEUTIC APPLICATIONS.

Santiago de Compostela, 2025

Doctoral Programme in Molecular Medicine

ESCOLA DE DOUTORAMENTO
INTERNACIONAL DA USC

DOCTORAL THESIS

IC-TAGGING SYSTEM: FROM PROTEIN TRACKING TO THERAPEUTIC APPLICATIONS

Author
Paula Sánchez Gascón

Supervisors: José M. Martínez Costas, Natalia Barreiro Piñeiro
Tutor: José M. Martínez Costas

PHD PROGRAMME IN MOLECULAR MEDICINE
SANTIAGO DE COMPOSTELA
2025

ACKNOWLEDGMENTS / AGRADECIMIENTOS

Llegados a este punto toca echar la vista atrás y dejar constancia de que este pequeño libro no estaría en vuestras manos de no haber contado con el apoyo de muchas personas.

En primer lugar, quiero expresar mi más sincero agradecimiento a Jose, por haber dejado a una química inexperta adentrarse en su laboratorio. También por guiarme durante todos estos años y afrontar todos los proyectos con positividad. También a Natalia, por tu infinita paciencia desde el primer día y por enseñarme prácticamente todo lo que he aprendido en estos años en el laboratorio. Pero sobre todo por estar para mí siempre que lo he necesitado. A Rebe, por tener siempre una palabra amable y por toda tu ayuda con el cultivo celular. A Dani y Adri, por contribuir desde que llegasteis en tener un buen ambiente en el laboratorio. Y por último a Lisa, por sacar un momento para echarnos a todos una mano cuando lo necesitamos. Ha sido un placer trabajar con todos vosotros.

Thanks also to Sandra Diebold, for hosting me in your lab, and for introducing me in the world of immune-oncology. I have learned so much under your mentorship, and your insights have been truly invaluable. Also, a big thanks to the MHRA girls, Shreye, Dhyana and Federica, for those meetings outside the lab.

Fuera del laboratorio, pero no muy lejos, también he coincido con gente maravillosa. En el P3L5 he encontrado excelentes compañeros y amigos. Alberto, mi mitad aragonesa en Santiago. Ana, la mejor compañera de fiesta y confidente que he tenido en Santiago. También a Diego y a Carmen, empezamos juntos y terminamos juntos. Y no me olvido de Roi, Axel, David B. y David A. Gracias por formar parte de estos años.

Quisiera mencionar también a mis compañeros de despacho, ha sido una suerte poder compartir esta última etapa con vosotros. A Richi, por recibirme todos los días con tu abrazo diario. A Andy, por ser compañero de batallas nocturnas. También a Jose y a Sandra, por ser las personas más divertidas del despacho. A Zeko, mi gymbro del último mes. A mi recién incorporado primo Marcos, bienvenido a la familia. A Alex, Cinzia, Xuli, Mayra, Dani y Alba (aunque haya emigrado). Y a Giulia, que, aunque hace tiempo que te has ido, seguimos siendo buenas amigas. Gracias.

A Carla y a Maziu, que han estado conmigo desde el primer año en Santiago. Con vosotros he vivido muchos momentos que nunca olvidaré. Gracias por ser un pilar principal en esta etapa.

Tengo que reconocer que ha habido momentos en los que estar lejos de mi familia y amigos no ha sido fácil. Sin embargo, he podido encontrar en Santiago otra familia: Andrea y Alfonso. Con Andrea todo ha sido fácil, compartir piso, ser compañeras de shopping (siempre online) y sobre todo ser buenísimas amigas. No puedo imaginarme esta etapa sin ti. Y Alfonso, la persona que más me saca de quicio, pero también la que más me hace reír. Estos meses contigo en casa han sido un regalo. Os quiero mucho a los dos.

No me puedo olvidar de las principales responsables de que consiguiera acabar la carrera, Alejandra e Inés. Gracias por todos los momentos que hemos vivido, por vuestro apoyo y por tantos apuntes prestados. A Sergio y Gonzalo, o Gamba y Torrente, por hacer que Zaragoza se sintiera un hogar. A Sonia, por ser la mejor compañera de piso que tuve en todos los años en Zaragoza. Y a Mario, tus clases de matemáticas también tienen parte de responsabilidad en todo esto. También a mi amiga Patri, entre Teruel, Asturias y Praga, pero siempre unidas.

Gracias a mis amigas de Teruel, por hacerme sentir que no ha cambiado nada cada vez que nos vemos y por apoyarme incansablemente desde la lejanía.

A Fonso, por ser el mejor compañero de vida que he podido elegir. Gracias por tu paciencia infinita, tu cariño y por darme siempre el impulso que necesito. Una parte muy importante de esta tesis es tuya. También a tu familia y amigos, por haberme hecho sentir una más desde el primer momento.

Por ultimo, quiero agradecerle a mi familia el no haber permitido que me flaqueasen las fuerzas y por haber confiado ahora y siempre en que puedo conseguir todo lo que me proponga.

Después de escribir estas líneas, me quedo con la convicción de que el verdadero éxito de esta etapa no es otro que el de haber llegado hasta aquí tan bien rodeada.

Gracias a todos.

INDEX

ABBREVIATIONS

α1AT	α1-antitrypsin
Å	Amstrong
Ab	Antibody
ACE2	Angiotensin-Converting Enzyme 2
AHSV	African Horse Sickness Virus
APC	Antigen presenting cell
ARV	Avian Reovirus
B16 OVA cells	Murine tumor cell line model for human skin cancers
BiFC	Bimolecular Fluorescence Complementation Assay
BSA	Bovine Serum Albumin
BTV	Bluetongue Virus
CAR-T	Chimeric Antigen Receptor T-Cell
CD4+	T helper cell
CD8+	Cytolytic T Lymphocyte
CHO	Chinese Hamster Ovary
CSF	Colony Stimulation Factor
CTL	Cytotoxic T Lymphocyte
DAMP	Damage Associated Molecular Patterns
DAPI	4′,6-diamidino-2-phenylindole
DC	Dendritic Cell
DLS	Dynamic light scattering
DMEM	Dulbecco's Modified Eagle Medium
DMSO	Dimethyl sulfoxide
DNA	Desoxyribonucleic Acid
dNTP	Deoxynucleotide Triphosphates
dsRNA	Double-stranded RNA
E	Envelope protein of the SARS-CoV-2
EDS	Energy Dispersive X-ray Spectroscopy
EDTA	Ethylenediaminetetraacetic acid
EGFP	Enhanced GFP
EGFR	Epidermal Growth Factor Receptor
EHDV	Epizootic Hemorrhagic Disease Virus
ELISA	Enzyme-Linked Immunosorbent Assay
ER	Endoplasmic Reticulum
ERAD	ER- Associated Degradation
EU	Endotoxin Unit

FW	Forward
GFP	Green Fluorescent Protein
h	Hours
HB	Hypotonic Buffer
HBV	Hepatitis B virus
HC	Heavy Chain
HEK	Human Embryonic Kidney
HER2	Human Epidermal growth factor Receptor
HLC	Hairy Cell Leukemia
IC	Intercoil
IFN	Interferon
IFNAR-/-	Mice lacking the interferon alpha receptor
Ig	Immunoglobulin
IgG	Immunoglobulin G
IL	Interleukin
IPTG	Isopropyl β- d-1-thiogalactopyranoside
kb	kilobases
kDa	Kilodalton
KO	Knockout
LAL	Limulus Amoebocyte Lysate
LB	Luria Bertani
LC	Light Chain
Leu	Leucine
LPS	Lipopolysaccharide
LRR	Leucine-rich-repeat
M	Membrane protein of the SARS-CoV-2
MAT	Monocyte Activation Test
MHC	Major Histocompatibility Complex
MHRA	Medicines and Healthcare products Regulatory Agency
MOPC 21	Mouse IgG1 Isotype Control
MPLA	Monophosphoryl lipid A
MRV	Mammalian Reovirus
MS	Microsphere
MVA	Modified Vaccinia Virus Ankara
MW	Molecular Weight
N	Nucleoprotein of SARS-CoV-2
ng	nanogram

NHK-α1AT	Null Hong Kong mutant of α1-antitrypsin
NK	Natural Killer
NP	Nanoparticle
NS	Nanosphere
NS1	Ig k light chain
OVA	Ovalbumin
PAGE	Polyacrylamide Gel Electrophoresis
PAMP	Pathogen Associated Molecular Patterns
PAP	Prostatic Acid Phosphatase
PBMC	Peripheral Blood Mononuclear Cells
PBS	Phosphate-buffered saline
PCR	Polymerase Chain Reaction
PdI	Polydispersity Index
PEG	Polyethylene Glycol
Pfu	Plaque-forming Unit
poly I:C	Polyinosinic-polycytidylic acid
PRR	Pattern Recognition Receptor
RBD	Receptor binding domain
RCC	Renal Cell Carcinoma
RNA	Ribonucleic Acid
rpm	Revolutions per minute
ROS	Reactive Oxygen Species
RT	Room Temperature
RV	Reverse
RVFV	Rift Valley fever virus
S	Spike protein of the SARS-CoV-2
SARS-CoV-2	Severe Acute Respiratory Syndrome Coronavirus 2
SDS	Sodium Dodecyl Sulfate
SEAP	Soluble Embryonic Alkaline Phosphatase
Sf9	Clonal isolate of Spodoptera frugiperda
SN	Supernatant
SRP	Signal Recognition Particle
SS	Signal Sequence
ssRNA	single-stranded RNA
SV5	Small epitope found in the paramyxovirus simian virus 5
TAA	Tumor-associated Antigen
TAE	Tris-Acetate-EDTA

TEM	Transmission Electron Microscopy
TGF	Transforming growth factor
TIR	Toll/Interleukin Receptor
TLR	Toll-like Receptor
TME	Tumor Microenvironment
TNF	Tumor Necrosis Factor
TSA	Tumor Specific Antigen
TSS	Transformation and Storage Solution
V	Volts
VERO	Kidney epithelial cells from African green monkey
VLP	Virus-like Particle
WB	Whole Blood
WT	Wild Type

SUMMARY

ENGLISH VERSION

INTRODUCTION

The IC-Tagging system is a technology developed in our laboratory, based on the properties of muNS, a non-structural protein of the avian reovirus. These viruses are double-stranded RNA viruses that infect a wide range of hosts and are characterized by their segmented genome. The virus replicates inside protein inclusions or viroplasms and the protein muNS has been demonstrated to form the scaffold of these inclusion-like structures. The C-Terminal- third portion of this protein (muNS- minimal or muNS-Mi) is still able to form spherical intracellular inclusions by its own when expressed in eukaryotic cells (microspheres or MS) and bacteria (nanospheres or NS). Previous studies revealed that one of the four domains of muNS-Mi, termed IC domain, presents high affinity for the inclusions. This finding motivated the creation of the IC-Tagging methodology, in which proteins tagged with the IC domain are relocated to muNS inclusions when coexisting in the same cell. Studies conducted in our laboratory endorsed that the relocated proteins maintain their proper folding inside the micro or nanospheres. Besides that, they keep functionally active, allowing them to stablish complex interactions, undergo post-translational modifications and execute intricate biochemical reactions while integrated in the inclusions. Thanks to these features, the system has been credited with several applications, among which we can highlight the validation of protein-protein interactions, the production of large amounts of particulate material and the stabilization of enzymes.

As mentioned, with this strategy we can create both MS and NS loaded with proteins of interest enabling us to use it for several biotechnological applications. In this thesis, we will mainly focus on the NS, because of the advantages that their size confers them. Nanosystems are gaining increasing attention in the field of medicine for the treatment of a wide variety of diseases, from cancer to other infections. Their nanometric size is great benefit for improving the delivery of hydrophobic drugs and delivering therapeutics to a specific target. Moreover, they are key players in intracellular delivery, stability against degrading agents, tolerability, making a significant increase in the therapeutic index of certain drugs.

This doctoral thesis aims to leverage the properties of the IC-Tagging system to develop novel biotechnological applications. We focus our attention in three different applications: designing an autofluorescent biosensor to detect protein retro-translocation in vitro, developing a VLP-based vaccine model against enveloped viruses, with SARS-CoV-2 as an example, and creating a cancer vaccine candidate using protein-based nanoparticles and microparticles.

CHAPTER I. DESIGN OF AN AUTOFLUORESCENT BIOSENSOR TO DETECT PROTEIN RETRO-TRANSLOCATION

In this first chapter, we focused on the development of an autofluorescent biosensor to monitor protein retrotranslocation. Retrotranslocation is known as the movement of proteins from the endoplasmic reticulum (ER) to the cytosol. The vast majority of substrates that perform retrotranslocation are proteins that have been unable to reach a proper folding state. Hence, a quality control mechanism comes into play and forces their move to the cytosol, to be degraded there via the ubiquitin-proteasome system. This complex process that ends with the degradation of the target molecule is known as endoplasmic-reticulum-associated degradation, ERAD. However, degradation is not the only end for retrotranslocated substrates. This process plays a crucial role in cellular homeostasis and disease mechanisms, making it a valuable target for study.

The proposed biosensor was designed combining the IC-Tagging system with bimolecular fluorescence complementation assay. BiFC consists of the splitting a fluorescent protein into two non-fluorescent fragments that only emit fluorescence when reassemble through protein interactions. Our sensor was engineered using specifically cleaved EGFP fragments tagged with the IC domain. We introduced a linker between the fragment and the IC to enhance the flexibility of this constructs. This strategy enables us to observe the reassembly of the complementary fragments by fluorescence microscopy, concentrating the EGFP fluorescence in a small portion of space inside the cell with the particular shape of muNS-Mi spherical inclusions.

To investigate retro-translocation of substrates, two ERAD models were used: NS1 a non-secretory Ig κ light chain and NHK-α1AT a mutant form of α1-antitrypsin, both of which are known to be retro-translocated for further degradation by the proteasome. In both cases we could observe by fluorescence microscopy that the selected proteins do retro-translocate and, that once in the cytosol, IC-tagged fragments are able to relocate and co-localize in muNS-Mi inclusions, allowing the EGFP reassembly. The fluorescence derived from the EGFP reassembly was perfectly localized and easily distinguishable from the cell's autofluorescence. Thus, we confirmed that the IC-Tagging system in combination with BiFC are able to efficiently detect the retro-translocation of NS1 and NHK-alfa1 antitrypsin.

Furthermore, additional experiments were conducted to determine if our sensor was capable of detecting the effects of proteasome inhibition on the retrotranslocation process. The use of a proteasome inhibitors such as MG132 leads to the accumulation of retro-translocated substrates in the cytosol. As expected, in the presence of a proteasome inhibitor, the visualization of retrotranslocated substrates by fluorescence microscopy was perfectly endorsed. Apart from this,

we study the difference in the protein content of retrotranslocated substrates in the cells by Western-Blot. Results obtained in these studies revealed that, for both ERAD models, protein content increased considerably when the proteasome inhibitor is present. On top to that, flow cytometry analysis was performed to check if we could quantitatively study the effect of the proteasome inhibitor by means of fluorescence recovery by IC-tagging. Results obtained revealed a relevant increase of fluorescence in the presence of the proteasome inhibitor. This increase in the fluorescence is derived from an increase in the reassembly of EGFP provoked by the accumulation of the ERAD models in the cytosol. These outcomes confirm that the sensitivity of the designed fluorescent sensor is not only capable of detecting the effect provoked by the proteasome inhibitor, but also allows a reliable quantification of the retro-translocated proteins.

To summarize, our system is a simple, efficient, and reliable alternative that allows the detection of dislocated molecules either in the presence or absence of proteasome inhibitor. Furthermore, it presents great advantages in front other detection methods. Our sensor does not require the separation of the cytosolic fraction and the coupled degradation has been demonstrated no to impede the detection of dislocated substrates. Hence it can be considered an appropriate alternative to build up cell sensors.

CHAPTER II. CANCER VACCINE DEVELOPMENT USING PROTEIN-BASED PARTICLES.

In the second chapter, we investigated the use of protein-based particles for cancer immunotherapy. This project was conducted in collaboration with Dr. Sandra Diebold at the Medicines and Healthcare products Regulatory Agency (MHRA) in the UK. The research focused on leveraging the IC-Tagging system to test their efficacy in cancer immunotherapy, specifically through the design of a nano and microparticle-based vaccines for the B16-OVA pseudo-metastasis model.

Cancer immunotherapy has evolved significantly since its early conceptualization by William B. Coley, known as the father of immunotherapy. He demonstrated that the immune system could be harnessed to fight cancer through the use of bacterial toxins. Despite initial success, the risks associated with bacterial infections led to the use of alternative methods, as surgery, chemotherapy, and radiotherapy. However, immunotherapy has emerged as a promising alternative in cancer treatment. These vaccines target tumor-associated antigens or neoantigens and typically require strong adjuvants to stimulate an effective immune response.

One of the key challenges in cancer vaccine development is the identification of suitable tumor antigens. Tumor-associated antigens (TAAs) are found on both healthy and cancerous cells, while tumor-specific antigens (TSAs) or neoantigens are exclusively present in tumor cells. Although neoantigens are ideal targets for therapeutic treatments due to their specificity, most preclinical studies focus on TAAs. The main limitation of TAAs lies in their low immunogenicity and the risk of triggering autoimmunity. Additionally, the immunosuppressive tumor microenvironment further complicates effective immune activation. In an attempt to enhance immunogenicity, some therapies employ strong adjuvants. One of the main targets of adjuvants are Toll-like receptors (TLR). TLR agonists have demonstrated therapeutic potential by activating innate immune responses. Humans possess ten TLRs, each detecting specific microbial structures and their activation lead to pro-inflammatory cytokine release. This response creates a bridge between innate and adaptive immunity. However, chronic TLR activation can promote tumor progression by sustaining inflammation, highlighting the need for precise immune modulation.

In this need, protein nanoparticles have emerged as an effective delivery system in cancer immunotherapy, providing stability and controlled antigen release. The FDA's approval of Abraxane in 2005 marked a milestone for nanoparticle-based therapies. Specifically, protein-based platforms offer significant advantages in biocompatibility and functionalization in front of other type of nanoparticles. Additionally, combining antigens with adjuvants strengthens both components' biological activity, improving vaccine efficacy.

Considering the current stage landscape in this field and the need of an optimal presentation of therapeutics, the aim of the project is to develop nanoparticle and microparticle-based vaccines for the B16-OVA pseudo-metastasis model in collaboration with Dr. Sandra Diebold. To this approach, we took advantage of the IC-Tagging system properties. We used the IC-Tagging system to produce protein-based nanospheres and microspheres that are efficiently loaded with the OVA. Ovalbumin (OVA) is a harmless chicken protein that is commonly used as tumor specific antigen or neoantigen expressed in the B16 melanoma model.

Initial antigen-loaded nanospheres produced in our laboratory were found with endotoxin contamination from lipopolysaccharides (LPS), which interfered with immune response assessments. To circumvent this issue, two alternative production methods were adopted: the ClearColi bacterial expression system, which lacks endotoxin, and the baculovirus expression system, which utilizes insect cells to produce microspheres free of bacterial endotoxins.

The production and characterization of these nanospheres and microspheres required rigorous endotoxin-free conditions. Upon production, Dynamic light scattering (DLS) and optical

microscopy assessed the correct size, morphology and complexity of the different preparations. A Limulus Amebocyte Lysate (LAL) assay validated that the baculovirus-derived microspheres contained <5 IU/ml of endotoxin, allowing for immunostimulatory analysis.

To assess cytokine release, monocyte activation tests (MAT) were performed using peripheral blood mononuclear cells (PBMCs). The results demonstrated that OVA-loaded nanoparticles (OVA NS) induced significant cytokine release, particularly IL-1β, MCP-1, IL-6, IL-8, and TNF-α. Besides that, comparing the cytokine release for PBMC and whole blood we concluded similar cytokine patterns, except for IL-6, which was more abundant in the whole blood assay.

Further experiments aimed to determine which TLRs mediated the immune response to OVA NS. Using HEK-Blue reporter cell lines expressing TLR2, TLR4, TLR5, and TLR9, it was found that TLR2 played a predominant role in recognizing OVA NS. This conclusion was reinforced by the inhibition of TLR2 activity using TL2-C29, which diminished cytokine release, though residual stimulation suggested additional pattern recognition receptors might be involved.

Regarding OVA-loaded microspheres (OVA MS), IL-6 and IL-8 release was detected, but at lower levels than OVA NS. TLR activation studies showed weak stimulation of TLR2 and unclear involvement of TLR4, indicating the need for further investigation into the immune mechanisms underlying OVA MS activity. These findings suggest that nanoparticle size might influence immunogenicity, with nanospheres eliciting a stronger immune response compared to microspheres.

In conclusion, this study developed two innovative methods for endotoxin-free cancer vaccine production. The ClearColi system enabled the generation of muNS-mi-derived nanospheres loaded with the OVA neoantigen, while the baculovirus system facilitated the production of OVA-loaded microspheres. Immunostimulatory analysis confirmed that OVA NS effectively triggered TLR2-mediated cytokine release, though additional PRRs may contribute to immune activation. In contrast, OVA MS exhibited a weaker response, necessitating immunogenic analysis. Future in vivo studies will focus on assessing cytotoxic T lymphocyte responses and evaluating the anti-tumor efficacy of these vaccine candidates in mouse models expressing OVA in B16 tumor cells.

CHAPTER III. DESIGN OF A NOVEL VACCINE CANDIDATE METHOD FOR ENVELOPED VIRUSES - SARS-COV-2 AS A MODEL.

The third chapter presents the development of a VLP-like candidate vaccine construction method, applied to SARS-CoV-2. Severe acute respiratory syndrome coronavirus 2 (SARS-CoV-2) emerged in 2019, causing an outbreak in China that rapidly spread to the rest of the world, producing a world-wide pandemic without precedents, known as Covid-19 pandemic.

This virus is a single stranded RNA enveloped virus, meaning that its single-stranded RNA genome is packed in a protein core, that is surrounded by a lipidic layer containing different trans-membrane glycoproteins. Virions are spherical or ellipsoidal in shape and their size ranges between 100 nm to 116 nm. Their genome encodes for 4 structural proteins, among which we can highlight the spike protein (S) and the nucleoprotein (N). The spike protein of the SARS-Cov-2 is a type I transmembrane glycoprotein. It is characterized for forming a trimeric structure that protrudes in the outer part of the viral surface, hence its designation protein spike. This protein is presented in different conformations stochastically. The conformation of the spike protein is a key aspect for the viral entry in the host cell, thus becoming a crucial aspect for the infectivity of the virus. The success of the use of this protein in vaccines against SARS-CoV-2 is directly related with the production of neutralizing antibodies. On the other hand, the nucleocapsid protein is known to be the most abundant in the viral particle. Its main function is binding the viral RNA and packing it into the nucleocapsid structure. This protein is implicated in the host cell cycle progression and apoptosis, which is related with the virulence of the viral infection. Besides that, it is used as a highly immunogenic antigen and a diagnostic marker of infection, and it was also reported to contain sequences with T-epitope characteristics.

For these reasons, the main goal of this chapter was the development of a novel strategy for producing vaccines against enveloped virus, focusing our interest on SARS-CoV-2, taking advantage of the tunable features of the IC-Tagging system. However, details related with the design, synthesis and characterization of the particles are not shown because it is the subject of a patent application. Hence, it must remain private until intellectual property permissions are registered.

As a conclusion, we developed a novel method for producing VLPs that mimic the structure of SARS-CoV-2 applying the IC-Tagging system to different expression methods. The proper assembly of the particles was assessed using various techniques. Moreover, stability studies demonstrated that VLPs remained stable for 24 hours at room temperature and at 37°C, indicating their suitability for physiological conditions. In the next steps of the project, we will conduct

immunogenicity studies to assess their ability produce different immune responses. On top to that, the immune response induced in vivo will be characterized using different administration ways of the vaccine candidates in order to optimize its characterization for pre-clinical studies.

CONCLUSIONS

This doctoral thesis explores various biomedical applications of the IC-Tagging system, leading to three major findings. First, a fluorescent biosensor was developed by combining IC-Tagging with a bimolecular fluorescence complementation assay to efficiently detect the retrotranslocation of ERAD substrates. This biosensor demonstrated high sensitivity in detecting subtle changes in protein expression, making it a superior alternative to current detection strategies. Second, two cancer vaccine candidates were developed to overcome contamination issues caused by bacterial endotoxins. In both cases, the neoantigen OVA was encapsulated in either a protein nanoparticle or microparticle. These vaccine candidates elicited a strong cytokine response, although differences in particle size influenced their immune-stimulatory pathways. Third, a novel vaccine strategy was designed for enveloped viruses, offering advantages such as ease of production and low manufacturing costs. This approach presents a promising alternative for vaccine development, including potential applications against SARS-CoV-2. Together, these findings highlight the versatility of the IC-Tagging system in biotechnology, with significant implications for biosensing, antiviral vaccines, and cancer immunotherapy.

VERSIÓN EN GALEGO

INTRODUCIÓN

O sistema IC-Tagging é unha tecnoloxía propia desenvolvida no noso laboratorio. Esta tecnoloxía foi creada baseándose nas propiedades da muNS, unha proteína non estrutural dun reovirus aviario. Estes virus son virus de ARN de dobre cadea que infectan unha ampla gama de hóspedes e caracterízanse polo seu xenoma segmentado. O virus replícase dentro de inclusións proteicas ou viroplasmas, e demostrouse que a proteína muNS forma a estrutura base destas inclusións. o extremo C-terminal desta proteína (muNS-minima ou muNS-Mi) é capaz de formar inclusións intracelulares por si mesma cando se expresa en células eucariotas (microesferas ou MS) e en bacterias (nanoesferas ou NS). Estudos previos revelaron que un dos catro dominios de muNS-Mi, denominado dominio IC, presenta unha alta afinidade polas inclusións. Este achado motivou a creación da metodoloxía IC-Tagging, na que proteínas etiquetadas co dominio IC son relocalizadas nas inclusións de muNS. Estudos realizados no noso laboratorio confirmaron que as proteínas relocalizadas manteñen o seu correcto pregamento dentro das micro ou nanoesferas. Ademais, permanecen funcionalmente activas, o que lles permite establecer interaccións complexas, sufrir modificacións postraducionais e executar reaccións bioquímicas intrincadas cando están integradas nas inclusións. Grazas a estas características, o sistema foi acreditado con varias aplicacións, entre as que se destacan a validación de interaccións proteína-proteína, a produción de grandes cantidades de material particulado e a estabilización de encimas.

Como se mencionou, con esta estratexia podemos crear tanto MS como NS cargadas con proteínas de interese, o que nos permite empregalas para diversas aplicacións biotecnolóxicas. Nesta tese, centrarémonos principalmente nas NS, debido ás vantaxes que lles confire o seu tamaño. Os nanosistemas están a gañar unha atención crecente no campo da medicina para o tratamento dunha ampla variedade de enfermidades, desde o cancro ata outras infeccións. O seu tamaño nanométrico supón un gran beneficio para mellorar a administración de fármacos hidrofóbicos e a entrega de terapias a un obxectivo específico. Ademais, xogan un papel clave na entrega intracelular, a estabilidade fronte a axentes degradantes e a tolerabilidade, incrementando significativamente o índice terapéutico de certos fármacos.

Esta tese doutoral ten como obxectivo aproveitar as propiedades do sistema IC-Tagging para desenvolver novas aplicacións biotecnolóxicas. Centrarémonos en tres aplicacións diferentes: o deseño dun biosensor autofluorescente para detectar a retrotranslocación de proteínas in vitro, o desenvolvemento dun modelo de vacina baseado en VLPs contra virus envoltos, especificamente

o SARS-CoV-2, e a creación dunha vacina contra o cancro usando nanopartículas e micropartículas baseadas en proteínas.

CAPÍTULO I. DESEÑO DUN BIOSENSOR AUTOFUORESCENTE PARA DETECTAR A RETROTRANSLOCACIÓN DE PROTEÍNAS

No primeiro capítulo, centrarémonos no desenvolvemento dun biosensor autofluorescente para monitorizar a retrotranslocación de substratos proteicos. A retrotranslocación o dislocación é o proceso polo cal as proteínas se moven do retículo endoplasmático (RE) ao citosol. A maioría dos substratos que realizan este proceso son proteínas que non acadaron un estado de pregamento adecuado. Como resultado, entra en xogo un mecanismo de control de calidade que as forza a moverse ao citosol para seren degradadas polo sistema ubiquitina-proteasoma. Este proceso complexo, que remata coa degradación da molécula diana, é coñecido como degradación asociada ao retículo endoplasmático (ERAD). Con todo, a degradación non é o único destino dos substratos retrotranslocados. Este proceso desempeña un papel crucial na homeostase celular e nos mecanismos de enfermidades, converténdose nun obxectivo valioso para o estudo.

O biosensor proposto foi deseñado combinando o sistema IC-Tagging cun ensaio de complementación de fluorescencia bimolecular (BiFC). BiFC consiste na división dunha proteína fluorescente en dous fragmentos non fluorescentes que só emiten fluorescencia cando se ensamblan novamente a través de interaccións proteicas. O noso sensor foi deseñado usando fragmentos de EGFP especificamente cortados e etiquetados co dominio IC. Ademais, introducimos un conector entre o fragmento e o dominio IC para aumentar a flexibilidade da construción. Esta estratexia permítenos observar o reensamblaxe dos fragmentos complementarios mediante microscopia de fluorescencia, concentrando a fluorescencia de EGFP nunha pequena porción do espazo dentro da célula.

Para investigar a retrotranslocación de substratos, utilizáronse dous modelos ERAD: NS1, unha cadea lixeira de Ig κ non secretora, e NHK-α1AT, unha forma mutante da α1-antitripsina, ambos coñecidos por seren retrotranslocados para a súa posterior degradación polo proteasoma. En ambos casos, observamos mediante microscopia de fluorescencia que as proteínas seleccionadas si se retrotranslocan e, unha vez no citosol, os fragmentos etiquetados con IC poden co-localizarse, permitindo o reensamblaxe de EGFP.

Ademais, na parte final do proxcto, realizáronse experimentos adicionais para determinar se o noso sensor era capaz de detectar os efectos da inhibición do proteasoma no proceso de retrotranslocación. O uso de inhibidores do proteasoma, como MG132, leva á acumulación de

substratos retrotranslocados no citosol. Como se esperaba, en presenza dun inhibidor do proteasoma, a visualización dos substratos retrotranslocados mediante microscopia de fluorescencia foi perfectamente evidente.

En resumo, o noso sistema é unha alternativa simple, eficiente e fiable que permite a detección de moléculas dislocadas tanto na presenza como na ausencia de inhibidores do proteasoma. Ademais, presenta grandes vantaxes fronte a outros métodos de detección. O noso sensor non require a separación da fracción citosólica e demostrouse que a degradación acoplada non impide a detección de substratos dislocados. Polo tanto, pode considerarse unha alternativa adecuada para o desenvolvemento de biosensores celulares in vitro.

CAPÍTULO II. DESENVOLVEMENTO DUNHA VACINA CONTRA O CANCRO USANDO PARTÍCULAS BASEADAS EN PROTEÍNAS

No segundo capítulo, investigamos o uso de partículas baseadas en proteínas para a inmunoterapia contra o cancro. Este proxecto realizouse en colaboración coa Dra. Sandra Diebold da Axencia Reguladora de Medicamentos e Produtos Sanitarios (MHRA) do Reino Unido. A investigación céntrase en aproveitar o sistema IC-Tagging para mellorar a eficacia da inmunoterapia contra o cancro, concretamente a través do deseño de vacinas baseadas en nano e micropartículas para o modelo de pseudo-metástase B16-OVA.

A inmunoterapia contra o cancro evolucionou significativamente desde a súa conceptualización inicial por William B. Coley, coñecido como o pai da inmunoterapia. Coley demostrou que o sistema inmunitario podía ser aproveitado para combater o cancro mediante o uso de toxinas bacterianas. A pesar do éxito inicial, os riscos asociados ás infeccións bacterianas levaron ao uso de métodos alternativos como a cirurxía, a quimioterapia e a radioterapia. Porén, a inmunoterapia emerxeu como unha alternativa prometedora no tratamento do cancro. Estas vacinas diríxense a antíxenos tumorais asociados ou neoantíxenos e, xeralmente, requiren adxuvantes potentes para estimular unha resposta inmune eficaz.

Un dos principais desafíos no desenvolvemento de vacinas contra o cancro é a identificación de antíxenos tumorais axeitados. Os antíxenos tumorais asociados (TAAs) están presentes tanto en células sas como cancerosas, mentres que os antíxenos tumorais específicos (TSAs) ou neoantíxenos só se atopan en células tumorais. Aínda que os neoantíxenos son ideais para tratamentos terapéuticos debido á súa especificidade, a maioría dos estudos preclínicos céntranse nos TAAs. A principal limitación dos TAAs é a súa baixa inmunoxenicidade e o risco de desencadear autoinmunidade. Ademais, o microambiente tumoral inmunosupresor complica

aínda máis a activación inmune eficaz. Para aumentar a inmunoxenicidade, algunhas terapias empregan adxuvantes potentes, sendo un dos principais obxectivos destes os receptores Toll-like (TLR). Os agonistas dos TLR demostraron potencial terapéutico ao activar respostas inmunes innatas. Os humanos posúen dez TLRs, cada un dos cales detecta estruturas microbianas específicas, cuxa activación leva á liberación de citocinas proinflamatorias. Esta resposta crea unha ponte entre a inmunidade innata e adaptativa. Porén, a activación crónica dos TLRs pode favorecer a progresión tumoral ao manter unha inflamación sostida, o que destaca a necesidade dunha modulación inmune precisa.

Neste contexto, as nanopartículas proteicas emerxeron como un sistema de administración eficaz en inmunoterapia contra o cancro, proporcionando estabilidade e unha liberación controlada de antíxenos. A aprobación por parte da FDA de Abraxane en 2005 marcou un fito nas terapias baseadas en nanopartículas. En concreto, as plataformas baseadas en proteínas ofrecen vantaxes significativas en termos de biocompatibilidade e funcionalización en comparación con outros tipos de nanopartículas. Ademais, a combinación de antíxenos con adxuvantes fortalece a actividade biolóxica de ambos compoñentes, mellorando a eficacia da vacina.

Considerando o panorama actual neste campo e a necesidade dunha presentación óptima das terapias, o obxectivo do proxecto foi desenvolver vacinas baseadas en nanopartículas e micropartículas para o modelo de pseudo-metástase B16-OVA en colaboración coa Dra. Sandra Diebold. Para este enfoque, aproveitamos as propiedades do sistema IC-Tagging. Usamos este sistema para producir nanopartículas e micropartículas baseadas en proteínas que se cargaron eficientemente co neoantíxeno OVA. A ovoalbúmina (OVA) é un antíxeno tumoral específico ou neoantíxeno comúnmente usado no modelo de melanoma B16.

As primeiras partículas cargadas con antíxenos producidas no noso laboratorio presentaron contaminación por endotoxinas procedentes de lipopolisacáridos (LPS), o que interfería coa avaliación da resposta inmune. Para solucionar este problema, adoptáronse dous métodos alternativos de produción: o sistema de expresión bacteriano ClearColi, que elimina os sinais de endotoxinas, e o sistema de expresión baseado en baculovirus, que utiliza células de insecto para producir microsferas libres de endotoxinas bacterianas.

A produción e caracterización destas nanopartículas e micropartículas requiriu condicións estritas libres de endotoxinas. Tras a produción, a Dispersión Dinámica da Luz (DLS) e a microscopía óptica avaliaron o tamaño, morfoloxía e complexidade das diferentes preparacións. Un ensaio de Limulus Amebocyte Lysate (LAL) confirmou que as microesferas derivadas de baculovirus contiñan menos de 5 IU/ml de endotoxina, permitindo a súa análise inmunoestimuladora.

Para avaliar a liberación de citocinas, realizáronse probas de activación de monocitos (MAT) usando células mononucleares do sangue periférico (PBMCs). Os resultados demostraron que as nanopartículas cargadas con OVA (OVA NS) induciron unha liberación significativa de citocinas, especialmente IL-1β, MCP-1, IL-6, IL-8 e TNF-α. Ademais, ao comparar a liberación de citocinas en PBMCs e en sangue total, observouse un patrón similar, excepto no caso da IL-6, que foi máis abundante no ensaio con sangue total.

Realizáronse experimentos adicionais para determinar que TLRs mediaban a resposta inmune ás OVA NS. Empregando liñas celulares HEK-Blue que expresaban TLR2, TLR4, TLR5 e TLR9, os investigadores descubriron que o TLR2 desempeñaba un papel predominante no recoñecemento das OVA NS. Esta conclusión reforzouse coa inhibición da actividade de TLR2 mediante TL2-C29, o que reduciu a liberación de citocinas, aínda que a estimulación residual suxire que outros receptores de recoñecemento de patróns poderían estar implicados.

En canto ás microesferas cargadas con OVA (OVA MS), detectouse a liberación de IL-6 e IL-8, pero a niveis inferiores ás OVA NS. Os estudos de activación dos TLRs mostraron unha estimulación feble do TLR2 e unha implicación pouco clara do TLR4, indicando a necesidade de máis investigacións para comprender os mecanismos inmunes subxacentes ás OVA MS. Estes achados suxiren que o tamaño das nanopartículas inflúe na inmunoxenicidade, sendo as nanoesferas máis inmunoxénicas que as microesferas.

En conclusión, este estudo desenvolveu dous métodos innovadores para a produción de vacinas contra o cancro libres de endotoxinas. O sistema ClearColi permitiu a xeración de nanoesferas muNS-mi cargadas co neoantíxeno OVA, mentres que o sistema de baculovirus facilitou a produción de microesferas con OVA. A análise inmunoestimuladora confirmou que as OVA NS activaron eficazmente a liberación de citocinas mediada polo TLR2, aínda que outros receptores de recoñecemento de patróns tamén poderían estar implicados. En contraste, as OVA MS mostraron unha resposta máis feble, requirindo unha análise inmunoxénica adicional. Os futuros estudos in vivo centraranse en avaliar as respostas dos linfocitos T citotóxicos e a eficacia antitumoral destas vacinas candidatas en modelos murinos que expresan OVA en células tumorais B16.

CAPÍTULO III. DESEÑO DUN NOVO MÉTODO de CANDIDATO VACINAL PARA VIRUS CON ENVOLTURA - SARS-COV-2 COMO MODELO.

Neste terceiro capítulo preséntase o desenvolvemento dun método de producción dun candidato vacinal baseada en partículas semellantes a virus (VLPs) contra o SARS-CoV-2 como modelo de virus con envoltura. O coronavirus da síndrome respiratoria aguda grave 2 (SARS-CoV-2) xurdiu no ano 2019, causando un brote en China. Este brote espallouse rapidamente polo resto do mundo, xerando unha pandemia sen precedentes coñecida como a pandemia da Covid-19.

Este virus é un virus ARN monocatenario con envoltura, o que significa que está composto por un núcleo proteico que contén o seu xenoma, recuberto por unha capa lipídica con diferentes glicoproteínas transmembrana. As súas virións son esféricas ou elipsoidais e teñen un tamaño que varía entre os 100 nm e os 116 nm. Ademais, o seu xenoma codifica catro proteínas estruturais, entre as que destacan a proteína spike (S) e a nucleoproteína (N).

A proteína spike do SARS-CoV-2 é unha glicoproteína transmembrana de tipo I que forma unha estrutura trimérica que sobresae da superficie externa do virus, o que lle dá o nome de "proteína spike". Esta proteína preséntase en diferentes conformacións de maneira estocástica. A súa conformación é un aspecto clave na entrada do virus na célula hóspede, polo que xoga un papel fundamental na infectividade do virus. O uso desta proteína nas vacinas virais contra o SARS-CoV-2 está directamente relacionado coa produción de anticorpos neutralizantes.

Por outra banda, a nucleocápside proteica (N) é a máis abundante na partícula viral. A súa función principal é unirse ao ARN viral e empaquetalo na estrutura da nucleocápside. Ademais, está implicada na progresión do ciclo celular do hóspede e na apoptose, o que está relacionado coa virulencia da infección. Esta proteína tamén é altamente inmunoxénica e emprégase como marcador diagnóstico da infección.

Por estes motivos, decidimos utilizar ambas proteínas, a spike (S) e a nucleoproteína (N), para deseñar un novo enfoque na obtención de partículas semellantes a virus (VLPs). As VLPs son estruturas proteicas autoensambladas que imitan ás partículas virais sen conter material xenético. Ademais, son coñecidas por estimular de maneira eficiente tanto a resposta inmune celular como a humoral e presentan características clave na indución da resposta inmune, como a captación eficiente por células dendríticas (DCs) e a produción de anticorpos neutralizantes, converténdoas en candidatas ideais para o desenvolvemento de vacinas e aplicacións terapéuticas.

Por estas razóns, o obxectivo principal deste capítulo foi o desenvolvemento dunha nova estratexia para producir vacinas contra virus envoltos, centrando o noso interese no SARS-CoV-2, aproveitando as características modulables do sistema IC-Tagging. Non obstante, os detalles relacionados co deseño, síntese e caracterización das partículas non se amosan porque son obxecto dunha solicitude de patente. Polo tanto, deben permanecer en privado ata que se rexistren os permisos de propiedade intelectual.

Como conclusión, desenvolvemos un novo método para producir VLPs que imitan a estrutura do SARS-CoV-2 aplicando o sistema IC-Tagging a diferentes métodos de expresión. A correcta ensamblaxe das partículas foi avaliada mediante varias técnicas. Ademais, os estudos de estabilidade demostraron que as VLPs permaneceron estables durante 24 horas a temperatura ambiente e a 37 °C, indicando a súa axeitada estabilidade en condicións fisiolóxicas. Nos seguintes pasos do proxecto, realizaremos estudos de inmunoxenicidade para avaliar a súa capacidade de producir diferentes respostas inmunitarias. Ademais, caracterizarase a resposta inmunitaria inducida in vivo empregando diferentes vías de administración dos candidatos a vacina co fin de optimizar a súa caracterización para estudos preclínicos.

CONCLUSIÓNS

Esta tese doutoral explora diversas aplicacións biomédicas do sistema IC-Tagging, dando lugar a tres achados principais. Primeiro, desenvolveuse un biosensor fluorescente ao combinar o IC-Tagging cun ensaio de complementación de fluorescencia bimolecular para detectar de maneira eficiente a retrotranslocación de substratos de ERAD. Este biosensor demostrou unha alta sensibilidade na detección de cambios sutís na expresión de proteínas, converténdose nunha alternativa superior ás estratexias de detección actuais. Segundo, desenvolvéronse dúas candidatas a vacina contra o cancro para superar os problemas de contaminación causados por endotoxinas bacterianas. En ambos os casos, o neoantíxeno OVA foi encapsulado nunha nanopartícula ou micropartícula proteica. Estas vacinas xeraron unha forte resposta de citocinas, aínda que as diferenzas no tamaño das partículas influíron nas súas vías inmunoestimuladoras. Terceiro, deseñouse unha nova estratexia vacinal para virus envoltos, que ofrece vantaxes como a facilidade de produción e os baixos custos de fabricación. Este enfoque preséntase como unha alternativa prometedora para o desenvolvemento de vacinas, incluíndo aplicacións potenciais contra o SARS-CoV-2. En conxunto, estes achados resaltan a versatilidade do sistema IC-Tagging en biotecnoloxía, con implicacións significativas para a biosensórica, as vacinas antivirais e a inmunoterapia contra o cancro.

INTRODUCTION

1. Reovirales.

The former Reoviridae family, now order Reovirales, was split into two different families: Sedoreoviridae and Spinareoviridae (Figure 1). These viruses infect respiratory and enteric epithelia of a very extended host range, from fish and mammals to insects and plants. Manifestations of infection are comprised in a fairly wide range, from asymptomatic to even death.[1]

Viruses of these families are characterized by their fragmented genome, constituted by 10-12 unique segments of dsRNA and by their ability to replicate in globular inclusions. These inclusions are known as viral factories or viroplasms and they are located in the cytoplasm of the infected cells. Besides that, virions lack a lipid envelope, but they may have one, two or three concentric protein coats with an external diameter between 70-80 nm.[2,3]

Based on structural differences of the virions, the number of genomic fragments and the different strategies in the replication cycle, the members of this family can be classified in different genera (Figure 1). Only *Orthoreovirus*, *Coltivirus*, *Rotavirus*, *Orbivirus* and *Seadornavirus* are capable of infecting humans and other vertebrates while the rest of them infect plants, insect or fish. [4]

Figure 1. ***The Reovirales order.***

The genus *Orthoreovirus,* belonging to the Spinareoviridae family, is composed by viruses that possess ten fragments of dsRNA inside a 70–90 nm double layered protein capsid.[5] They are widely distributed in nature, infecting mammals, birds, reptiles and insects. The two major groups in this genus are mammalian reovirus (MRV) and avian reovirus (ARV). Both groups share multiple morphological and physicochemical characteristics.[6] However, they differ in host range, pathogenicity, genome coding capacity and biological properties, particularly the fusogenic capacity of ARVs.[7]

Avian reoviruses are widespread pathogens in bird populations, frequently causing asymptomatic infections. Nonetheless, certain strains can lead to substantial mortality rates among affected bird communities. Virulent strains are accountable for diverse infectious syndromes, with viral tenosynovitis or infectious arthritis being one of the initial conditions connected to these viruses. This ailment entails joint inflammation and gastrocnemius tendon damage. Avian reoviruses have additionally been associated with various gastrointestinal and respiratory disorders, impeding bird growth and inducing skeletal changes that directly affect farm productivity. [8,9]

1.1. Structure of the avian reovirus.

1.1.1. Genome, proteins and viral capsule.

The genome of avian reovirus was studied using polyacrylamide gel electrophoresis (PAGE), concluding that it consists of 10 different segments of dsRNA. These ten segments can be classified in three different classes according to their molecular weight: L (large), M (medium), S (small). Classes M and L consist of three segments and class S consists of four segments.[10] The positive strand of every segment correspond to its encoded mRNA and possesses a type-1 cap at its 5′ end. In contrast, the negative strand contains a pyrophosphate group at this location.[11]

The first seven nucleotides at the 5'-end and the last five nucleotides of the 3'-end of all segments remain conserved in all sequenced positive strands of avian reovirus, indicating a potential role as target signals for transcription, replication, and/or encapsulation of viral transcripts.[7]

From these 10 segments of dsRNA, ARV encode 12 different primary translation products: 8 of them are structural proteins and 4 are non-structural proteins. These 4 non-structural proteins are not incorporated into the viral particle. [12] Among them, the two major non-structural proteins, that have been termed as muNS and sigmaNS, are readily detected in the cytoplasm of infected cells. Apart from them, different proteins are generated derived from the proteolytic processing of the primary translation products.[13]

ARV virions are characterized by their icosahedral shape, about 70-85 nm in diameter. The 10 genomic fragments are located inside of the viral particle, in the inner part of a double layered protein capsid. This structure is typical of the viruses in this genus.[10,14] In 1997, former members of our laboratory determined the distribution of the structural proteins of the virus. Proteins λA, λB, μA and σA are components of the internal capsid, whereas μB, μBC, μBN, σB and σC are part of the external capsid. Moreover, λC forms turrets that pass through both capsids (Figure 2).[12]

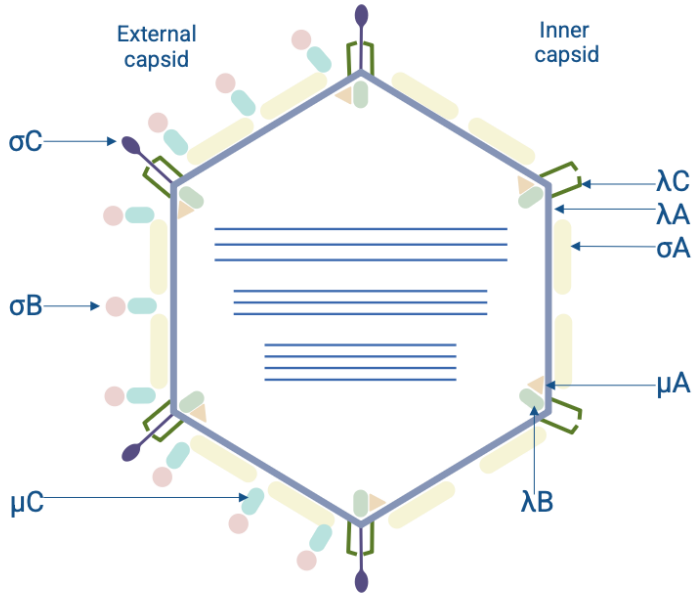

Figure 2. ***Schematic representation of the viral particle of ARV.***

1.2. Replicative cycle of avian reovirus.

1.2.1. Entry and decapsidation.

The initial binding of the virus to the host cell occurs through a receptor-mediated process involving protein sigmaC from the virus and a still unknown cell surface receptor in a specific way.[15] The receptor mediating this reaction appears to be a ubiquitous protein, because ARV are not only capable of replicating in avian cells, they are also able to enter mammalian cell lines.[16]

Chicken embryonic fibroblasts infected with ARV have been examined using electron microscopy (Figure 3), revealing that the virus enters the cells through receptor-mediated endocytosis.

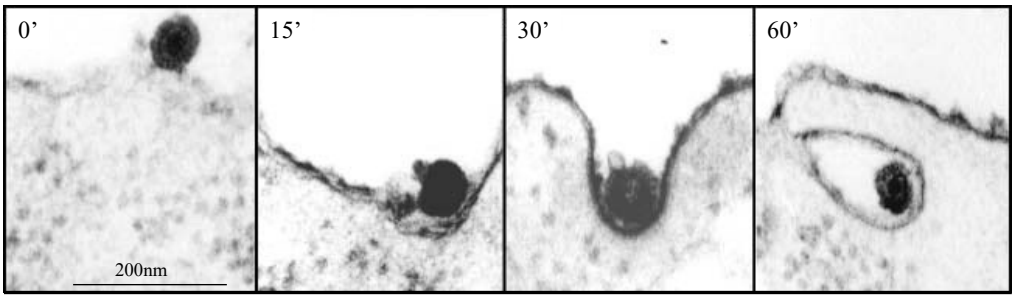

Figure 3. ***Avian reovirus entry under an electron microscope****. (Adapted with permissions from ref 17, Copyright © 2006, Springer Nature).*

After endocytosis, the decapsidation of the virus is necessary to enable the release of the transcription-competent cores. It does occur within the interior of endosomes, as depicted in Figure 4. This process requires the acidification of the environment, leading to the proteolytic processing of the muBC protein. However, the mechanism facilitating the movement of the cores across the endosomal membrane to reach the cytoplasm remains unclear.[18]

1.2.2. Genomic expression.

The genomic expression starts with the synthesis of the 10 mRNA using the negative strands of the genomic segments as templates. This process occurs thanks to the RNA polymerase activity of the λB protein. These mRNAs are responsible of the viral protein synthesis and serve also as templates for the negative strands of the viral progeny.[11]

1.2.3. Morphogenesis and exit.

Contrary to another RNA viruses, there is no nuclear contribution in the production of viral proteins and nucleic acid. Instead, the synthesis of the avian reovirus RNA takes place in dense cytoplasmic compartments (Figure 4).[19] These cytoplasmic inclusions are named as viroplasms, viral inclusions or viral factories. Viroplasms are made by structural and non-structural proteins and is there where the generation of new virions occurs, being the recruitment of viral proteins to them a controlled and selective process.[20,21] The scaffold of the viral factories is protein muNS, which plays a key role in the recruitment of proteins sigmaNS, lambdaA and lambdaC.

Finally, the mechanism of exit of the viral particles from infected cells is still unclear. However, there are two hypotheses to explain the spread of the virus: the fusogenic capacity of the p10 protein allows cell-cell fusion, [22,23] or that the apoptosis triggered by ARV enhances the viral spread.[24]

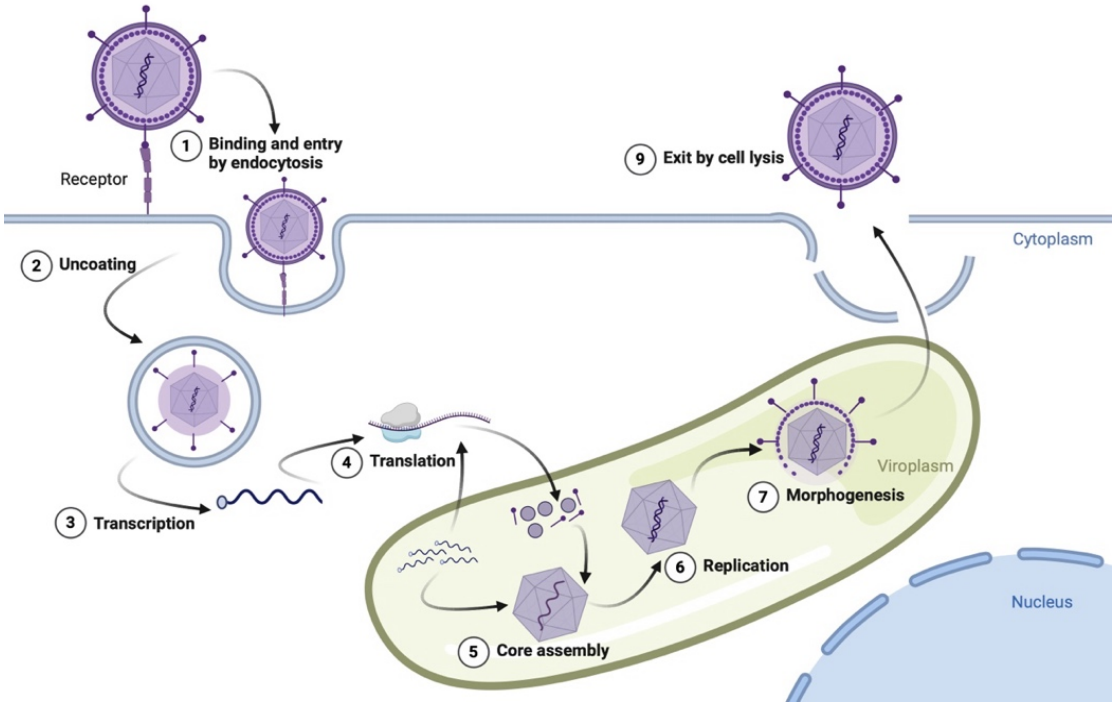

Figure 4. ***Schematic representation of the replicative cycle of avian reovirus.***

1.3. Protein muNS.

As mentioned above, protein muNS is directly involved in the formation of viral factories. It is encoded by the M3 gene and consists of 1908 nucleotides. M3 contains one single open reading frame, encoding a 635 amino acid polypeptide, whose sequence is notably different to the equivalent protein of MRV, as they differ in a 71,7%.[25]

It has been demonstrated that muNS is the only avian reovirus protein that, when expressed in the absence of other viral proteins in transfected cells, is capable of forming globular cytoplasmic inclusions and to recruit viral proteins to them. These inclusions are not microtubule-associated and their formation and are not related to aggresome or autophagosome generation. On the other hand, studies performed in our laboratory revealed that muNS monomers strongly self-associate to form homo-oligomers. These outcomes led us to the conclusion that muNS is the main driving force behind the ARV viral factories. [3]

Taking these findings into account, our laboratory conducted an extensive analysis of deletion mutants with the aim of identifying crucial regions essential for the formation of viroplasms. Results of these studies demonstrated that the C-terminal region of the protein is indispensable for the development of the factories. Conversely, deletion of the initial 140 amino acids has no impact on the protein's ability to generate inclusions. Larger deletions (from amino acid 380 to 447) resulted in the formation of smaller and spherical inclusions. On the other hand, further

removal of residues starting from position 448 impairs muNS capacity to form inclusions (Figure 5). Consequently, this minimal segment (448-635), which efficiently induces intracellular inclusions, has been designated as muNS-Mi (muNS-Minimal). The size of the spherical inclusions originated by this minimal fraction in eukaryotic cells range between 1 and 4 micrometers, so they are named microspheres (MS).[26]

On top to that, certain mutants, including muNS 84-635, muNS 112-635, muNS 208-635, and muNS 271-635, exhibited the formation of amorphous aggregates that underwent polyubiquitination and subsequent degradation by the cell. This behavior was not observed in the case of the original protein, or the spherical inclusions formed by muNS-Mi, reinforcing the notion that the latter are organized structures. [26]

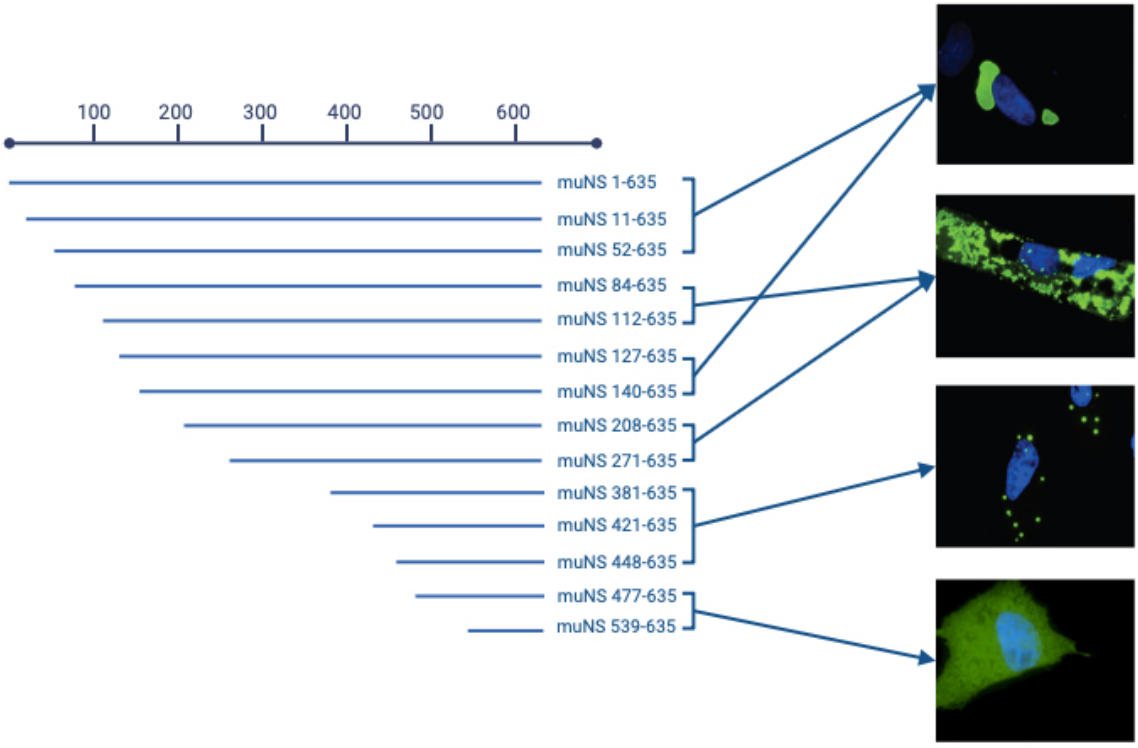

Figure 5. ***Immunofluorescence of muNS and different truncation mutants and their capability to generate inclusions.*** *Protein muNS and the different versions were observed in green by indirect immunofluorescence and nuclei were stained blue with DAPI. Amino acid composition of each protein is stated by residue numbers. (Adapted with permissions from ref 26, Copyright © 2010 American Society for Microbiology.)*

Even though it has not been possible to crystalize the protein and elucidate its quaternary structure, computational analysis revealed that muNS-Mi comprises four distinct domains (Figure 6): two predicted coiled-coil elements designated as Coil1 (C1; residues 448 to 477) and Coil2 (C2; residues 539 to 605), a segment of 62 amino acids connecting the two coiled-coils referred to as Intercoil (IC; residues 477 to 539), and a C-terminal region of the protein designated as C-Tail (CT; residues 605 to 635). [26]

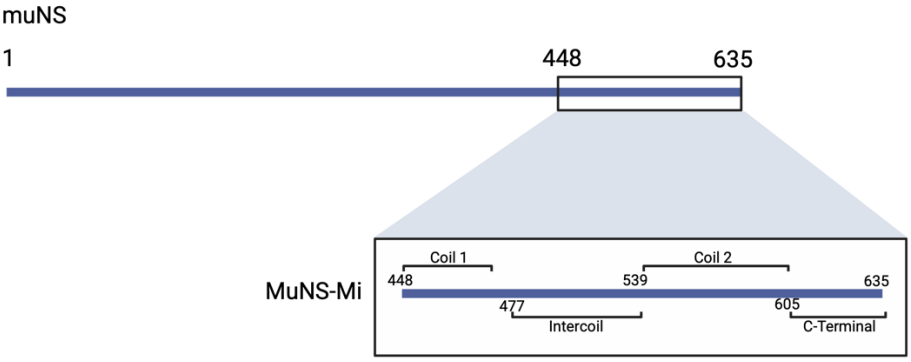

Figure 6. ***Schematic representation of the different domains of the muNS-Mi protein.***

At this stage, the laboratory set their focus on the recognition of the role of each domain in the formation of MS. The obtained results indicate that the C1 domain can be substituted with a dimerization domain, such as GFP or CA-C (C-terminal end of the dimerization domain of the HIV capsid protein). This approach indicated that the C1 domain plays a role in the generation of oligomers and, consequently the formation of MS structures through self-association. Similarly, the CT domain can be replaced by a dimerization domain. However, the phenotype of the resulting inclusions depends on the nature of the substituting domain, whether GFP (resulting in tubular inclusions) or CA-C (resulting in spherical inclusions). This observation indicated that the CT domain dictates the initial monomer-to-monomer contacts, leading to the formation of properly oriented oligomers that control inclusion shape and inclusion-forming efficiency. In contrast, point mutations at highly conserved residues, such as His487 and Cys489, within the IC domain led to a loss of the ability of both muNS and muNS-Mi to form MuNS structures or inclusions, causing the proteins to be uniformly distributed in the cytoplasm (Figure 7). Thus, all of them are essential for the inclusion formation. [26]

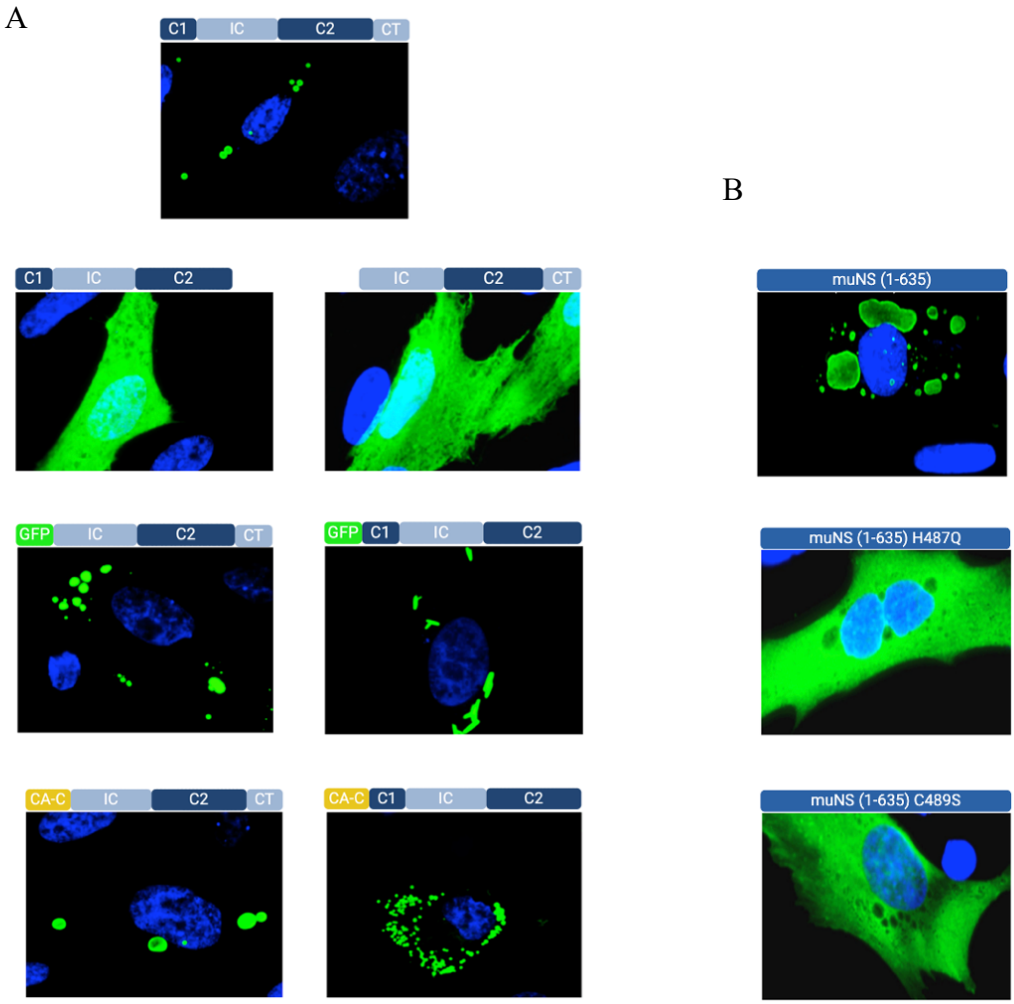

Figure 7. ***A. Immunofluorescence analysis of the roles of the different domains of muNS in the formation of viral inclusions.*** *(Adapted with permissions from ref [26], Copyright © 2010 American Society for Microbiology)* ***B. Punctual mutations of residues H487 and 489 and their effect in viral inclusion formation****. In both images protein muNS and the different versions were observed in green by indirect immunofluorescence and nuclei were stained blue with DAPI. (Adapted with permissions from ref 26, Copyright © 2010 American Society for Microbiology).*

2. IC-Tagging: basis and applications.

In the course of the investigation focused on understanding the interactions established between monomers of muNS, it was found out that the 62 residue-long Intercoil (IC) possesses a strong affinity for the inclusions formed either by muNS and muNS-Mi. This outcome opened the way towards the development of a molecular tagging system, named IC-Tagging. [26]

This system consists of two components: firstly, the muNS-Mi protein with its capability of forming spherical inclusions upon expression in both prokaryotic and eukaryotic cells. Secondly, the IC domain, which can be fused to any protein of interest at either the amino or carboxyl terminus without modifying the characteristics or cellular localization of the subject protein. Thus, when both components are co-expressed concurrently, the IC promotes the relocation of

the tagged protein to the generated inclusions taking advantage of the high affinity of the IC domain for them. Furthermore, it has been demonstrated that the inclusion-targeted proteins are properly folded and active when integrated in these structures (Figure 8).

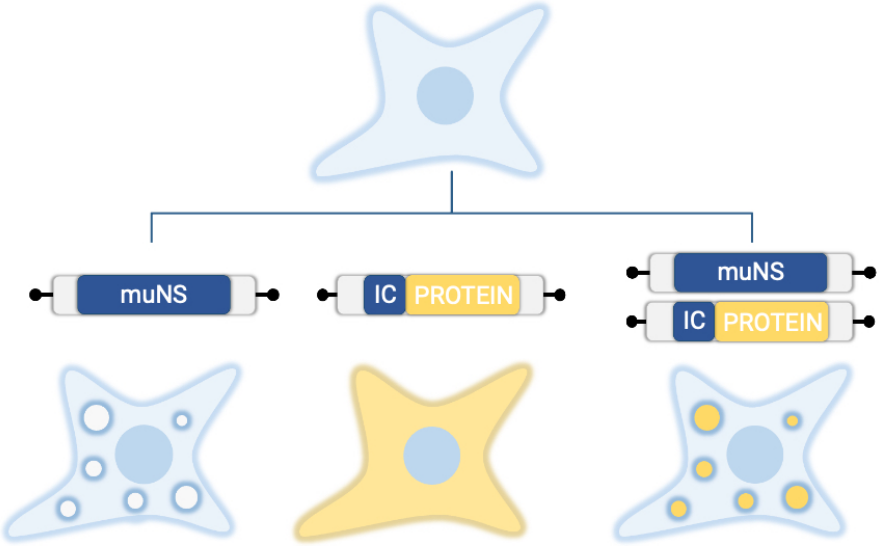

Figure 8. ***IC-tagging system basis.***

This phenomenon is perfectly exemplified in Figure 9, where GFP-IC and p53-IC are expressed in DF-1 cells either in the presence or the absence of muNS-Mi. GFP is observed in green thanks to its autofluorescence, whereas p53 is detected by indirect immunofluorescence (red). In the first column we can observe both proteins conserving their cellular location, cytosolic and nuclear respectively, while the co-expression with muNS-Mi (right panels) clearly causes the relocation of both of them to the muNS-Mi derived microspheres

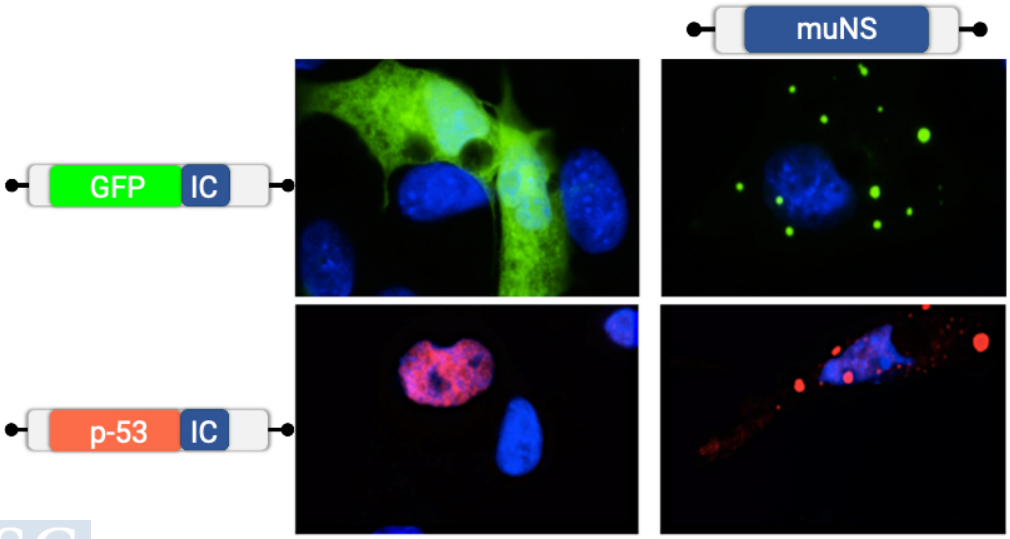

Figure 9. ***Immunofluorescence analysis of the IC-Tagging basis****. Protein GFP and the is observed in green, p-53 is labelled in red, and nuclei were stained blue with DAPI. In the left column, both IC-tagged proteins were expressed individually, while in the right column, co-expression with muNS-Mi was performed.*

Protein relocation to microspheres does not exclude them to undergo post-translational modifications, as it was shown to happen to protein Ds-Red. This protein depends on the interaction of four monomers to mature its fluorophore, and this interaction takes place through the C-terminus. [27] Consequently, if the protein is tagged with the IC tag at the C-terminus, it loses its ability to mature the fluorophore and remains non-fluorescent, while tagging the protein in the N-terminus there is no change on its behavior. However, when the C-terminal- tagged protein is co-expressed with muNS-Mi, the Ds-red protein relocates to the MS and regains fluorescence, showing that within the MS, proteins are able to interact, undergo post-translational modifications and execute intricate biochemical reactions (Figure 10).[28]

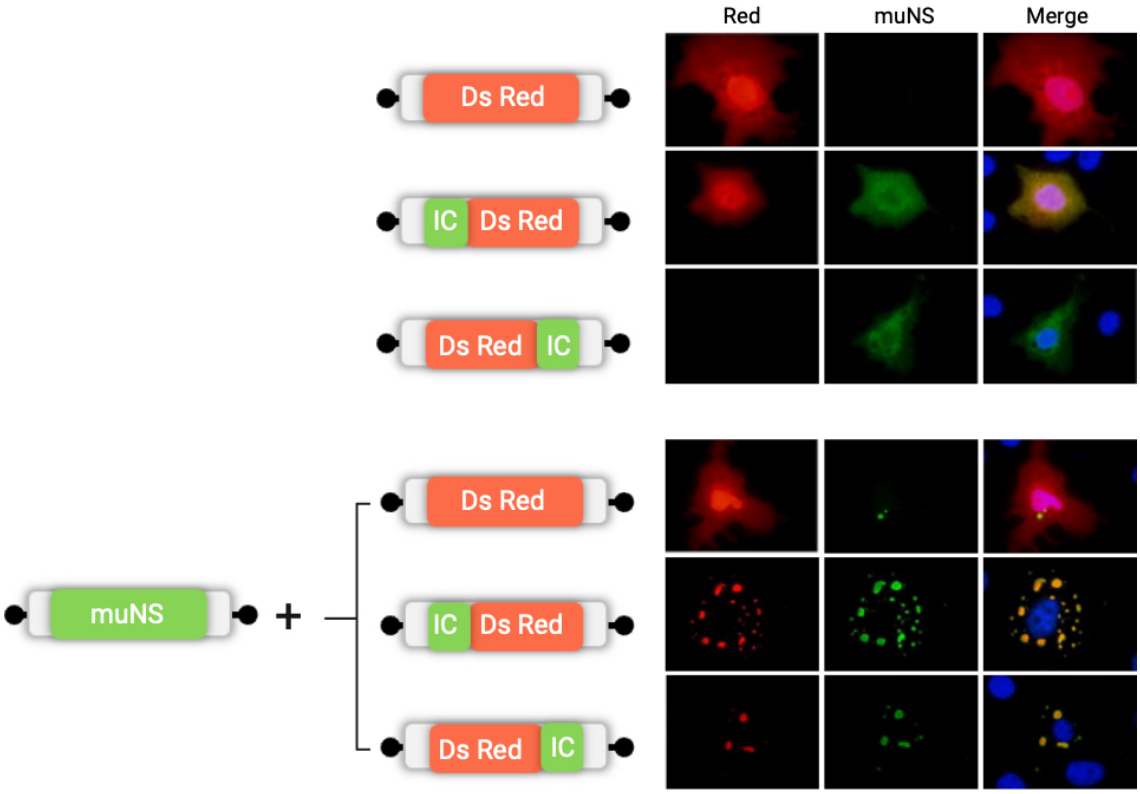

Figure 10. ***Immunofluorescence analysis showing the distribution of the dsRed protein in the cell in the absence (upper panel) or presence (lower panel) of MS****. Protein dsRed is observed in red, muNS is labelled with green antibody and nuclei were stained blue with DAPI. The presence of the IC tag at the C or N terminus of DsRED is indicated in the drawings. (Adapted with permissions from ref 28, Copyright © 2011 Elsevier B.V)*

As it has been sown above, the platform functions efficiently in eukaryotic cells. Besides that, this functionality is identically observed in prokaryotic cells. Nevertheless, in this case the size of the generated inclusion is in the nanometric scale (NS, nanospheres). The difference in size between eukaryotic cell-produced and the prokaryotic-cell produced inclusions can be observed below. (Figure 11)

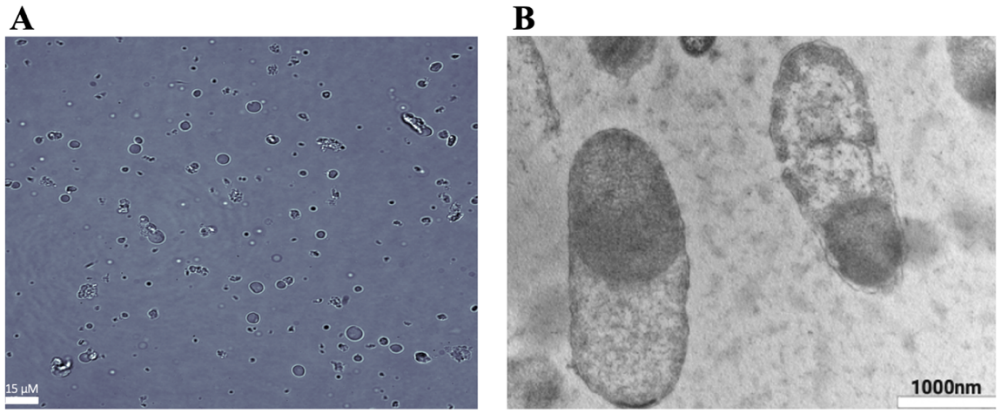

Figure 11. ***Comparison of microscopy images of eukaryotic and prokaryotic-produced viral inclusions****. **A**. Bright field imagen of MS produced in Sf9 cells via baculovirus expression system.* ***B.*** *Electron microscopy image of NS produced in BL21 bacteria, showing the production of one NS per bacteria (Adapted with permissions from 29, Copyright © 2025 by the authors).*

The IC-Tagging system is credited with different biotechnological applications. Among them we can highlight the validation of protein-protein interactions, the production of large amounts of particulate material and the stabilization of enzymes.[28,30,31] Bellow, the first two applications are going to be analyzed in depth because they are exploited during this thesis.

2.1. Validation of protein-protein interactions.

The IC-Tagging system can be used to validate protein-protein interactions within living cells by using the strategy represented in Figure 12. In brief, when an expression vector carrying the gene encoding for muNS-Mi and a plasmid expressing an IC-tagged protein B (bait) are co-transfected into cells, B should be incorporated into the inclusions. Then, performing a co-transfection with a third plasmid which expresses a protein F (fish) thought to interact with the bait, F would be also attracted to the inclusions if such interaction occurs. Otherwise, if B and F do not associate, F will maintain its normal intracellular distribution in the transfected cell.

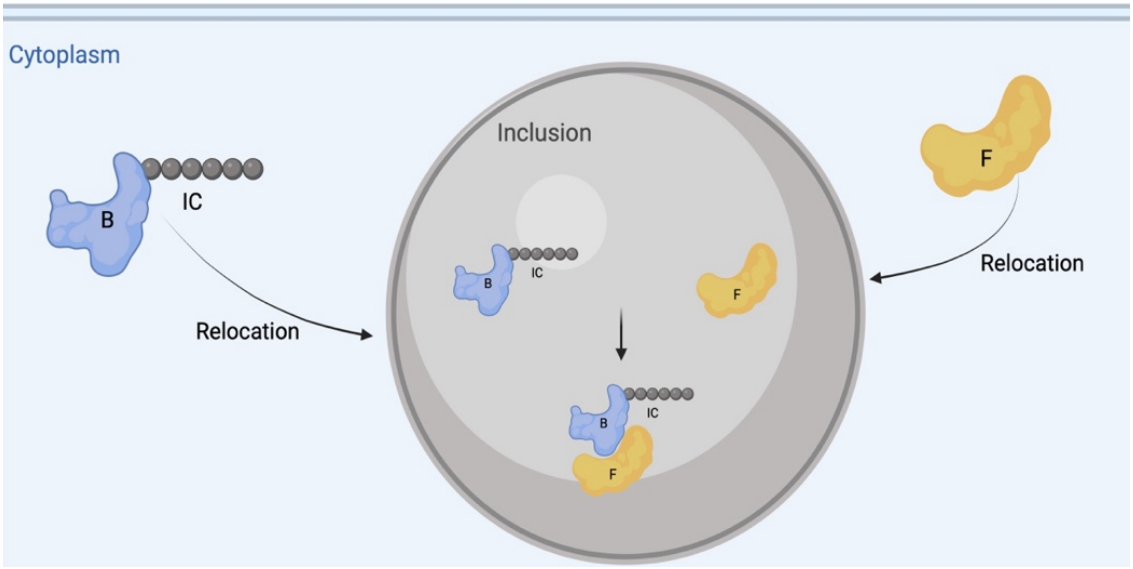

Figure 12. ***Schematic representation of the use of the IC-Tagging strategy to validate protein-protein interactions.***

Studies conducted in our laboratory have employed the p53 protein and the SV40 T antigen as examples to illustrate this concept, as their interaction have been widely described. In Figure 13 we can observe different co-expressions in eukaryotic cells. The top three panels show the recruitment of COS-7 cells endogenous T-antigen, while the bottom three panels show T-antigen expressed via plasmid. As expected, labeling p53 with IC, induced a shift in the distribution of the protein from the nucleus to the MS. However, we can observe that the T antigen, despite lacking an IC, also undergoes redistribution from the nucleus to the MS driven by its interaction with p53 in the presence of muNS/muNS-Mi. [28]

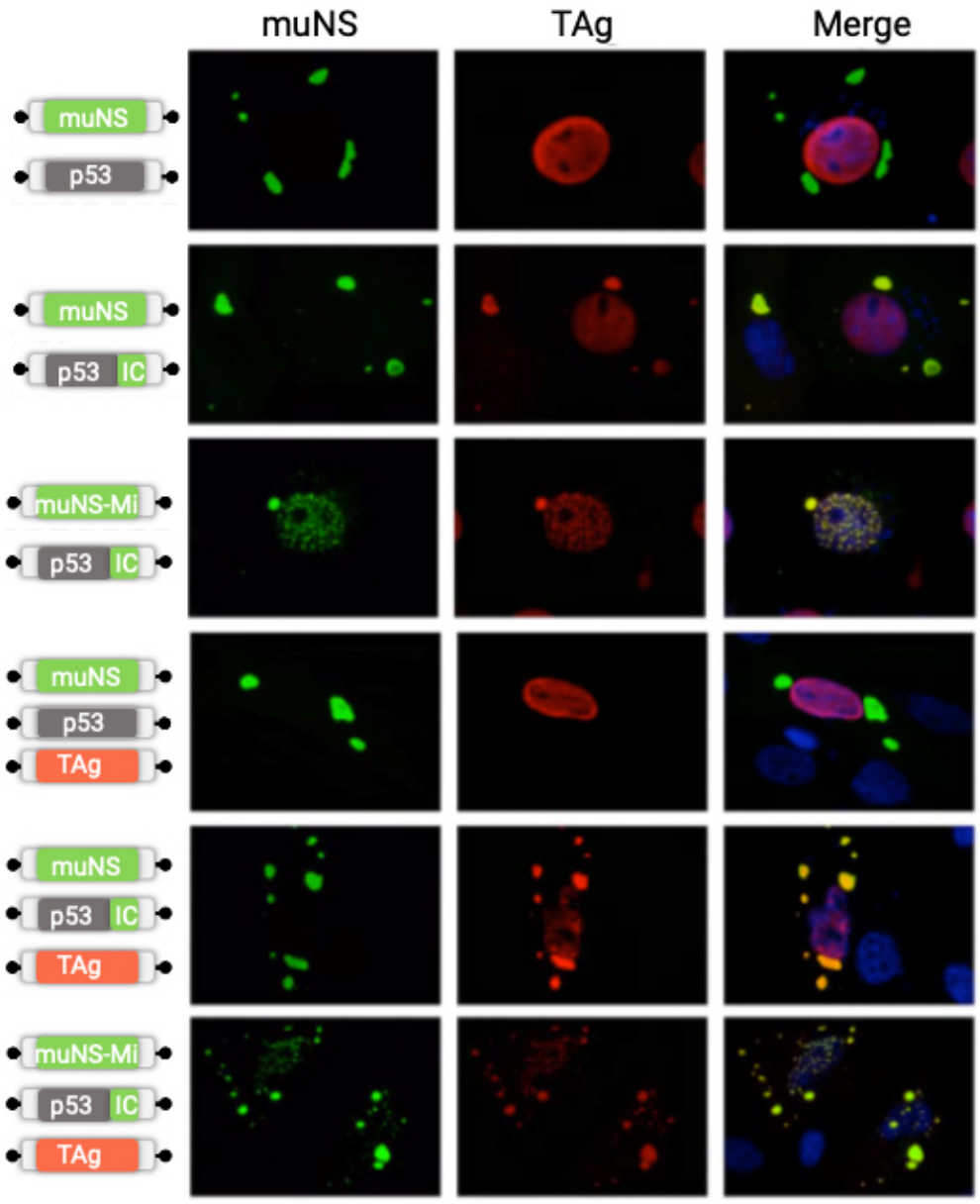

Figure 13. ***Immunofluorescence analysis of the validation of the interaction of p53 and Tag.*** *MuNS is labelled with green antibody, Tag is labelled with red antibody and nuclei were stained blue with DAPI. The expressed proteins are indicated for each panel at the left of the figure. (Adapted with permissions from ref 32 Copyright © 2010 by the authors).*

2.2. Production and purification of proteins.

IC-tagging can be also used for the production and purification of proteins, taking advantage of the baculovirus/insect cells and bacterial expression systems ability to express foreign proteins in big amounts. With both methods large amount of protein can be easily purified using simple mechanical procedures. On regard to this, the IC-Tagging platform presents several competitive advantages for immobilized protein production compared to other techniques, such as synthetic

nanoparticles. The MS/NS produced by this method are expressed, assembled, and loaded with the protein of interest simultaneously in vivo. Consequently, there is no need to generate and purify the components separately for subsequent coupling. This feature converts the IC-tagging system in an easy and time and cost-saving alternative to produce particulate material.[33]

2.3. Vaccine production system.

Directly related with the previous application, the IC-tagging system presents good advantages in the production of subunit vaccines, due to its good capability of easily purify large amount of protein and the own adjuvant activity of the muNS-Mi particles. Whereas classical vaccines require use of adjuvant in order to boost the immune response, the muNS-Mi protein has been found to possess its own adjuvant capability.[34]

As an example of this application, IC-Tagging was used to produce subunit vaccines against bluetongue virus (BTV) and African horse sickness virus (AHSV). These viruses are part of the genus *Orbivirus* and the two of them are of great relevance in the veterinary field. They infect ruminants and have high mortality rates. Thus, infection with these viruses has a high economic impact in industry.[35]

The main problem related with the vaccination against these viruses relies on the limited protection of the used vaccines (attenuated or inactivated) to the high diversity of serotypes that these viruses present. Thus, highly conserved proteins among serotypes are a common target in the production of vaccines.[35] To address this problem, our laboratory developed different vaccines against these viruses using the IC-Tagging technology in collaboration with the group of Dr. Ortego (CISA-CSIC, Valdeolmos, Madrid).

In the case of BTV, baculovirus-expressed microspheres were loaded with two structural proteins, VP2 and VP7, and a non-structural protein, NS1. These preparations were used to immunized IFNAR (-/-) mice, using soluble epitopes and empty MS as controls. A second dose of the vaccine candidate was administered 15 days after the first dose and 15 days later, a lethal dose of BTV-4 was administered to the mice. As a result, both control groups presented a 100% mortality rate only 4-5 days after infection. Whereas mice administered with the MS loaded with the viral epitopes had a 100% of survival. Furthermore, the MS loaded with the epitopes were able to confer partial (60%) cross-protection against a heterologous challenge using BTV-1.[36] Besides that, in further studies our laboratory developed a new vaccination strategy. In this case, the prime-boost was comprised of the MS in combination with the viral vaccine vector Modified Vaccinia Virus Ankara (MVA) expressing the selected epitopes, VP2, VP7, and NS1. The results

demonstrated that this new strategy provides complete protection against a homologous challenge with BTV-4 and heterologous challenge with BTV-1 in IFNAR(-/-) mice.[37]

On the other hand, for AHSV combination of the NS1-loaded MS with the recombinant MVA expressing NS1 was tested as a vaccine candidate against AHSV-4. In this case, while the MS or MVA vaccines induced 80% of protection when used individually, combined MS-MVA-NS1 immunization confers complete protection against either homologous and heterologous AHSV challenge (AHSV-9). [38]

3. The use of proteins as therapeutic agents.

Proteins are macromolecules with a wide and diversified range of functions in biological media such us the transport of molecules, the catalysis or inhibition of biochemical processes, the storage of amino acids or the maintenance of different structures. [39,40]

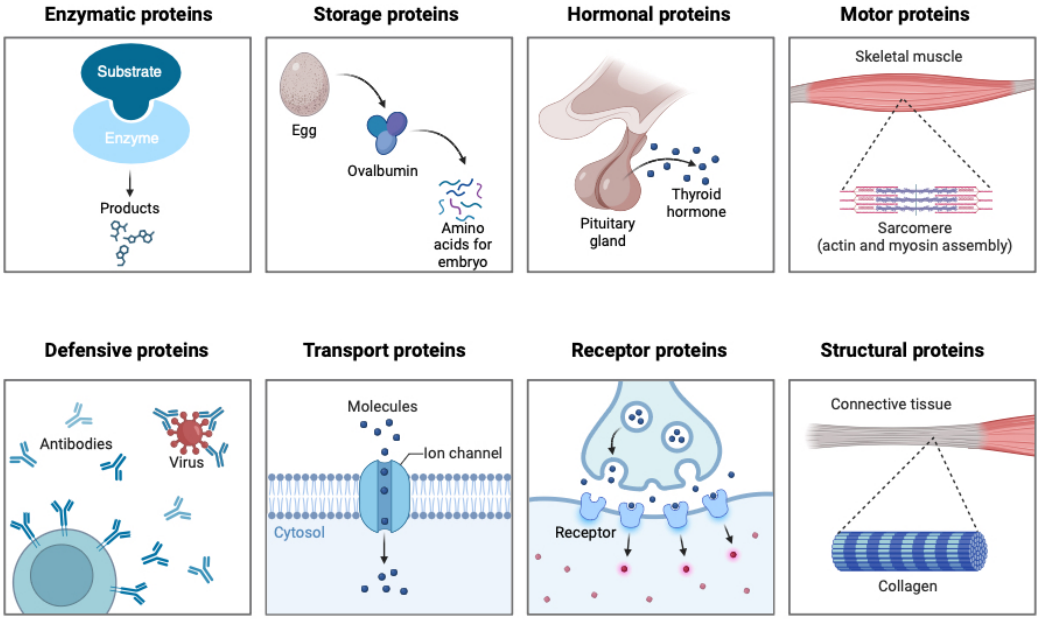

Figure 14. ***Different functions of proteins.***

Proteins have, due to their intrinsic characteristics, a great potential in the therapeutic field, presenting several advantages to small drugs. Among others, it is crucial to highlight their biocompatibility and their specific activity. Besides that, the shorter time to obtain the FDA approval compared to small drugs and the ease in the obtention of the patent protection have made them an attractive target in financial terms.[41]

To find the beginning of the use of proteins as therapeutic agents we have to look back to 1922, when Banting and Best discovered insulin. At first stage, crude extracts of different animal pancreas were used to treat diabetes.[42] However, it was not until 1978 when recombinant human insulin was expressed and produced.[43] Finally, in 1982 the FDA approved the recombinant protein human insulin for the treatment of type I and II diabetes mellitus. This was the beginning of a new era in the context of protein therapeutics.[42] Since then, the number of protein-based therapeutics approved by the FDA have grown exponentially. In 2023 the number of them was approximately 350 and their field of action is very wide, ranging from cancer therapy to immune-mediated disorders.[44]

Although there have been several advances in development of therapeutic proteins, this field is addressing several challenges. On the one hand, the fragile conformation stability limits the modification or re-formulation of the protein. [45] Additionally, the high molecular weight, short half-lives, instability against enzymatic degradation, and immunogenicity represent great disadvantages in their use. Besides that, protein therapeutics present several problems regarding membrane permeability, what limits them to extracellular targets, resulting in a limited therapeutic use.[46,47]

This problematic prompts the search of efficient protein delivery systems in order to improve the access of proteins to the required target. The focus of these system is related to enhance solubility, bioavailability, immunogenicity, safety, and protection against degrading agents such us enzymes. Besides that, they aim to decrease the secondary effects related to toxicity.[48] Different ways to improve the therapeutic properties of proteins include chemical modification, conjugation with large polymers, encapsulation or the use of stimuli-responsive nanomaterials. [49,50] In this scenario, nanotechnology has emerged as a great tool to engineer therapeutic proteins. Nanosystems are thought to act as vehicles for proteins and palliate their previously mentioned weaknesses.[51]

3.1. Nanotechnology: the key in therapeutic proteins.

Nanotechnology refers to the study and application of materials and processes at the nanoscale, originally within the range of 1 to 100 nanometers.[52] However, currently the prefix ‘nano’ is widely used to define materials from 1 to 1000 nanometers (Figure 15). [53]

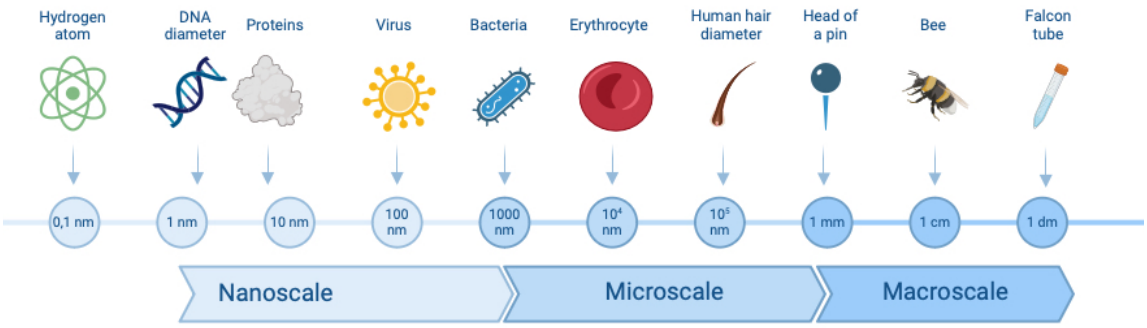

Figure 15. ***Relative size of the nanometric objects compared to other objects.***

These nanosystems, commonly known as nanoparticles (NPs), are arising in the field of medicine due to their enhanced therapeutic effects. They are posed as a solution to the main problems related to therapeutic proteins and peptides: improve the delivery of hydrophobic drugs, deliver of therapeutics to a specific target, intracellular delivery, stability against degrading agents, tolerability and therapeutic index.[54,55] Even though the treatment of cancer is the main target in the application of nanoparticle-derived therapies, the treatment of other diseases is taking advantage of their benefits, such us anemia, nervous system disease and others. Furthermore, nanoparticles are also utilized in vaccine development and diagnosis techniques.[56–58]

Since the FDA's initial approval of Diprivan® in 1989, which is a liposomal formulation of propofol, several nanomedicines have entered the market. [59,60] Figure 16 shows some of the breakthroughs in the field of nanomedicine in order of time, including Doxil®, a nanomedicine used for the treatment of ovarian cancer that is still used nowadays.[61] Additionally, it includes the recently approved mRNA vaccines developed by BioNTech/Pfizer and Moderna that play a crucial role during the COVID-19 pandemic.[62]

Currently, 100 nanomedicines are commercially available, with an additional 563 in clinical development. Considering the constant increasing number of approved nanoparticle therapies and those which are in clinical trials, it is obvious that this field rapidly expanding with the aim of improving human health. [58]

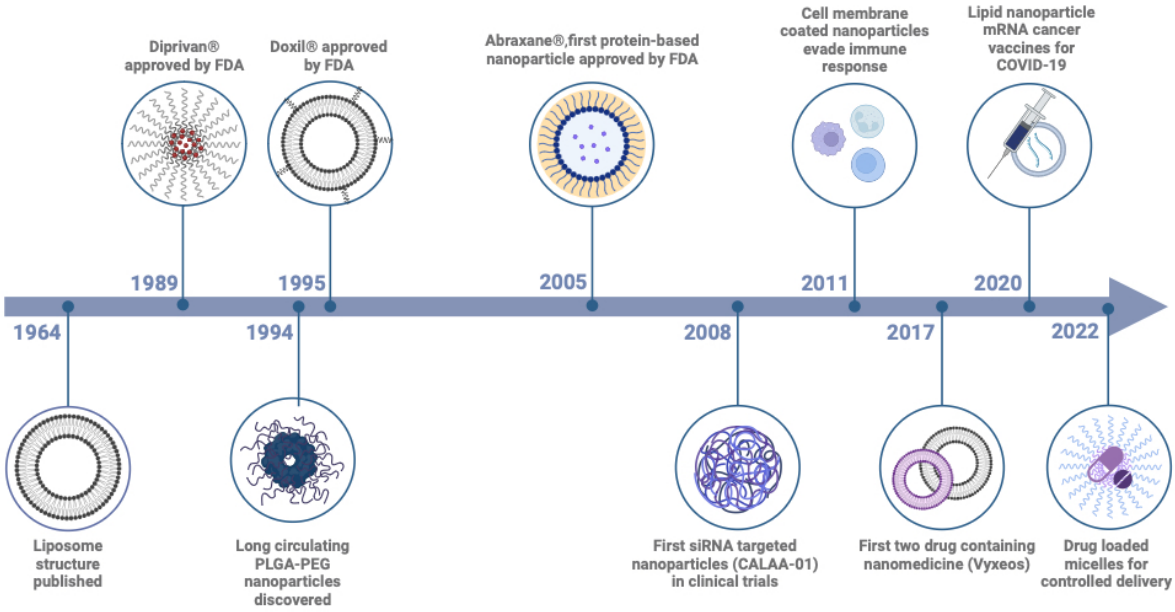

Figure 16. ***Timeline of some of the most representative events in the history of nanomedicines.***

3.1.1. Classification of nanoparticles.

The classification of nanoparticles can be performed following different criteria: dimensionality, shape, or origin. However, the most common classification is based on the composition of the nanoparticle. According to this categorization nanoparticles can be divided into three different groups: organic NPs, carbon-based NPs and inorganic NPs (Figure 17). [63]

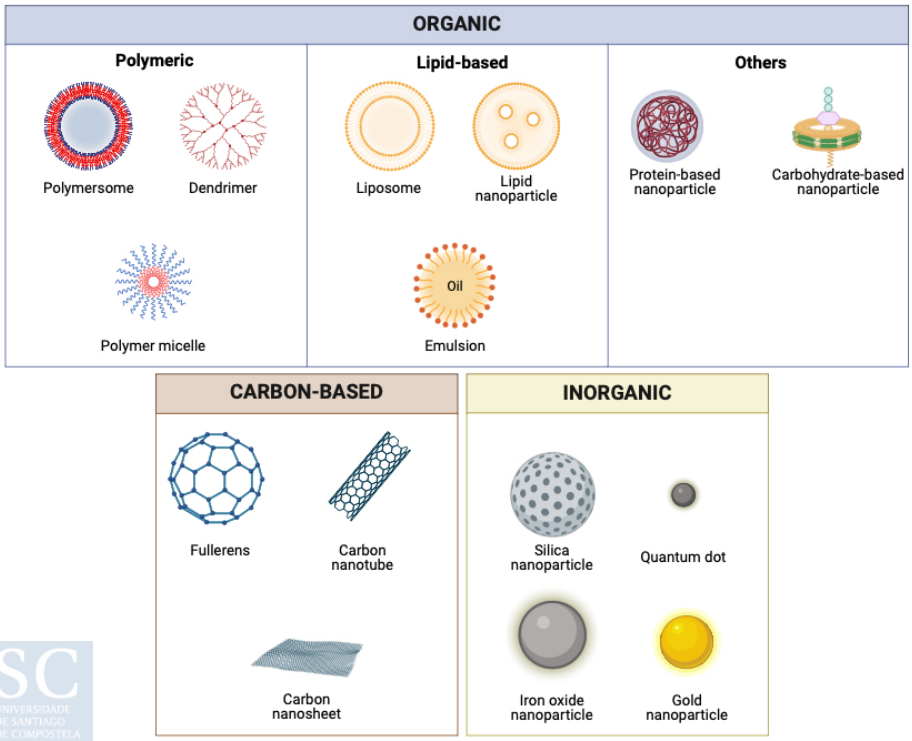

Figure 17. ***Nanoparticle classification and examples of each group.***

The group of organic nanoparticles comprise those which are composed of lipids, polymers, proteins, carbohydrates or any other organic compound.[63] Among them, lipidic and polymeric NPs are the most common ones due to therapeutic and manufacturing reasons. Polymeric NPs enables a direct control over the targeting, reducing in this way the systemic toxicity. On the other hand, lipidic nanoparticles present clear advantages regarding biocompatibility and the ease of encapsulation.[64] Due to their relevance in this thesis, protein-based nanoparticles and cell membrane-coated nanoparticles will be further analyzed in chapter II.

Carbon-based NPs are those exclusively made by carbon atoms. This feature confers carbon-based systems very particular electronical properties. For this reason, carbon-based NPs are widely used for environmental applications.[65] On top to that, they are an object of study in the biomedical field, although their proved cellular toxicity is still a great challenge.[66]

To conclude, inorganic nanoparticles are those that are not made of carbon, generally metal or metal oxide-based NPs.[63] The physicochemical properties of these particles endowed them with potential applications in magnetic recording, sensing, and biological diagnosis.[67]

3.2. Micrometric sized therapeutics.

Even though nanometric size therapeutics have attracted great attention in the last years, micrometric particles are presented as useful alternatives in certain cases. One of the differences against nanoparticles is the lowest rate of clearance by the reticuloendothelial system. Besides that, micrometric therapeutics enable possibility to design therapeutic agents that are released in the systemic circulation, mimicking a continuous intravenous administration. This feature is a cornerstone in the frequency of administration that the patient requires, which is particularly important in certain populations such us pediatric, geriatric or patients presenting psychiatric disorders. [68]

An example of micrometric therapeutic agent is TRELSTAR®, a therapeutic agent used in the treatment of advanced prostate cancer. This therapy is a peptide-based particle coated with PGLA, forming microgranules. The formulated peptide is a gonadotropin releasing hormone agonist that acts by suppressing the production of sexual hormones, particularly testosterone. Its administration is intramuscular, and it is required every 4, 12 or 24 weeks, depending on the patient needs.[69]

OBJECTIVES

This doctoral thesis aims to exploit the unique features of the IC-tagging system in order to develop different biotechnological applications. Thus, it will grow the list of applications of the system, increasing its value in the field of biotechnology. The main objectives are:

1. Create an autofluorescent biosensor to detect protein retro-translocation in-vitro.

2. Determination of the immune response elicited by IC-tagging produced nano and micro-spheres designed as cancer vaccine candidates.

3. Establish a protocol for a novel vaccine production method against enveloped viruses, using SARS-CoV-2 as a model.

MATERIALS AND METHODS

1. Biological material.

1.1. Eukaryotic cell lines.

- CHO: immortalized cell lines derived from epithelial cells of the ovary of the Chinese hamster (Cricetulus griseus).
- DF-1: cell line obtained by spontaneous transformation of chicken fibroblast embryos (Gallus gallus)
- HEK293: cell line derived from human embryonic kidney cells. (Homo Sapiens)
- Human peripheral blood mononuclear cells (PBMCs): contributed by the Joint United Kingdom Blood Transfusion and Tissue Transplantation Services Professional Advisory Committee (JPAC). (Homo Sapiens)
- Sf9: stable cell line from pupa ovarian tissue of a fall armyworm. (Spodoptera frugiperda)
- THP1-Dual™ KO-TLR4: from the human THP1-Dual™ monocyte cell line by stable knockout of the TLR4. (Invitrogen)
- TLR Transgenic Cells: HEK-Blue reporter cells. (Invitrogen)
- VERO: cell line derived from the kidney of an African green monkey. (Chlorocebus aethiops)

1.2. Prokaryotic cells.

- BL21 (DE3) Codon Plus-RP (Agilent Technologies): Escherichia coli strain used for protein expression in bacteria through T7 polymerase. Genotype: B F- ompT hsdS (r_B- m_B-) dcm^+ Tet^r gal λ (DE3) endA Hte [argU prolL Cam^r].
- ClearColi BL21 (DE3) (Clear Coli): Genotype: F- ompT hsdSB (r_B- m_B-) gal dcm lon λ(DE3 [lacI lacUV5-T7 gene 1 ind1 sam7 nin5]) msbA148 ΔgutQ ΔkdsD ΔlpxL ΔlpxM ΔpagP ΔlpxP ΔeptA.
- DH10Bac is an Escherichia coli bacterial strain used for the propagation of recombinant baculovirus genomes. Its genotype is: F^- mcrA Δ(mrr-hsdRMS-mcrBC) φ80dlacZΔM15 ΔlacX74 deoR recA1 endA1 araD139 Δ(ara-leu)7697 galU galK $λ^-$ rpsL nupG / bMON14272 / pMON7124.
- XL1-Blue (Agilent Technologies): Escherichia coli strain used for the growth and purification of plasmids. Genotype: recA1 endA1 gyrA96 thi-1 hsdR17 supE44 relA1 lac [F´ proAB laclqZΔM15 Tn10 (Tet^r)].

1.3. Baculovirus.

- Bac-WT (wild-type): a baculovirus strain that has been devoid of the polyhedrin and P10 genes and does no express foreign proteins.
- Bac-muNS-Mi: a recombinant baculovirus that express the aminoacids 448 to 635 of the muNS protein of the avian reovirus S1133
- Bac-OVA-IC: a recombinant baculovirus that express the OVA model antigen.
- Bac-SS-S-IC: recombinant baculovirus that expresses the S protein of SASR-CoV-2.

1.4. Parental plasmids.

- pcDNA 3.1 Zeo (Invitrogen): vector for transient expression in eukaryotic cells. The cloned genes are under the control of the cytomegalovirus early promoter.
- pETDuet-1: (Sigma) Bacterial vector for the co-expression of two genes.
- pFastBac1 (Invitrogen): expression vector of the Bac-to-Bac system used to generate recombinant baculoviruses.

1.5. Antibodies.

1.5.1. Primary antibodies.

- Polyclonal antibody against the muNS protein,[25] generated in our laboratory by immunizing rabbits with the denatured muNS protein extracted from an SDS-PAGE gel. It is used in Western blot at dilutions between 1:5000 and 1:10000 and immunofluorescence at dilutions between 1: 1000 and 1: 5000.
- Monoclonal antibody against SV5 epitope produced in mouse (Thermo-Fisher). It is used at 1:5000 in Western Blot and 1:1000 in immunofluorescence.
- Monoclonal antibody against GAPDH produced in rabbit (Abcam). It is used at 1:10.000 in Western Blot.
- Polyclonal antibody against Anti-SARS-CoV-2 Spike Glycoprotein produced in rabbit (Abcam). It is used at 1:10.000 in Western Blot.

1.5.2. Secondary antibodies.

- Goat antibodies against rabbit and against mouse IgG conjugated with peroxidase for detection by Western blot (Sigma). Used at a 1:10,000 dilution.

- Goat antibodies against rabbit and against mouse IgG conjugated with various fluorochromes: Alexa Fluor 488, Alexa Fluor 594 (Invitrogen) for detection by fluorescence microscopy. All of them were used at 1:1000.

1.5.3. Capture Antibodies, detection antibodies and Standards for ELISA.

- Biotinylated Human IL-8 detection antibody (Biolegend ELISA Max kit).
- Biotinylated rat anti-human IL-6 detection antibody (BD).
- Human IL-6 coating antibody (BD).
- Human IL-6 standard donated from the Pyrogen Lab (MHRA).
- Human IL-8 coating antibody (BioLegend ELISA Max kit).
- Human IL-8 standard (Biolegend ELISA Max kit).

1.6. TLR agonists and other stimuli for MATs.

- Endotoxin Standard IS 10/178 (MHRA).
- LPS, Flagellin, MPLA, LTA, Pam3CSK4, R848, CpG ODN 2006 and PolyI:C (InvivoGen).

1.7. Enzymes.

- Lysozyme, from chicken egg powder (Sigma).
- Pfu DNA polymerase (Promega).
- Restriction enzymes: BamHI, EcoRI, NotI, XhoI. (Thermo Fisher).
- T4 phage DNA ligase (Thermo Scientific)

2. Non biological material.

2.1. Culture media.

- D-MEM (Gibco) supplemented with 10% of Fetal Bovine Serum, 100 U/ml penicillin, 100µg/ml streptomycin and 292 µg/ml glutamine (Gibco) was used for the maintenance of CHO, VERO, and HEK cells. D-MEM stock, without any supplementation, was used for cell transfection.
- R10 medium containing RPMI 1640 medium (Gibco), 10mM Hepes (Sigma),10% heat-inactivated human male AB serum, 100 U/ml penicillin (Gibco), 100 µg/ml streptomycin (Gibco) was used for the experiments using PBMCs and TLR transgenic cells.

- Sf-900II (Gibco) supplemented with 5% of Fetal Bovine Serum, 100 U/ml penicillin (Gibco), 100µg/ml streptomycin (Gibco) and 920 µg/ml of glutamine (Gibco)was used for the maintenance of Sf9 cells.
- Luria-Bertani (LB) medium was utilized for bacterial suspension culture. For the selection of transformed bacteria, the medium was amended with 100 µg/ml ampicillin, 7 µg/ml gentamicin (Sigma), 10 µg/ml tetracycline (Sigma), or 50 µg/ml kanamycin (Sigma), according to the plasmid-specific selection requirements. For solid medium culture, the same LB medium with identical antibiotic concentrations was used, supplemented with 1.5% bacto-agar (Sigma). The detailed composition of these media can be found in the protocol manual by Sambrook et al.[70]

2.2. Buffers and solutions.

- Acryalmide/Bisacrylamide (Serva).
- AP-Streptavidin (Dorset).
- Bacterial lysis buffer: 20mM Tris-HCl (pH 7.5); 200mM NaCl; 1mM DTT; 2mM $MgCl_2$; 0,25% Tween-20; 1mg/ml lysozyme and 10mM protease inhibitor.
- Blocking solution (ELISA buffer): PBS containing 2,5% FCS and 0,02% NaN_3.
- Chemiluminescent HRP Substrate (Millipore).
- Coating buffer: 0,1M $NaHCO_3$, pH 8.2 (except for mouse TNF ELISA: 0,1M Na_2HPO_4, pH 6.0).
- Con A (Biotium).
- DAPI: prepared at 100µg/ml in sterile water and sterilized through a 0.22µm filter.
- DNA electrophoresis buffer (TAE): 40 mM Tris; 1,1%, acetic acid and 1mM EDTA, (pH8.3).
- FACS buffer.
- Glutaraldehyde (70%), (Sigma).
- Hypotonic buffer: 10mM Hepes pH7.9; 10mM KCl 1M; 1.5 mM $MgCl_2$;0.5 mM DTT.
- Laemmli buffer (1x): 10% glycerol; 60mM Tris-HCl (pH 6.8); 5% β-mercaptoethanol; 0,05% bromophenol blue and 2% SDS.
- MG132 (Sigma).
- Mowiol Mounting medium (Calbiochem).
- PBS-T-Milk: PBS-T with 4% skimmed milk powder.
- PBS-T: PBS with 0.05% Tween-20.
- PBS: 137mM NaCl; 2,7mM KCl; 8mM Na_2HPO_4 and 1,5mM KH_2PO_4.
- Polymyxin B sulfate salt, Sigma-Aldrich (Dorset).
- Proteasome inhibition cocktail (Sigma).

- Quantitiy-Blue (Invitrogen).
- RIPA buffer: 50mM Tris-HCl (pH 8.0); 150mM NaCl; 1% Nonidet P-40; 0,5% sodium deoxycholate and 0,1% SDS.
- Sample buffer for 6x DNA: 15% Ficoll; 0,25% bromophenol blue and 0,25% xylene cyanol.
- SDS-PAGE electrophoresis buffer (Tris-Glycine-SDS): 25mM Tris-HCl (pH 8.3); 192 mM glycine and 0,1% SDS.
- TL2-C29 (InVivoGen).
- Transfer buffer: 25mM Tris-HCl (pH 8.3); 192mM glycine and 20%.
- TRB- buffer: 10mM Hepes-KOH (pH 7.9) and 10mM KCl.
- TRB-T buffer: 10mM Hepes-KOH (pH 7.9); 10mM KCl; 0,5% Triton X-100.
- TRB+ buffer: 10mM Hepes-KOH (pH 7.9); 10mM KCl and 5mM $MgCl_2$.
- TRB+ T buffer: 10mM Hepes-KOH (pH 7.9); 10mM KCl;5mM $MgCl_2$; 0,5% Triton X-100.
- Trypsin-EDTA. (Gibco).
- TSS: 10% PEG 4000; 5% DMSO; 25mM $MgCl_2$; 10% glycerol in LB.
- Washing buffer: PBS containing 0,05% Tween (0,5ml Tween-20 in 1000ml PBS).
- Washing buffer: PBS containing 0,05% Tween.

2.3. Solid Reagents and organic solvents.

All solid reagents and organic solvents were purchased in Sigma.

2.4. Antibiotics.

All the antibiotics used (ampicillin, gentamicin, tetracycline, and kanamycin) were purchased in Sigma.

3. Methods.

3.1. Handling conditions for eukaryotic cell cultures.

The manipulation of the eukaryotic cells was carried out under sterile conditions inside a vertical laminar flow cabinet (Teslar).

3.1.1.Cell thawing.

The thawing of frozen cell stocks was conducted by immersing the vials in a 37°C water bath to ensure rapid thawing. Then, the vial contents were transferred into falcon tubes containing pre-warmed supplemented D-MEM (37°C) and centrifuged at 500×g for 5 minutes to remove the cryoprotectant medium. The resulting cell pellet was resuspended in culture medium, seeded into cell culture flasks containing fresh medium, and incubated at 37°C under standard conditions.

3.1.2. Mammalian cell culture.

Cells were cultured in an incubator (Napco) at 37°C and with a relative humidity of 95% with 5% CO_2. Cells were passed twice a week, as they approached 70-80% surface coverage. Cells were harvested when approaching 70-80% confluency by executing the following protocol: D-MEM medium was collected, and cells were washed with 2 ml of PBS. Trypsinization for 2 minutes with 2 mL of 0.5% trypsin–EDTA allowed the cells to be harvested. The cells were recovered by adding 3 ml of supplemented DMEM.

3.1.3. Insect cell culture.

Insect cells were maintained either as a monolayer or in suspension (120 rpm) within Sanyo and Innova incubators, respectively, under ambient humidity, without CO_2 supplementation, and at a temperature of 28°C.

3.1.4. Mammalian Cell transfection.

PEI reagent (Polyscience) was used as a transfection agent.

Cells were plated, in a 12-well plate, 18–24 hours prior to transfection in 1 mL of complete growth medium per well, ensuring ≥80% confluency and incubated overnight in culture conditions. Immediately before transfection, PEI: DNA complexes were prepared. To this approach, 1 µg of plasmid DNA was added in 100 µl of D-MEM stock. Then, 3 µl of PEI reagent was added to the DNA mixture and gently mixed. This solution was incubated at room temperature for 30 minutes. The complexes were then added dropwise to the cells, ensuring even distribution by gently rocking the plate. The cells were incubated for 16–48 hours without replacing the medium, after that they were harvested and assayed as needed.

3.2. Handling conditions for prokaryotic cell cultures.

The handling of prokaryotic cells was performed in an ethanol-sterilized work using a Bunsen burner.

3.2.1. Growth of bacterial cell culture.

Bacteria were cultivated at 37ºC with agitation in LB medium containing the appropriate antibiotic based on the plasmid selection method. Antibiotics (Sigma-Aldrich, Madrid, Spain) were used at the following concentrations: ampicillin (100 µg/ml), gentamicin (7 µg/ml), tetracycline (10 µg/ml), and kanamycin (50 µg/ml). For long-term preservation, bacterial cultures were stored at -80ºC in LB medium supplemented with 20% glycerol.

3.2.2. Preparation of competent bacteria.

The appropriate bacterial strain was grown overnight in LB medium at 37ºC. The overnight culture was then diluted 1:100 in pre-warmed LB medium. Diluted culture was incubated until the optical density at 600 nm (OD600) reaches 0.3. At this point, bacteria were harvested by centrifugation at 3200 x g for 10 minutes at 4ºC using a centrifuge (Eppendorf 5430R). The pellet was resuspended in 1/10 of the original culture volume with pre-cooled TSS transformation buffer. The competent cells were then frozen at -80ºC until use.

3.2.3. Transformation of bacteria.

The selected competent bacteria were thawed on ice. 100 µl of bacteria were added to the transformant DNA. Then, bacteria were subjected to thermal shock: 30 min in ice, heat at 42ºC for 1 min and finally, ice for 2 min. After that, bacteria were recovered in 900 µl of LB without antibiotic for 40 min at 37ºC shaking. To conclude, bacteria were collected by centrifugation at 3000 g during 5 min, supernatant was discarded, and bacteria were resuspended and spread on a prewarmed LB supplemented with the correspondent antibody. Plates were incubated overnight at 37ºC.

3.3. General techniques in manipulation of nucleic acids.

3.3.1. Polymerase Chain Reaction (PCR).

The standard reactions were performed with constant reagent concentrations and amplification cycles, except for the hybridization temperature and elongation time. Typically, the amplification

protocol consisted of an initial cycle (2 min at 94ºC), followed by 30 cycles (denaturation: 30 sec at 94ºC, hybridization:30 sec at 55–65ºC, and elongation: 30 sec to 4 min at 72ºC), and a final extension step of 10 min at 72ºC. Each amplification reaction contained 5 units of Pfu DNA polymerase, 2 mM $MgCl_2$, 0.2 mM dNTPs (Invitrogen), 0.5 µM of each primer, and 1 ng of plasmid DNA.

The hybridization temperature was settled considering the melting temperature of the primers. The elongation time depended on the size of the DNA template and the elongation rate of the polymerase enzyme.

The reaction occurred in a thermal cycler (Bio-Rad) under the conditions mentioned above. All the primers were provided by IDT (Integrated DNA Technologies)

3.3.2. DNA hybridization.

For hybridization, 10 µl of each primer were mixed and boiled at 100ºC for 3 minutes. Later the mixture cooled down slowly until reached room temperature.

The reaction occurred in a thermal block (Fisher Brand) under the conditions mentioned above. All the primers were provided by IDT (Integrated DNA Technologies)

3.3.3.Isolation and purification of DNA fragments.

DNA fragments obtained either from PCR reactions or from restriction enzyme digestions were separated by agarose electrophoresis on 0.7-2% agarose gels in 1X TAE buffer in the presence of 0.5µg/ml of ethidium bromide. The correspondent DNA band was cut from the gel with a blade and transferred to a microtube. Then, DNA was purified using the commercial NucleoSpin® Gel and PCR Clean-up kit (Macherey-Nagel) following manufacturer's instructions.

3.3.4. Plasmid DNA purification.

Plasmid DNA purification on a small scale, for the analysis of transformants, was performed using the NucleoSpin® Plasmid EasyPure system (Macherey-Nagel) from 3 ml of bacterial culture. For large-scale DNA extraction, plasmids were isolated from 50 ml of bacterial culture using the PureYield™ Plasmid Midiprep System (Promega), following the manufacturer's instructions.

3.3.5. Digestion and ligation of DNA fragments.

DNA digestions with restriction enzymes were performed following the supplier's instructions, using the provided buffers and the optimal temperature for each enzyme. The reaction occurred in a thermal block.

Ligation reactions were carried out at room temperature overnight using T4 phage DNA ligase and the provided buffer with a molar ratio of vector to insert of 2:6.

3.4. Plasmid constructs for protein expression.

3.4.1. GFP fragments constructs and muNS-Mi.

- pcDNA 3.1 IC-$(G_4S)_3$-GFP1-10.

For this construction, the sequence of GFP 1-10 was obtained by PCR amplification from the plasmid pDEST-C HA-GFP1-10. The forward primer was 5′- GCGGAATTC ATGTCGAAAGGCGAGGAGCTG -3′ (EcoRI site is single underlined, and the start codon is double underlined) and reverse primer was 5′- CGCGCGGCCGCTTATTTCTCGTTTGGGTC -3′ (NotI site is single underlined and the stop codon is double underlined). The PCR product was digested and cloned between the EcoRI and NotI targets into the plasmid pcDNA3.1 Zeo+ IC-$(G_4S)_3$ to generate the plasmid pcDNA 3.1 IC-$(G_4S)_3$-GFP1-10. This receptor plasmid was previously made in our laboratory (data not shown) in which the IC-$(G_4S)_3$ was cloned between the HindIII and EcoRI restriction targets. In this way, we obtained the plasmid that expresses IC-$(G_4S)_3$-GFP1-10, with a molecular weight of 33,9 kDa.

- pcDNA 3.1 GFP11-$(G_4S)_3$-IC.

For this construction, the sequence of GFP 11 was obtained by DNA hybridization of adaptamers. The forward primer was 5′- GCGGAATTCACCATGGCGAGAGACCACATGGTGCTG CACGAGTACGTGAACGCCGCCGGCATCACCTAAGGCGGCCGCCGC -3′ (EcoRI site is single underlined, and the start codon is double underlined) and reverse primer was 5′- GCGGCGGCCGCCTTAGGTGATGCCGGCGGCGTTCACGTACTCGTGCAGCACCATGT GGTCTCTCGCCATGGTGAATTCCGC -3′ (NotI site is single underlined and the stop codon is double underlined). The hybridization product was digested and cloned between the EcoRI and NotI targets into the plasmid pcDNA 3.1 $(G_4S)_3$-IC, generating the plasmid pcDNA 3.1 GFP11-$(G_4S)_3$-IC. This receptor plasmid was previously made in our laboratory (data not shown) in which the $(G_4S)_3$-IC was cloned between the NotI and ApaI restriction targets. In this way, we obtained the plasmid that expresses GFP11-$(G_4S)_3$-IC, with a molecular weight of 11,7 kDa.

- pcDNA 3.1 GFP1-10-$(G_4S)_3$-IC.

For this construction, the sequence of GFP 1-10 was obtained by PCR amplification from the plasmid pcDNA 3.1 Zeo IC-$(G_4S)_3$-GFP1-10. The forward primer was 5′- GGAATTCACC ATGGCGTCGAAAGGCGAGG-3′ (EcoRI site is single underlined, and the start codon is double underlined) and reverse primer was 5′- CGCGCGGCCGCCTTTCTCGTTTGGGTC -3′ (NotI site is single underlined). The PCR product was digested and cloned between the EcoRI and NotI targets into the plasmid pcDNA 3.1 GFP11-$(G_4S)_3$-IC, eliminating GFP11 and generating the plasmid pcDNA 3.1 GFP1-10-$(G_4S)_3$-IC. In this way, we obtained the plasmid that expresses GFP1-10-(G_4S)3-IC, with a molecular weight of 33,9 kDa.

- pcDNA 3.1 IC-$(G_4S)_3$-GFP11.

For this construction, the sequence of GFP 11 was obtained by DNA hybridization of adaptamers. The forward primer was 5′- GCGGAATTCACCATGGCGAGAGACCACATGGTGCTG CACGAGTACGTGAACGCCGCCGGCATCACCTAAGGCGGCCGCCGC -3′ (EcoRI site is single underlined, and the start codon is double underlined) and reverse primer was 5′- GCGGCGGCCGCCTTAGGTGATGCCGGCGGCGTTCACGTACTCGTGCAGCACCATGT GGTCTCTCGCCATGGTGAATTCCGC -3′ (NotI site is single underlined and the stop codon is double underlined). The hybridization product was digested and cloned between the EcoRI and NotI targets into the plasmid pcDNA 3.1 IC-$(G_4S)_3$-GFP1-10, eliminating GFP1-10 and generating the plasmid pcDNA 3.1 IC-$(G_4S)_3$-GFP11. In this way, we obtained the plasmid that expresses IC-$(G_4S)_3$-GFP11, with a molecular weight of 11,7 kDa.

- pcDNA GFP1-10.

For this construction, the sequence of GFP 1-10 was obtained by PCR amplification from the plasmid pcDNA 3.1 Zeo IC-$(G_4S)_3$-GFP1-10. The forward primer was 5′- GGAATTCACC ATGGCGTCGAAAGGCGAGG-3′ (EcoRI site is single underlined, and the start codon is double underlined) and reverse primer was 5′- CGCGCGGCCGCCTTTCTCGTTTGGGTC -3′ (NotI site is single underlined). The PCR product was digested and cloned between the EcoRI and NotI targets into the plasmid pcDNA 3.1, generating the plasmid pcDNA 3.1 GFP1-10. In this way, we obtained the plasmid that expresses GFP1-10, with a molecular weight of 23,8 kDa.

- pcDNA GFP 11.

For this construction, the sequence of GFP 11 was obtained by DNA hybridization of adaptamers. The forward primer was 5′- GCGGAATTCACCATGGCGAGAGACCACATGGTGCT GCACGAGTACGTGAACGCCGCCGGCATCACCTAAGGCGGCCGCCGC -3′ (EcoRI site is single underlined and the start codon is double underlined) and reverse primer was 5′- GCGGCGGCCGCCTTAGGTGATGCCGGCGGCGTTCACGTACTCGTGCAGCACCATGT

GGTCTCTCGCCATGGTGAATTCCGC -3′ (NotI site is single underlined and the stop codon is double underlined). The hybridization product was digested and cloned between the EcoRI and NotI targets into the plasmid pcDNA 3.1, generating the plasmid pcDNA 3.1 GFP11. In this way, we obtained the plasmid that expresses GFP11, with a molecular weight of 1,8 kDa.

- pcDNA 3.1 muNS-Mi.

This construction was previously generated in our laboratory following the procedure described by Brandariz-Nuñez et al.[26]

3.4.2. ERAD substrates constructions.

Plasmids encoding the two ERAD models (pcDNA 3 SS-BAP-NS1-SV5-IC-$(G_4S)_3$-GFP11 and pcDNA 3.1 SS-NHK-α1AT-SV5-IC-$(G_4S)_3$-GFP11) used in chapter 1 and the non-mutant α1AT (pcDNA 3.1 SS- α1AT-SV5-IC-$(G_4S)_3$-GFP11) were purchased to Genscript.

3.4.3. Constructs of dual plasmid for bacterial expression.

- pET Duet 1. muNS-Mi 2.N-IC.

For this construction, the sequence of N-IC was obtained by PCR amplification from the plasmid pcDNA 3.1 IC-N-IC (purchased to genscript). The forward primer was 5′-CGGGATCCTACCATGTCCGACAACGGTCC -3′ (BamHI site is single underlined) and reverse primer was 5′- CCGCTCGAGCGGTTACGCTTCCACACG -3′ (XhoI site is single underlined, and the stop codon is double underlined). The PCR product was digested and cloned between the BglII and XhoI targets into the plasmid pET Duet 1. muNS-Mi, generating the plasmid pET Duet 1. muNS-Mi 2. N-IC. This receptor plasmid was previously made in our laboratory.[33] In this way, we obtained the plasmid that expresses both muNS-Mi and IC-N.

- pET Duet 1. muNS-Mi 2. IC-N.

For this construction, the sequence of IC-N was obtained by PCR amplification from the plasmid pFastBac IC-N (previously developed in our laboratory). The forward primer was 5′-CGGGATCCCGAAGATCACTTGTTGGC -3′ (BamHI site is single underlined) and reverse primer was 5′- CGGCTCGAGTTATGCCTGGGTGCTATC -3′ (XhoI site is single underlined, and the stop codon is double underlined). The PCR product was digested and cloned between the BglII and XhoI targets into the plasmid pET Duet 1. muNS-Mi, generating the plasmid pET Duet 1. muNS-Mi 2. IC-N. This receptor plasmid was previously made in our laboratory.[33] In this way, we obtained the plasmid that expresses both muNS-Mi and IC-N.

- pET Duet 1. muNS-Mi 2. OVA.

This plasmid was previously constructed in our laboratory by Pose, T.[71]

3.4.4. Construction of plasmids for baculovirus expression system.

- pFastBac SS-SC-IC.

For this construction, the sequence of SS-SC-IC was obtained by PCR amplification from the plasmid pcDNA 3.1 Zeo SS-SC-IC (purchased in Genscript). The forward primer was 5′-CGGGATCCTGCCACCATGTTCGTTTTCCTGG -3′ (BamHI site is single underlined) and reverse primer was 5′- CCGCTCGAGCGGTTACGCTTCCACACG -3′ (XhoI site is single underlined, and the stop codon is double underlined). The PCR product was digested and cloned between the BamHI and XhoI targets into the plasmid pFastBac, generating the plasmid pFastBac SS-SC-IC. In this way, we obtained the plasmid that expresses SS-SC-IC.

- pFastBac OVA.

For this construction, the sequence of OVA was obtained by PCR amplification from the plasmid pcDNA 3.1 Zeo OVA (previously develop in our laboratory). The forward primer was 5′-GCGGAATTCACCATGGGCTCCATCGG -3′ (EcoRI site is single underlined) and reverse primer was 5′- CCGCTCGAGTTACGCTTCCACACGGGGTT -3′ (XhoI site is single underlined, and the stop codon is double underlined). The PCR product is digested and cloned between the EcoRI and XhoI targets into the plasmid pFastBac, generating the plasmid pFastBac OVA-IC. In this way, we obtained the plasmid that expresses OVA-IC.

3.5. Protein expression using bacterial expression system.

For protein expression, BL21 DE3 Codon Plus-RP cells or ClearColi BL21 (DE3) were transformed with plasmids encoding the proteins of interest. A single colony from the transformation plate was used to prepare an overnight pre-culture at 37ºC. This pre-culture was then diluted 1:25 in fresh LB medium and incubated at 37ºC until the OD 600 reached 0.4–0.6. At this point, protein expression was induced using 1 mM IPTG, and the culture was incubated at 37ºC with shaking for 3 hours. The induced bacteria were harvested by centrifugation at 3200 x g for 30 minutes at 4ºC and washed twice with 1X PBS. The resulting pellet was resuspended in lysis buffer and frozen for at least 24 hours before proceeding to protein purification.

3.6. Protein expression using baculovirus expression system.

3.6.1. Generation of the recombinant baculovirus.

Recombinant baculoviruses were produced by transfecting Sf9 cells with bacmids generated using the Bac-to-Bac system. The process involved cloning PCR-amplified cDNAs into the pFastBac1 plasmid, as detailed above. Recombinant plasmids were verified by restriction analysis and sanger sequencing. After positive verification, they are used to transfect DH10Bac competent cells to generate bacmids via transposition.

Positive colonies were replated and verified by PCR using commercial M13 primers (Invitrogen), following the manufacturer's instructions. Sf9 cells were transfected with the verified bacmids using PEI. After 72 hours, the culture medium contained approximately $1x10^7$ plaque-forming units (pfu)/ml of recombinant baculoviruses.

To increase viral titers, several virus amplification steps were performed. Expression assays were then carried out to select the optimal clone for use. Baculoviral stocks were stored at 4ºC in the absence of light to maintain stability.

3.6.2. Expression of proteins using recombinant baculovirus.

After determining the viral titer, the recombinant baculoviruses were used to infect Sf9 cells in suspension with 5 plaque-forming units (pfu) per cell. The infection was performed in a flask containing Sf9 cells at a density of $1.5x10^6$ cells/ml, with viability exceeding 99%.

The cells were cultured in an Erlenmeyer flask with shaking at 120 rpm for three to five days at 28ºC. At this point, protein expression driven by the polyhedrin promoter typically reached its peak.

3.7. Purification of nanospheres produced using bacterial expression system.

The thawed bacterial pellet was incubated for 30 minutes at 37ºC with 1 mg/ml lysozyme in the same lysis buffer used during the freezing process. Lysis was performed by passing the suspension three times through a French Press homogenizer (Avestin). The resulting homogenate was centrifuged in a swinging bucket centrifuge (Eppendorf 5804R) at 2700 x g for 5 minutes at 4ºC, followed by three washes with RB+T buffer and an additional three washes with RB+ buffer.

The final pellet was resuspended in TRB+ buffer and concentrated 10-fold relative to the original lysis buffer volume for quantification.

The sample was observed under a microscope at 1000x magnification to verify structural integrity. Incorporation of the desired epitope into the purified nanospheres was assessed by SDS-PAGE, followed by Coomassie blue staining and/or Western blot analysis. Protein quantification was conducted using standard techniques after disassembly of the nanospheres.

3.8. Purification of microspheres produced using baculovirus expression system.

To purify the baculovirus-derived microspheres, infected Sf9 cells were first centrifuged for 7 minutes at 1500×g and 4°C in a swinging bucket centrifuge. The pellet was then washed twice with 10 ml of PBS containing a protease inhibitor cocktail, centrifuging under the same conditions after each wash. The cells were resuspended in RIPA buffer supplemented with protease inhibitor cocktail. The suspension was sonicated with a sonication probe (Dr. Hielscher) using two 6-minute pulses with a 30-second rest between pulses, keeping the tube on ice. After sonication, the mixture was centrifuged at 500×g for 5 minutes at 4°C. Pellet is washed once with RIPA and four times with TRB-T buffer. Then, it was subjected to 3 additional washes with TRB+. Finally, pellet was resuspended in TRB+.

The preparation was examined under a microscope to ensure no cell debris or intact nuclei were present; if detected, the sonication and washing steps were repeated. The incorporation of the desired epitope into the purified microspheres was confirmed using SDS-PAGE, followed by Coomassie blue staining and/or Western blot analysis.

3.9. Membrane extraction from Sf9 cells

To isolate cell membranes, Sf9 cells, previously washed with 1X PBS, were resuspended in hypotonic buffer (HB) supplemented with a protease inhibitor cocktail and incubated at 4°C for 15 minutes. The suspension was sonicated on ice at maximum amplitude using two cycles of 1 minute, separated by a 30-second rest. The lysate was centrifuged at 3000×g for 10 minutes at 4°C, and the supernatant is collected. This supernatant was further centrifuged at 20000×g for 25 minutes at 4°C, resulting in the membrane fraction being pelleted. The final pellet was resuspended in HB and frozen for downstream applications.

3.10. Cell membrane coating of muNS-Mi-derived NPs.

To coat our protein NPs with the Sf9 cell membrane we used a mini extruder (Avanti Polar Lipids).

The mini extruder is placed on a heating block and temperature is settled to 37º. The temperature was monitored using a thermometer inserted into the provided hole of the extruder. The extruder was assembled following manufacturer's instructions.

The mixture of NPs and cell membranes was transferred to a glass syringe, and it is inserted in the extruder. The plunger of the filled syringe was pushed until the lipid solution is completely transferred to the alternate syringe. Then, the plunger of the alternate syringe was pushed to transfer the solution back to the original syringe. This process is repeated multiple times in order to have at least 9 passes through the membrane inside the extruder. The extruder was removed from the block, and the syringe is extracted from the extruder by pulling the syringe straight out of the extruder. The extruded solution is transferred to a clean vial and stored as required.

3.11. Gel electrophoresis analysis by SDS-PAGE.

SDS-polyacrylamide gel electrophoresis (SDS-PAGE) was performed as previously described by Laemmli in 1970.[72] The resolving gel contains 12.5% polyacrylamide, while the stacking gel contains 4%. Electrophoresis is run at 210V for 40 min.

After electrophoresis, proteins were fixed and stained with 0.25% Coomassie blue in a solution containing 33% methanol and 10% acetic acid, followed by destaining in the same solution without the dye.

3.12. Dynamic light scattering.

Particle size and polydispersity index (PdI) were determined by Dynamic Light Scattering (DLS), using a Zetasizer NanoZS (Malvern Instruments). Samples were diluted 1:20 in TRB- and measurements are performed at 25º.

3.13. Immunological techniques.

3.13.1. Monocyte activation test.

Cryo-preserved PBMCS at MHRA from selected donors were thaw and diluted in R10 medium at $1x10^6$ cells/ml. At this dilution, cells were seeded in 96-well tissue culture plates.

Different dilutions of the antigen loaded nanoparticle and control stimuli were added to the wells in quadruplicates

PBMCs were incubated with all the stimuli for 18 to 21 hours. Supernatants (SN) are transferred with a multichannel pipette to separate 96-well plates splitting up the sample over three plates to avoid repeated freezing and thawing of the SN. Plates were frozen and stored in the -80°C freezer for their individual thawing for ELISA and/or multiplexing at later time points.

3.13.2. Blood collection and PBMCs and whole blood incubation with stimuli for V-PLEX Proinflammatory Panel 1 Human Kit.

This test was performed according to the guidelines provided by the Medicine and Healthcare products Regulatory Agency of the United Kingdom.

Blood collection was performed by Dr Sandrine Vessillier. 20 ml blood was collected from 5 different donors in heparin tubes (10 IU/ml blood). From each sample, 4.5 ml of blood sample was set aside for whole blood assay.

The remaining blood was diluted 1:2 in pre-warmed serum-free RPMI and mixed well by inversion. PBMCs were isolated by centrifugation and re-suspended in 10 ml RPMI and counted with CASY counter.

40.000 cell/well for PBMCs were added to each well, whereas for whole blood plates, 190µl of blood was added. Control antibodies, stimuli and OVA NS were added to each well at the corresponding concentrations. Plates were incubated at 37º and 5% CO_2 for 48h.

3.13.3. Western Blot.

For this purpose, transfection and co-transfection of cell monolayers were performed using the corresponding expression plasmids and PEI as transfection vehicle.

At the correspondent time after transfection, cells were washed twice with PBS. Cells were lysed with 1.5X Laemmli buffer, and the extract was subjected to SDS PAGE electrophoresis. After protein separation by SDS-PAGE, proteins were transferred onto a PVDF/Immobilon-P membrane (Millipore) using transfer buffer. The transfer was performed at 100 V for 1 hour using the Mini-PROTEAN III system (Bio-Rad). Non-specific binding sites were blocked with 4% skimmed milk in PBS-T (PBS containing 0.05% Tween-20).

Immunodetection was carried out by incubating the membrane with the correspondent primary antibodies diluted in PBS-T with milk for 60–90 minutes, followed by 5 washes with PBS-T to remove non-specifically bound antibodies. Antigen-antibody complexes were detected using HRP-conjugated secondary antibodies and visualized with Chemiluminescent HRP Substrate.

3.13.4. Slot-Blot

Identical amounts of non-denatured protein samples are transferred to a nitrocellulose membrane using a Bio-Dot® and Bio-Dot SF Microfiltration Apparatus (Bio-Rad) following manufacture's instructions. Non-specific binding sites were blocked with 4% skimmed milk in TBS-T (TBS containing 0.05% Tween-20).

Immunodetection was carried out by incubating the membrane with the correspondent primary antibody diluted in TBS-T with milk for 60 minutes, followed by 5 washes with TBS-T to remove non-specifically bound antibodies. Antigen-antibody complexes were detected using HRP-conjugated secondary antibodies and visualized with Chemiluminescent HRP Substrate.

3.13.5. Indirect immunofluorescence analysis.

For this purpose, transfection and co-transfection of cell monolayers grown on glass coverslips were performed using the corresponding expression plasmids and PEI as transfection vehicle.

At the correspondent time after transfection, the monolayers were washed twice with PBS and fixed for 15 min with 4% paraformaldehyde in PBS. Paraformaldehyde-fixed cells were washed twice with PBS, incubated for 5 min in permeabilizing buffer (0.5% Triton X-100 in PBS), and then blocked in PBS containing 2% BSA for 30 min at room temperature. The permeabilization step was omitted when required. Then, the cells were incubated for 1 h at room temperature with the correspondent primary antibody at the chosen dilution in blocking buffer. After five washes with PBS, cells were incubated for 30 min with the correspondent secondary antibody (1:1000) and DAPI (1:1000) or ConA (μg/ml) depending on the experiment requirements, diluted in

blocking buffer. Finally, coverslips were washed five times with PBS and mounted on glass slides adding to each one 25 µl of Mowiol DABCO mounting medium. Images were obtained with an Olympus DP-71 digital camera mounted on an Olympus BX51 fluorescence microscope or with Fusion software (Andor) with a Dragonfly spinning disc confocal microscope mounted on a Nikon Eclipse Ti-E and equipped with an Andor Zyla 4.2 PLUS sCMOS digital camera.

3.13.6. ELISAs.

To perform ELISA analysis, immunoplates were first coated with the capture antibody, diluted to the specified concentration in the appropriate coating buffer. A volume of 50 µl of the antibody solution was added to each well of a 96-well flat-bottom ELISA plate using a multi-channel dispenser, followed by incubation for 6 hours to overnight at 4°C. The plates were washed twice with PBS-Tween using an ELISA washer, and nonspecific binding sites were blocked by adding 150 µl of blocking solution per well for 2 hours at room temperature. After blocking, the plates were washed twice with PBS-Tween, and 50 µl of the correspondent dilutions for the standards and experimental supernatants are added to their respective wells. The plates were incubated for 4 hours at RT or overnight at 4°C for higher sensitivity. Following the incubation, plates were washed four times with PBS-Tween using an ELISA washer. Detection antibody, diluted in blocking solution, was added at 100 µl per well and incubated for 1 hour at RT. After this step, the plates were washed four times with PBS-Tween. Next, 100 µl of AP-Streptavidin or Avidin-HRP (depending on the selected cytokine) was added to each well, followed by a 1-hour incubation at RT. After washing the plates four times with 300 µl PBS-Tween per well, 100 µl of substrate solution was prepared using the SIGMAFAST kit (1 buffer tablet and 1 substrate tablet dissolved in 20 ml of H_2O) and added to each well to initiate the reaction. Plates were incubated for 30 minutes to overnight at RT in a humid chamber, protected from light. If necessary, the reaction was stopped by adding 25 µl of 3M NaOH per well.

The standard curve was generated from the OD A405 values of the standards, and the linear portion of the curve was used to determine the sample concentrations accurately. Optical density (OD) was measured at 405 nm using a plate reader.

3.13.7. LEGENDPLEX™ human inflammation panel 1 (13-plex).

LEGENDPLEX™ human inflammation panel 1 (13-plex) was provided by BioLegend.

This assay was performed to measure the cytokine level in supernatants extracted from MAT analysis. The experimental procedure was performed following manufacturer's instructions and

the materials provided in the kit. Samples were acquired using BD FACSCanto™ II Clinical Flow Cytometry System and data was analyzed using LEGENDplex™ Data Analysis Software v.7.1.

3.13.8. V-PLEX Proinflammatory Panel 1 Human Kit.

This assay was performed to compare cytokine release in PBMCs and whole blood samples. The experimental procedure was performed following manufacturer's instructions and the materials provided in the kit. Samples were acquired using MESO QuickPlex SQ 120 instrument and data was analyzed in DISCOVERY WORKBENCH® Software.

3.14. Quantification of cell fluorescence through flow cytometry.

For this purpose, transfection and co-transfection of cell monolayers were performed using the corresponding expression plasmids and PEI as transfection vehicle.

At the correspondent time after transfection, cells were washed twice with PBS. After that, cells were incubated for 5 minutes with sterile 0.5% trypsin–EDTA allows for subsequent harvesting in Eppendorf tubes. Cells were then washed twice with PBS by centrifugation at 500g 5 min. Finally, cells were resuspended in 200 µl of PBS and plated in a 96-well plate for analysis. Green fluorescence was measured on a Guava easyCyte BG HT collecting the emission at 525/40 nm and using InCyte v.3.2 (GuavaSoft, Millipore). Cells with typical FSC and SSC parameters were selected, and the median fluorescence intensity calculated for each sample.

3.15. Fixation of muNS-Mi-derived NS for electron microscopy analysis.

MuNS-Mi-derived nanospheres were fixed before being deposited for TEM or SEM analysis. To this approach, samples were incubated 15 min with 2% of glutaraldehyde at RT. After incubation, fixation was stopped using 5 µM of Tris pH 7.5. After that, samples are immediately deposited as explained below.

3.16. Deposition of muNS-Mi-derived NS for transmission electron microscopy analysis (TEM).

To prepare samples for TEM analysis, a piece of Parafilm was placed on a polystyrene support and secured with pins. On the Parafilm, three drops of 20 µl each were deposited: one containing the correspondent sample, one with water, and one with uranyl acetate as a stain. A Formvar/Carbon Supported Copper Grids was carefully removed from its holder and sequentially

placed on each drop for 1 minute: first on the sample drop, then on the water drop, and finally on the uranyl acetate drop. Once stained, the grid was placed into the designated holder. After preparation, the grid and holder were dried under vacuum for at least 48 hours before analysis. observation by using a JEOL JEM-F200CF-HR microscope (JEOL®).

For energy dispersive spectroscopy (EDS), the same protocol was followed, omitting the staining step.

3.17. Deposition of muNS-Mi-derived NS and CMC-NS for scanning electron microscopy analysis (SEM).

For scanning electron microscopy (SEM) analysis samples were deposited on silicon wafer substrate and dried for 48 h at 37 ºC prior to observation in an analytical scanning electron microscope (ZEISS EVO LS 15/EDX, ZEISS®)

3.18. Image processing.

Images were processed using FIJI v. 2.14.0/1.54f or Imaris Viewer 10.1.

3.19. Limulus Amoebocyte lysate (LAL) assay.

To assess the presence of bacterial endotoxins in our preparations, the gel-clot method of the LAL assay was performed using Endosafe lysate from Charles River Laboratories in conjunction with the 3rd WHO International Standard (10/178).

This assay followed the protocol outlined as Method B in Section 2.6.14 of the European Pharmacopoeia. Thus, the baculovirus derived microspheres are diluted to 0.01 mg/ml before testing. The LAL assays were conducted by Trusha Desai at the Medicines and Healthcare products Regulatory Agency (MHRA).

3.20. Testing of NS/MS on HEK Blue TLR Transgenic Cells and THP1-Dual™ KO-TLR4.

Cells were seeded in into 96-well plates in the presence or absence of TL2-C29 (100 μM). TLR agonists, and OVA-loaded NS/MS were added at different concentrations and incubated for 18-21 h at 37º. After incubation supernatants were transferred to a separate well and frozen for subsequent analysis. To detect the TLR activation, 20μl of selected supernatants were transferred

to flat-bottom 96-well plate and 180µl of Quantity-Blue Solution was added per well. Plates were incubated at 37°C for 1h and the OD at 630nm (620-655nm) was determined in a plate reader.

3.21. Bioinformatic analysis of DNA sequences.

All constructs were verified by Sanger sequencing (Stab Vida).

Basic analysis of the obtained sequences, including restriction sites, coding sequences, theoretical molecular weights, and similar features, was performed using the software ApE - A Plasmid Editor V3.1.5 (M. Wayne Davis).

Protein sequence alignments were also conducted using ApE - A Plasmid Editor V3.1.5 (M. Wayne Davis).

RESULTS AND DISCUSSION

CHAPTER I. DESIGN OF AN AUTOFLUORESCENT BIOSENSOR TO DETECT PROTEIN RETRO-TRANSLOCATION.

CHAPTER I. DESIGN OF AN AUTOFLUORESCENT BIOSENSOR TO DETECT PROTEIN RETRO-TRANSLOCATION.

1. Introduction.

In eukaryotic cells, up to one-third of the newly synthesized proteins move from the cytosol to the endoplasmic reticulum (ER) lumen in a process known as translocation. The vast majority of them are secretory and membrane bound proteins whose translation start on free ribosomes in the cytosol. However, if the emerging nascent polypeptide contains a signal sequence (SS), it is recognized by the ER-bound signal recognition particle (SRP) attracting the signal recognition particle-ribosome complex to the SRP receptor located in the ER membrane. In this way, the nascent chain is led to the translocation channel or 'translocon', Sec61, where the elongation of the chain continues towards the ER lumen.[73–75] This channel has a narrow pore, so the nascent chain slides in the translocon, by Brownian motion, in an unfolded state (Figure 18). This translocation process involves a large number of different proteins, and the mechanism of insertion is still not fully understood. Once they are in the ER lumen, they undergo a post-translational folding process, including covalent modifications, which are assisted, among others, by a wide range of proteins of the chaperon family.[76,77]

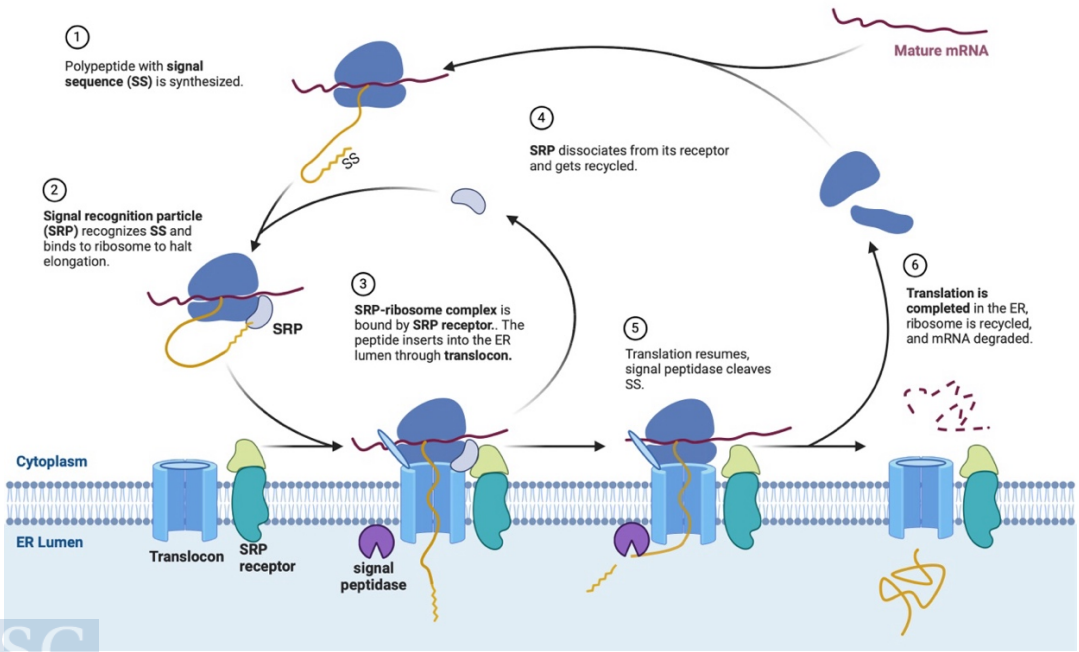

Figure 18. ***Representation of the translocation process.***

However, due to possible genetic mistakes, cellular stress or simply stochastic events, there are proteins that do not reach the proper folding state. These misfolded proteins are subjected to a quality control mechanism in order to avoid their accumulation in the ER lumen, and its possible disastrous consequences.[78] Thus, when quality control mechanisms come into play, misfolded proteins have two potential outcomes: they can be targeted for ER-associated degradation (ERAD) or ER-phagy for their annihilation either by the proteasome or lysosome, respectively.[79]

The ER-associated degradation starts with the tagging of the misfolded molecule when it is in the ER lumen. This process is mainly performed by both lectins and chaperones, that recognize and lead them to ERAD.[80] Later on, these proteins are transported back to the cytoplasm in a process known as retro-translocation or dislocation. They do it via the aforementioned conducted channel sec61, although the mechanism of the process remains unclear.[81] Once in the cytosol, they are ubiquitinated for their subsequent degradation by the proteosome S26.[82,83] However, different substrates follow different ERAD pathways depending on several factors such as the localization of the misfolded moiety or the type of substrate.[84]

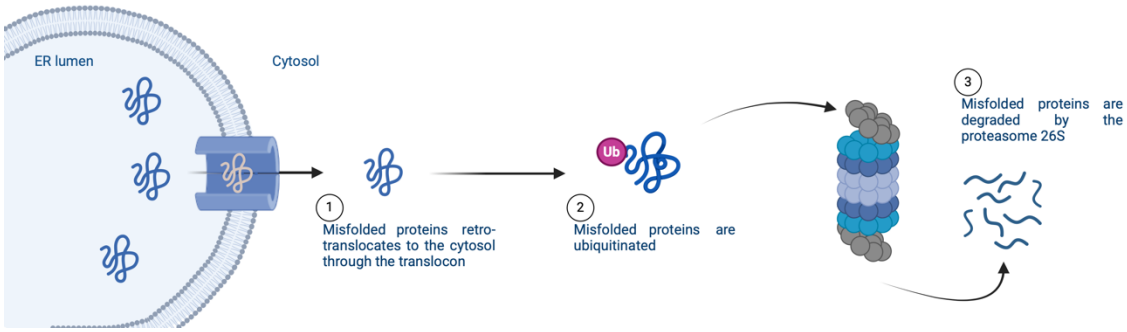

Figure 19. ***Schematic representation of the most common ERAD pathway.***

Although degradation is the main end for the retro-translocated substrates, other substrates are dislocated to entail cytoplasmic or nuclear functions. It is the case of the protein calreticulin that have been reported with different functions outside the ER, such as interact with α-integrins to maintain cell adhesion.[85]

As mentioned above, retro-translocation is a very complex process with poorly understood basis. In particular, there is conflicting data regarding the specific proteins involved in this phenomenon in mammals. The difficulty for studying this process relies in three reasons. First, the inability to distinguish between substrates that are already retro-translocated or those that are at some point prior to translocate. Second, because the kinetics of the process cannot be ascertained, as translocation and retro-translocation occur simultaneously at variable rates, and it is not possible to synchronize them. And third, determining the precise role of a specific protein in retro-translocation proved to be challenging.[86]

2. Biosensor design.

To overcome this problematic, our group, in collaboration with Prof. Oscar Burrone (Trieste, Italy), decided to adapt the IC-Tagging system to create an auto-fluorescent sensor to observe the in vitro retro-translocation of proteins from the ER to the cytosol.

To this approach, we combine our multivalent methodology with a 'bimolecular fluorescence complementation (BiFC) assay'.

2.1. ERAD models.

As a model, we studied the retro-translocation process of the non-secretory Ig k light chain NS1 (NS1), the Null Hong Kong mutant of α1-antitrypsin (NHK-α1AT). Besides that, we observed the effects caused by the inhibition of the proteasome during the retro-translocation process.

2.1.1. Non-secretory Ig k light chain NS1 (NS1).

Immunoglobulins (Ig) are essential for the humoral immune system. They play a key role in B cell activation and antigen targeting. These proteins are multimeric complexes composed by two identical heavy chains and two identical light chains.[87] In the absence of light chains, heavy chains are not secreted, but instead are retained in the ER due to their association with an ER chaperone.[88] On the contrary, light chains tend to fold easily, and they are secreted independently as monomers or dimers.[89] However, there are exceptions for this behavior as NS1, a heavy chain-lacking variant of MOPC 21 mouse myeloma cells. In this case, the absence of secretion provokes the retro-translocation of the protein for its further proteasomal degradation.[90]

2.1.2. Null Hong Kong mutant of α1-antitrypsin (NHK-α1AT).

The α1-antitrypsin belongs to the serpins, a serine protease inhibitors family. Its role is to protect the lung against the enzyme neutrophil elastase. An important lack of α1-antitrypsin can produce tissue destruction, leading to a chronic obstructive pulmonary disease. Even though there are over 70 natural mutants of the protein, we are going to focus our attention in one of them, the Null Hong Kong mutant of α1-antitrypsin.[91] This mutant was isolated from a patient with a complete absence of α1AT in serum and it has been widely used as a model of ERAD. This variant presents a frame-shift mutation provoked by a dinucleotide deletion in the codon for Leu318, which leads to a premature termination at residue 334. This results in a truncated version of the protein of 45

kDa that lacks protease inhibitory activity. Besides that, this variant is retained within the endoplasmic reticulum and degraded by ERAD.[92]

2.2. Green fluorescent protein.

In 1955, the jellyfish Aequorea aequorea, also known as Aequorea Victoria was first reported with green fluorescence when irradiated with UV light. This phenomenon is mediated by two proteins, aequorin and green fluorescent protein. Aequorin emits blue light by a chemiluminescence process, whereas GFP transduce, by energy transfer, this blue light into green fluorescent light.[93]

GFP features a unique barrel-like structure composed of 11 β-strands, with a diameter of approximately 24 Å and a height of around 42 Å. These β-strands form the walls of a so-called "β-barrel," and inside it runs a diagonal α-helix. The chromophore is located at the center of the β-barrel and is connected by the α-helical segment that runs through the barrel's center (Figure 20). This arrangement of β-sheets forming a barrel with an internal α-helix is crucial for the bioluminescence of the protein, as well as for its stability.[93]

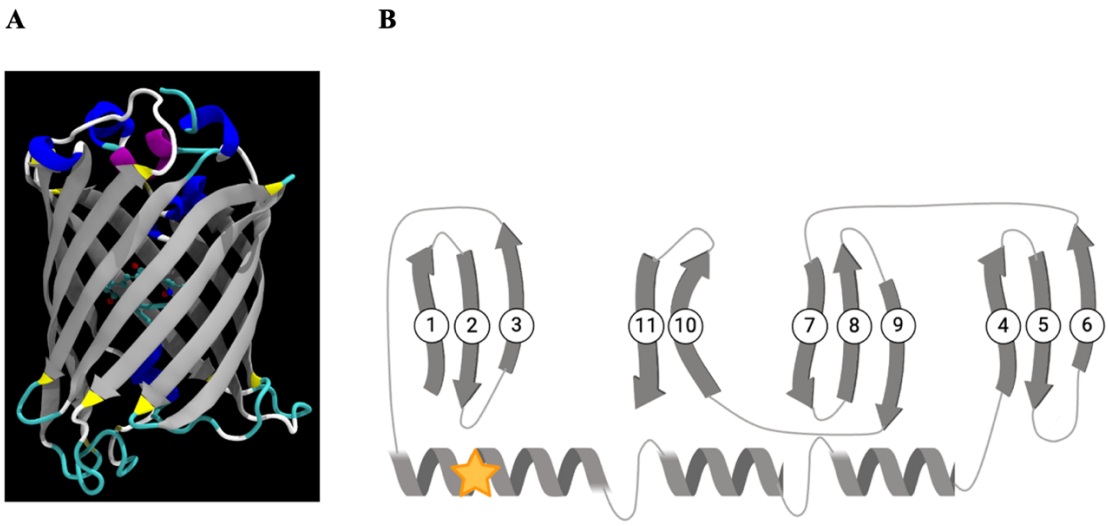

Figure 20. ***A. Three-dimensional structure of EGFP.*** *(PDB ID: 2Y0G from RCSB Protein Data Bank), with the β-strands shown in greys and α-helices visualized in blue using PyMOL software. B.* ***Folding topology of a fluorescent protein.*** *The 11 β-strands are numbered, and the yellow star indicates the position of the fluorophore.*

The cloning of GFP opened the door to a wide range of uses, since it can be expressed in numerous systems (bacteria, yeast…) and it can be fused at to a large branch of proteins, either at its N-terminal or C-terminal, without changing their original characteristics. It is interesting to remark that, when expressed in mammalian cells, GFP is located in the cytoplasm and nucleus.[94]

A mutation in the protein, resulting in the substitution of a valine resiude at position 2, led to the creation of the enhanced green fluorescent protein (EGFP). EGFP is characterized by its increased stability within cells, higher fluorescence intensity, and reduced cytotoxicity compared to the original protein. Consequently, EGFP has become one of the most frequently utilized tools in molecular and cell biology.[94]

2.3. Bimolecular Fluorescence Complementation Assay.

BiFC studies endorse the structural complementation between non-fluorescent fragments of a fluorescent protein. This involves the intentional splitting of fluorescent proteins at a loop or within a β-strand. Splits sites, between the 8th and 9th β-strands and 7th and 8th β-strands have been widely used as canonical sites for BiFC assays. However, different studies identify the loop between the 10th and 11th β-strands as the optimal split site for BiFC analysis.[95]

Once cleaved, these fragments are able to reassemble, thereby recovering their capability to emit fluorescence when simultaneously expressed in eukaryotic cells. The reassembly occurs by a non-covalent antiparallel β-strand association that is not spontaneous, but occurs if both parts are brought together by, for example, fusing them to two antiparallel leucine zippers.[95]

An example of this type of assay is the one performed by Ghosh, I. et al, in which the reassembly of the well-characterized green fluorescent protein (GFP) protein is studied. In this study the protein was sectioned between residues 157 and 158, that correspond to the canonical site between the 7th and 8th β-strands. From this cleavage resulted two different fragments: a N-terminal fragment containing the first 157 amino acids of the protein (NGFP) and a C-terminal fragment containing the last 81 amino acids of the proteins (CGFP). This strategical cleavage locates the fluorophore in the N-terminal fragment. Besides that, both fragments were tagged with leucine zippers, the fragment NGFP on its C-terminal end, while CGFP was tagged on its N-terminal end, generating NZGFP and CZGFP respectively.

The results obtained in this study showed that the reassembly of the fragments and the subsequent recovery of the protein fluorescence was only possible if both fragments were tagged with leucine zippers, demonstrating that leucine zipper-directed dimerization was essential for the reassembly of the fluorescent protein and fluorophore evolution.[96]

2.4. Precedents.

As it is mentioned in the introduction of this manuscript, one of the greatest capabilities of the IC-Tagging methodology is the validation of protein-protein interactions. Taking advantage of it, and the BiFC studies, our laboratory intended to develop an autofluorescent biosensor to detect efficiently protein retro-translocation using the enhanced version of the GFP protein, EGFP.

The idea is to strategically cleave the EGFP protein and fuse one of these fragments to the IC domain of the muNS-Mi protein. On the other hand, the remaining fragment is fused to a non-fluorescent protein expressed in the ER and labeled with the IC domain too. Thus, the co-expression of both aforementioned constructs with muNS-Mi protein will give rise to two different scenarios: if the selected protein undergoes retro-translocation, it will be transported to the cytosol, where the IC domain will relocate the protein and its fused fragment to the MS if it is not yet degraded. Within the MS, both fragments will come together, allowing the reassembly of the protein and the recovery of its green fluorescence. Conversely, if the protein does not retro-translocate, it will remain in the ER, preventing fragment reassembly and resulting in no fluorescence.

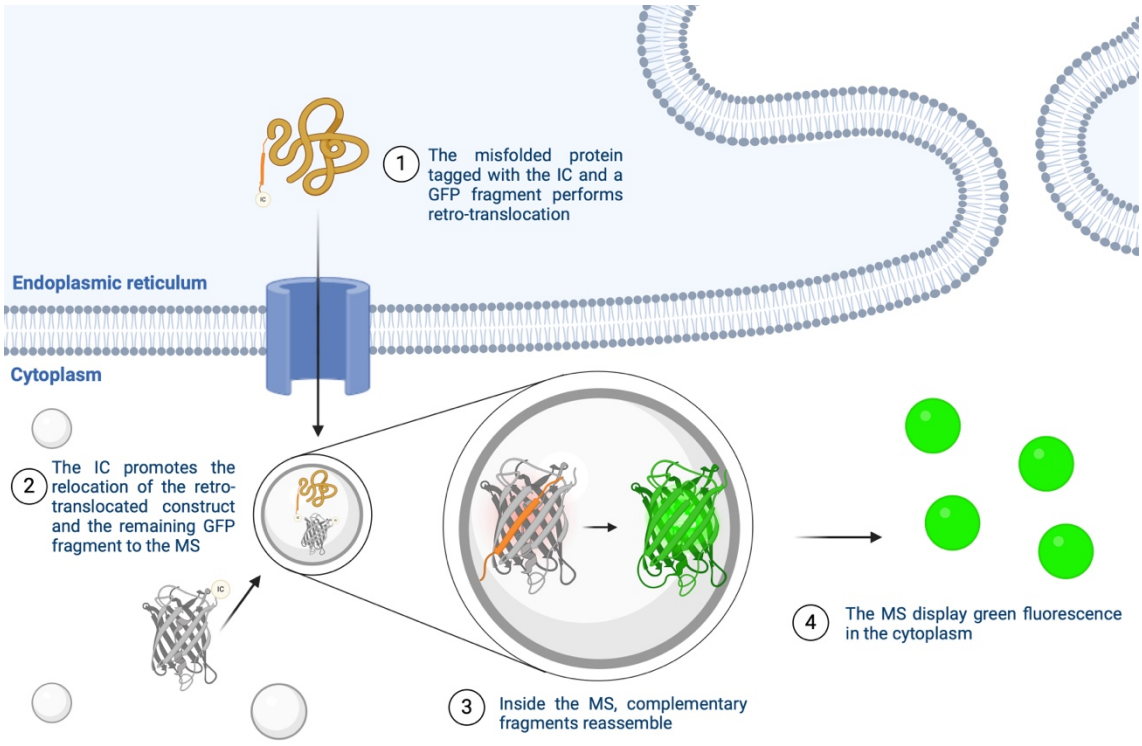

Figure 21. ***Basis of the autofluorescent biosensor performance.***

The first step of the process was the validation of the sensor, in other words, study if the fragments were able to reassemble in the MS independently of the retro-translocation process. To this approach, the EGFP protein was cleaved at the same position mentioned for the assay performed by Ghosh, I. et al. Therefore, the EGFP protein was cleaved in residue 158, generating two fragments: one containing the N-terminal region of the protein named as NEGFP and the one containing the C-terminal region of the protein named as CEGFP.

At this stage, the validation of the sensor was divided in two different strategies: i) tagging the fragment CEGFP with IC and fusing the fragment NEGFP to muNS-Mi and ii) tagging both fragments (CEGFP and NEGFP) with IC and co-expressing them with muNS-Mi. In all cases, the IC tag was alternatively placed at the N or C terminus of each construct, to test if its relative position might influence the outcome of the experiments (Table 1).

Strategy 1	**Strategy 2**
IC-CEGFP	IC-CEGFP
CEGFP-IC	CEGFP-IC
NEGFP-muNS-Mi	NEGFP-IC
muNS-Mi-NEGFP	IC- NEGFP

Table 1. ***Proteins constructs for the two different strategies performed with the aim of validating the sensor.***

Experiments performed in our laboratory revealed that, while Western blot analysis confirmed correct expression and co-expression of all the constructs in DF-1 cells under both strategies, indirect immunofluorescence analysis indicated no reassembly happening with any of the strategies as no fluorescence was observed in cells co-expressing both fragments and muNS-Mi.[97]

At this point a new strategy was introduced: the introduction of a linker sequence between the IC tag and the fragment, to enhance flexibility and facilitate the proper interaction between the GFP fragments within the microsphere. To this approach, the SV5 epitope was used, being introduced between the IC tag and the NEGFP fragment, giving rise to IC-SV5-NEGFP. With this new approach, experiments revealed robust expression of the IC-SV5-NEGFP protein when expressed individually; however, its expression significantly decreased when co-transfected with either of the two different CEGFP fragments. Additionally, indirect immunofluorescence results (not shown) showed that only few of the cells co-transfected with plasmids expressing IC-CEGFP,

IC-SV5-NEGFP, and muNS-Mi emitted MS-localized green fluorescence. This data confirms that although appropriate, the selected strategy was not efficient enough to be utilized as an ER retro-translocation sensor.[97]

2.5. Current strategy.

To increase sensor efficiency, we designed new constructs for the GFP fragments and studied their reassembly within the MS compared to the previous strategy. Our new approach is inspired by a study conducted by Cabantous, S. et al. in which they engineered two new soluble GFP fragments capable of self-association. In this case, the protein is cleaved in between residues 214 and 215 and the last 8 amino acids are deleted because they are not essential for the emission of fluorescence. This strategy generates two different fragments, the N-terminal fragment named as GFP-1-10, comprising the first 214 amino acids of the protein and the C-terminal fragment, GFP-11, containing only the last 15 amino acids of the protein.[98]

Several pairs of mutated fragments based on the aforementioned cleavage position were generated to find the most accurate split. However, the ones obtaining better solubility and complementation were those including the following mutations: the GFP 1-10 fragment containing mutations S30R, N39I, T105K, E111V, I128T, Y145F, K166T, I167V, I171V, S205T, and the GFP 11 fragment containing mutations L221H, F223Y, and T225N.

Besides the change in the split site, the linker was modified. The SV5 epitope, used as linker in the previous attempts, was replaced by a $(G_4S)_3$ linker, consisting of a sequence of four glycine residues followed by a serine residue, repeated three times. This linker was thought to provide enough flexibility to the molecule without interfering with protein folding. This flexibility is derived from the absence of long chains and aromatic rings in both amino acids.[98]

This strategy gave rise to four different constructs of EGFP fragments with the linker and the IC tag: IC-$(G_4S)_3$-GFP 1-10, GFP 1-10-$(G_4S)_3$-IC, IC-$(G_4S)_3$-GFP 11 and GFP 11-$(G_4S)_3$-IC (Figure 22). From now on, I will refer to them as IC-GFP 1-10, GFP 1-10-IC, IC-GFP 11 and GFP 11-IC to facilitate the reading of the manuscript.

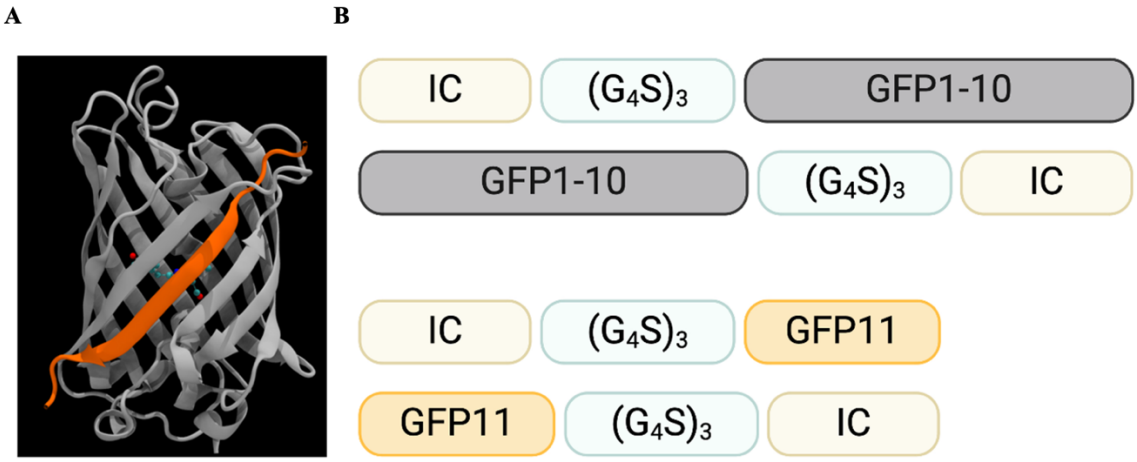

*Figure 22. **A. Three-dimensional structure of the cleaved EGFP.** (PDB:2Y0G from RCSB Protein Data Bank) Amino acids from 1 to 214 (GFP 1 -10) are displayed in gray, while amino acids 215 to 229 (GFP 11) are shown in orange. B. **Schematic representation of the 4 different genetic constructs of the EGFP fragments tagged with the IC domain.***

3. Validation of the sensor.

Once the fragments were designed, the next step was to assess whether they could be used for the development of the sensor or not. Thus, the expression and co-expression of the selected fragments and muNS-Mi have to be endorsed. On top to that, it is crucial to ensure the capability of our constructs to reassemble and recover GFP fluorescence.

For the first purpose, Western Blot analysis of the corresponding transfected cells was performed, while fragment reassembly and fluorescence recovery were ascertained by fluorescence microscopy. Western-Blot analysis was performed using polyclonal antibody against muNS that enables us to detect the IC domain of the different EGFP constructs, as well as muNS-Mi. As we can see in Figure 23, Western-blot analysis revealed the correct expression of the individually expressed constructs (lanes 1-4) and when co-expressed (lanes 5-8), with the exception of the small GFP 11 constructs. These may not be visible either because their small size might lower their retention by the membrane, because they present a very low expression level, because they degrade rapidly or altogether.

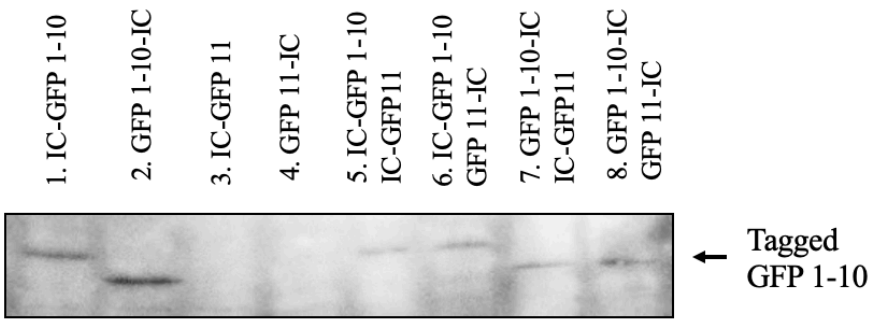

Figure 23. ***Western-Blot analysis of the IC-tagged fragments' expression and co-expressions****. Monolayers of CHO cells were transfected with the plasmid encoding the proteins indicated in the upper part of the image.*

Besides that, the expression and co-expression of the constructs with muNS-Mi was also ascertained. Again, while there was a correct co-expression of GFP 1-10 tagged constructs and muNS-Mi, no GFP 11 constructs could be detected (Figure 24).

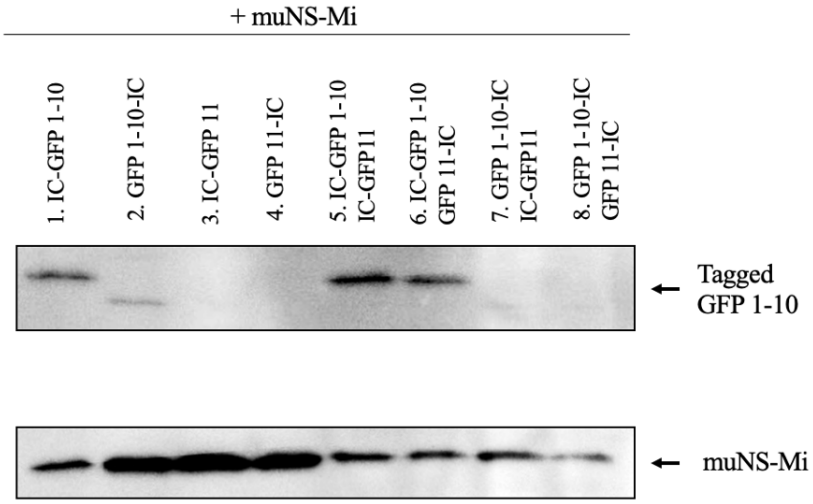

Figure 24. ***Western-Blot analysis of the fragment's expression and co-expressions with muNS-Mi****. Monolayers of CHO cells are transfected with the plasmid encoding the proteins indicated in the upper part of the image*

From Western-Blot analysis we can conclude that even though all the fragments are properly expressed and co-expressed in the presence or absence of muNS-Mi, those tagged in the N-terminal present higher levels of co-expression with muNS-Mi. For this reason, in the further development of the sensor, IC-GFP 1-10 and IC-GFP 11 were chosen.

Next, it was crucial to determine whether the co-expression of the complementary fragments with the muNS-Mi protein drives the reassembly of the protein GFP in the MS and consequently the emission of fluorescence, as expected. To this approach, fragments were first expressed individually and co-expressed in CHO similarly to the previous experiment in the absence of muNS-Mi, to check if GFP could reconstitute from the fragments in the absence of the MS.

As expected, cells expressing individually the fragments did not show any green fluorescence at all (Figure 25 A). However, when co-expressing the GFP complementary fragments in the absence of muNS-Mi, some cells presented fluorescence that was distributed throughout the entire cytoplasm (Figure 25 B). This observation led us to hypothesize two possibilities: either the IC domain has some dimerization ability, allowing the GFP fragments to reassemble independently of muNS-Mi, or the GFP complementary fragments can reassemble by themselves.

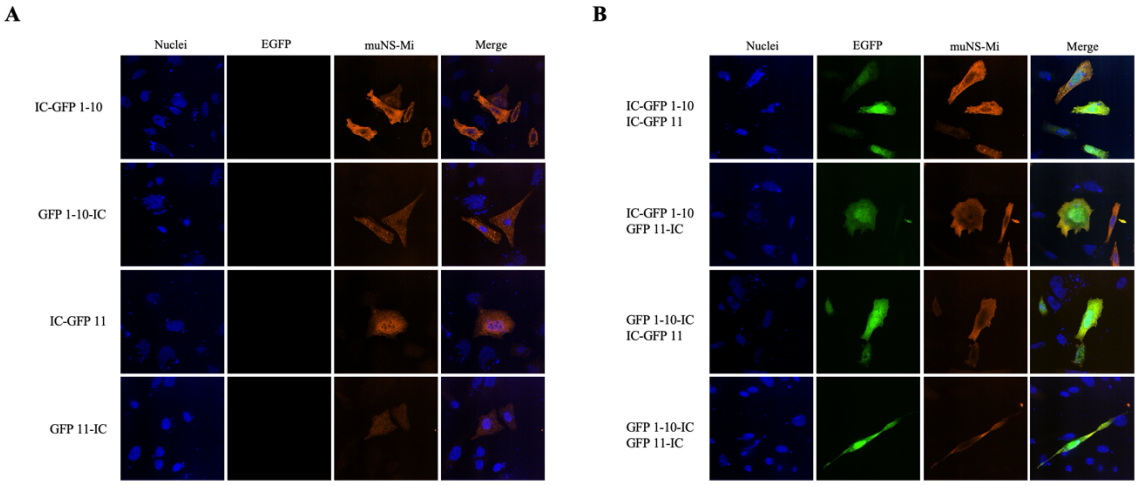

*Figure 25.**Immunofluorescence analysis of the expression and co-expression of EGFP fragments.** EGFP reassembly is detected using its autofluorescence ability, MuNS-Mi is shown in red and nuclei are stained blue with DAPI. **A. Immunofluorescence analysis of the individual expression of EGFP fragments.** Monolayers of CHO cells are transfected with the plasmid encoding the proteins indicated in the left side of the image. **B. Immunofluorescence analysis of the co-expression of EGFP complementary fragments.** Monolayers of CHO cells are co-transfected with the plasmids encoding the proteins indicated in the left side of the image.*

The next step was to co-express the tagged GFP fragments with muNS-Mi. First, in Figure 26 is shown that in all cells expressing muNS-Mi have MS in their cytoplasm. Also, it was observed that, while the individual GFP fragments co-expressed with muNS-Mi presented no GFP fluorescence at all (Figure 26 A), all cells expressing both complementary fragments and muNS-Mi, present green fluorescence that was indeed 100% localized in the MS (Figure 26 B). To summarize, the results obtained in this part of the study demonstrate that the co-expression of muNS-Mi with any of the fragments tagged with Intercoil do not interfere with the ability of muNS-Mi of generating inclusions in the cytoplasm. Also, and more importantly, that the relocation to MS by the IC tag drives the reassembly of GFP from the two complementary fragments, allowing the fluophore evolution and recovering the GFP green fluorescence.

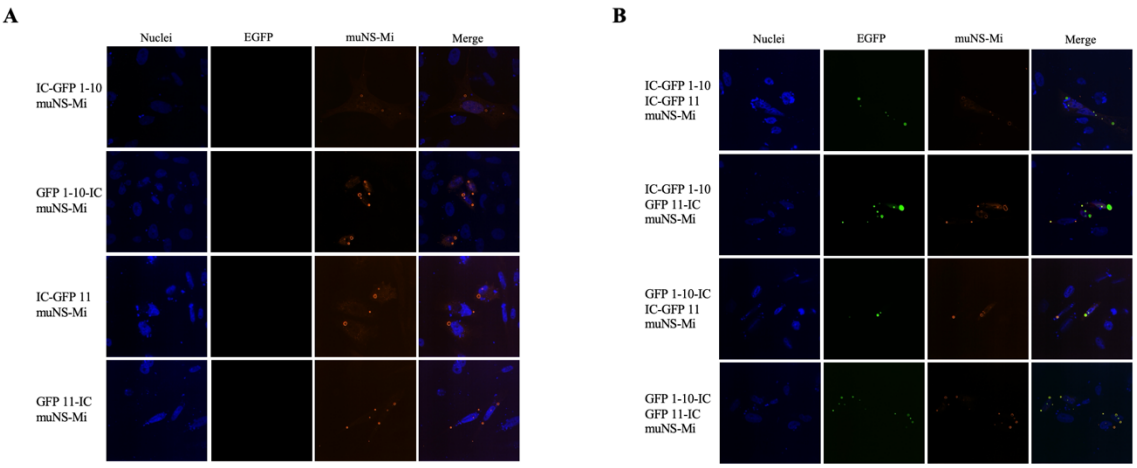

Figure 26. ***Immunofluorescence analysis of the expression of IC-tagged EGFP fragments with muNS-Mi in the presence or absence of the complementary fragments.*** *EGFP reassembly is detected using GFP green autofluorescence, MuNS-Mi is shown in red and nuclei are stained blue with DAPI.* ***A. Immunofluorescence analysis of the individual expression of IC-tagged EGFP fragments with muNS-Mi.*** *Monolayers of CHO cells were co-transfected with the plasmids encoding the proteins indicated in the left side of the image.* ***B. Immunofluorescence analysis of the co-expression of IC-tagged EGFP complementary fragments with muNS-Mi.*** *Monolayers of CHO cells were co-transfected with the plasmids encoding the proteins indicated in the left side of the image*

From the results obtained, we can confirm that the selected strategy enables the reassembly of the fragments both in the presence or absence of muNS-Mi. However, the best choice for the development of the sensor is the co-expression of fragments with muNS-Mi, because this strategy enables us to concentrate the fluorescence in a small space, being easier to recognize. This will be crucial in cases of low subject protein abundancy, where a low level of fluorescence distributed through the whole cell might be difficult to discern from autofluorescence events. Besides that, from Western-Blot results we conclude that those tagged in the N-terminal present higher levels of co-expression with muNS-Mi. For this reason, in the further development of the sensor, IC-GFP 1-10 and IC-GFP 11 were chosen for their co-expression with muNS-Mi. Moreover, we wanted to go one step further and clarify the role of the IC tag in the protein reassembly.

3.1. Clarification of the role of the IC tag in the EGFP reassembly of the fragments.

As previously mentioned, a possible dimerization role of the IC tag remains unclear in this stage of the process. Thus, with the aim of deepening in its role, new constructs were generated for both fragments eliminating the IC tag.

Unfortunately, we were not able to detect any of the fragments individually by Western-blot with any anti-GFP antibody tested and so we used muNS-Mi as an indirect control of transfection instead. Thus, Western-Blot analysis revealed the expression of muNS-Mi when co-transfected

with either one of the fragments (Figure 27, rows 3 and 4) or with both complementary fragments (Figure 27, row 6) although again, no signal was obtained from the GFP constructs..

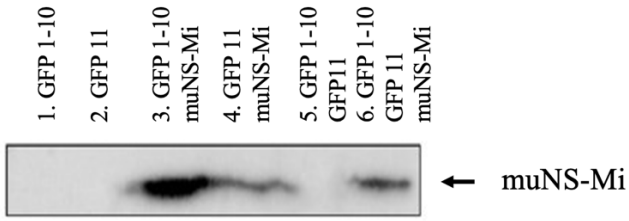

Figure 27. ***Western-Blot analysis of the no-tagged fragments' expression and co-expressions in the presence and absence of muNS-Mi****. Monolayers of VERO cells are transfected with the plasmid encoding the proteins indicated in the upper part of the image.*

Thus, we interpreted that, as transfection proceeded correctly, we could assume that the plasmids for the EGFP fragments have also been transfected and their expression consequently driven. We repeated these expression experiments three times with identical results.

Finally, an immunofluorescence analysis was performed to observe if the reassembly of EGFP occurs when the constructs lack the IC tag. After transfected as above, cells are fixed, immunostained using polyclonal antibody against muNS and observed under the fluorescence microscope. The results showed that there is no detected green fluorescence derived either from the individual expression of the untagged fragments (Figure 28, lanes 1 and 2) or when co-expressed (Figure 28, lane 5). No green fluorescence was neither observed when both complementary GFP untagged fragments were individually (Figure 28, lanes 3 and 4) or together (Figure 28, lane 6) co-expressed with muNS-Mi. On the other hand, muNS-Mi MS were correctly formed in the cytoplasm, as expected (Figure 28, lanes 3, 4 and 6, red channel). Although we cannot rule out the possibility that the untagged fragments are not properly expressed, these results suggest that the fragments themselves are not capable of reassembly, implying that the presence of the IC domain is sufficient for reassembly of the fragments.

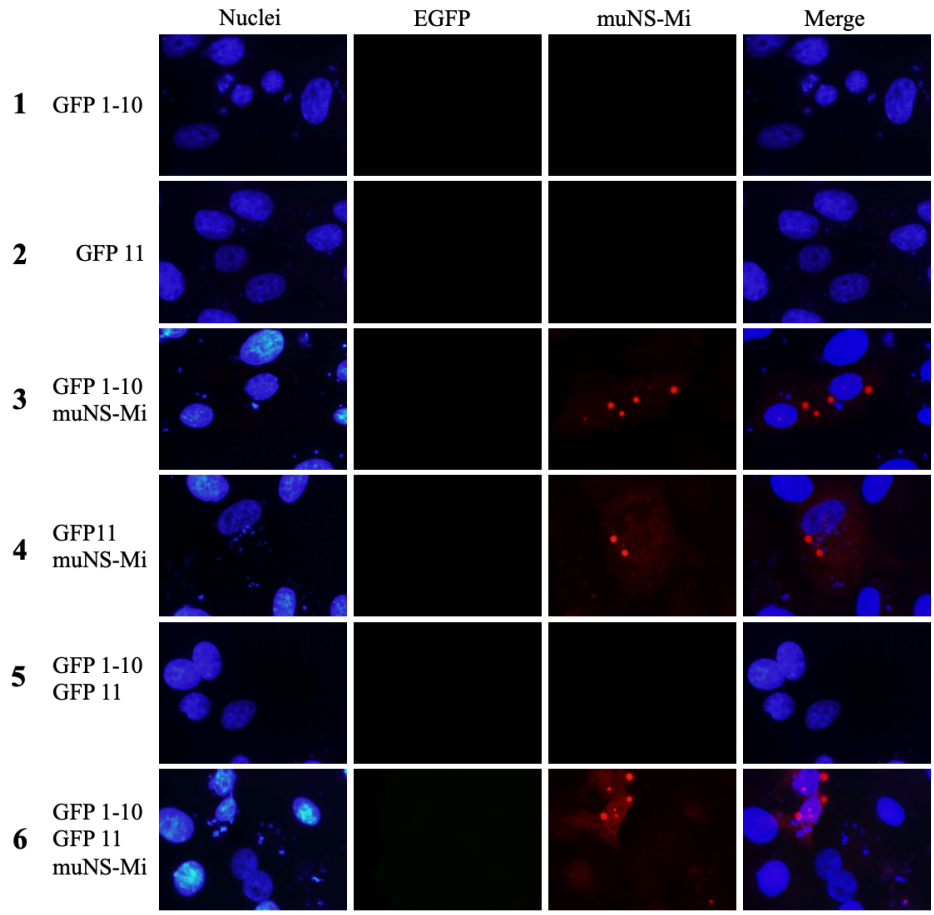

Figure 28. ***Immunofluorescence analysis of the individual expression and co-expression of untagged EGFP fragments in the presence and absence of muNS-Mi.*** *Monolayers of VERO cells were transfected with the plasmid encoding the proteins indicated in the left side of the image. MuNS-Mi is shown in reds and nuclei are stained blue with DAPI.*

Taking all these findings into account, we can conclude that the ideal design for the sensor comprises the expression of two complementary fragments tagged with the IC tag and the muNS-Mi protein. In this scenario, fluorescence is very efficiently rescued and located in very distinct spheres that enables unequivocal identification of EGFP reassembly.

4. Experimental assessment of the retro-translocation of NS1 And NHK-alfa1 antitrypsin.

As described before, NS1 And NHK-alfa1 antitrypsin (NHK- α1AT) are widely used protein models of ERAD. For this reason, they are going to be the object of study in these assays.

First, it was necessary to integrate both proteins into the sensor's gear. For this, new DNA constructs were generated for each protein, starting with a signal sequence named as 'SS' (MGWSLILLFLVAVATGVHSQ), to drive the newly synthesized proteins to the endoplasmic reticulum via Sec61. Besides that, both contain the SV5 epitope (GKPIPNPLLGLD) to use it as

an efficient detection tag. To conclude, both protein sequences were fused to the smaller of the GFP derived fragments, IC-$(G_4S)_3$-GFP 11. This strategy gave rise to the following constructs: SS-NS1-SV5-IC-$(G_4S)_3$-GFP11 and SS- NHK- α 1AT-SV5-IC-$(G_4S)_3$-GFP11 (Figure 29).

Figure 29. ***Schematic representation of the genetic constructions for the introduction of the ERAD models in the sensor gear.***

To properly visualize the retro-translocation of NS1 and NHK- α1 antitrypsin, these constructs need to be co-expressed with the cytosolic EGFP complementary fragment (IC-GFP 1- 10) and muNS-Mi. If the expression and co-expression of the constructs happens and the protein retro-translocate, we would observe green fluorescence located in the MS derived from the reassembly of the EGFP complementary fragments driven by the IC-relocation effect.

The first step to ensure the proper operation of the system, is the assessment of the individual expression of the ERAD substrate constructs and their co-expression with IC -GFP1-10 and muNS-Mi. To this approach we performed Western-Blot analysis using polyclonal antibody against muNS to detect the IC domain of the different EGFP constructs, as well as muNS-Mi, and a monoclonal antibody against SV5 to detect the ERAD models constructs.

Western-Blot analysis revealed that there are good levels of expression of both ERAD models individually (Figure 30 A, B, lane 1) and when they are co-expressed with IC-GFP1-10 (Figure 30 A, B, lane 2), with muNS-Mi (Figure 30 A, B, lane 3) and both (Figure 30 A, B, lane 4).

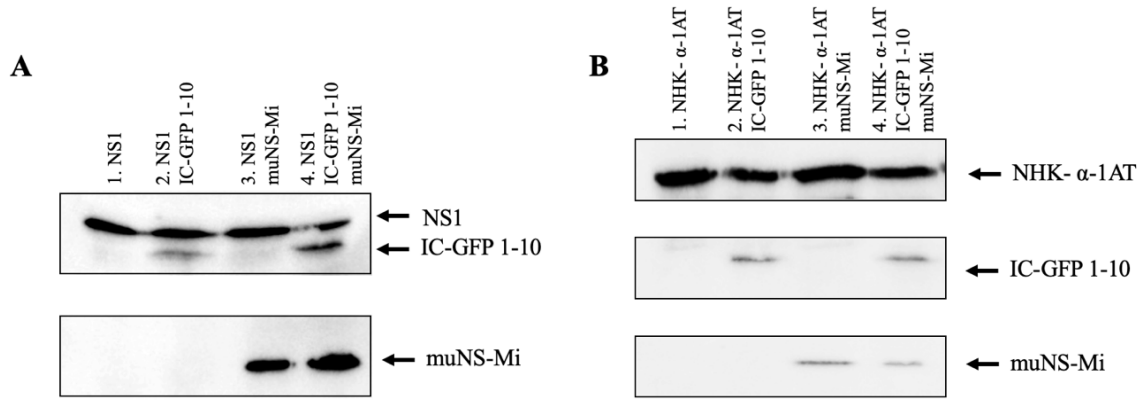

Figure 30. ***Western-Blot analysis of the ERAD models' expression.*** *Monolayers of CHO cells were transfected with the plasmids encoding the proteins indicated in the upper part of the image.* ***A. Western-Blot analysis of the expression and co-expression of NS1. B. Western-Blot analysis of the expression and co-expression of NHK- α 1 antitrypsin.***

Once the expression and co-expression of the ERAD substrate constructs is endorsed, we proceeded to follow up the protein retro-translocation process through fluorescence microscopy. To this end, cells of three different cell lines (CHO, HEK293 and VERO) were transfected with the plasmids encoding the ERAD models and the sensor's machinery. After that, cells were fixed and immuno-labelled with monoclonal antibody against SV5. The results showed in Figure 31 and Figure 32 demonstrated that both ERAD models displayed a similar behavior, and such behavior was independent of the cell line used. First, the cells expressing each of the ERAD models individually, presented antibody-derived red fluorescence consistent with an ER and cytosol localization (Figure 31 and Figure 32 A, B and C, lane 1). When cells expressing the ERAD models were co-expressed with IC-GFP 1-10, a green fluorescence distributed through the whole cell is observed, indicating the cytosolic reconstitution of EGFP from its fragments. These results further suggest that, at least some of the ERAD models constructs, are located in the cytosol, confirming their retro-translocation (Figure 31 and Figure 32, A, B and C, lane 2). Also as expected, the red and green fluorescence are not fully co-localizing, showing that two populations of the expressed constructs co-exist in the same cell, presumably one inside the ER and the other in the cytosol. Next, those cells co-expressing each of the ERAD models with muNS-Mi but no IC-GFP 1-10, showed no green fluorescence as it was presumable Figure 31 and Figure 32, A, B and C, lane 3). Finally, in both cases the co-expression of the ERAD model with the complementary fragments and muNS-Mi gives rise to green fluorescence neatly located in the MS (Figure 31 and Figure 32, A, B and C, lane 4).

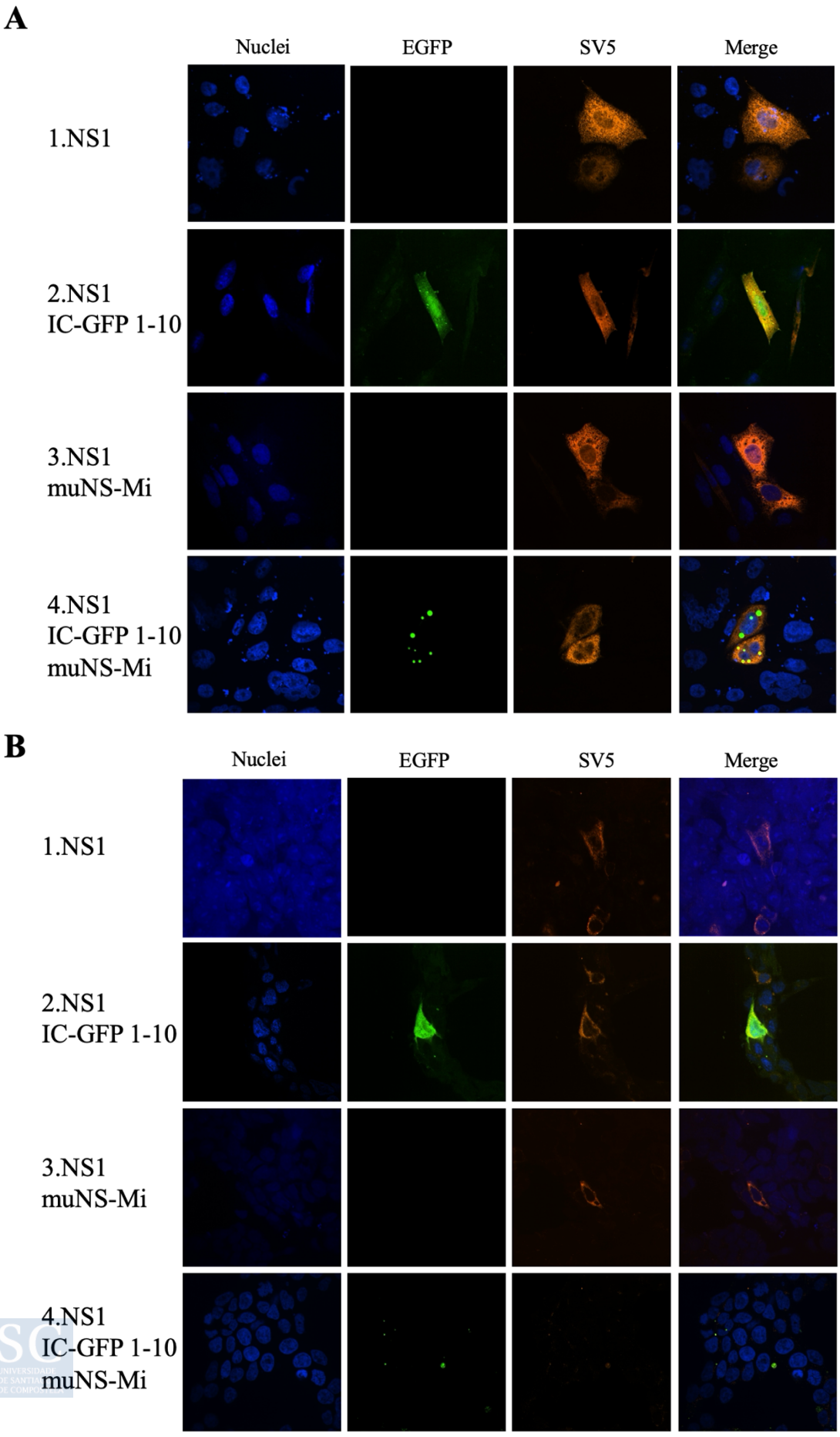

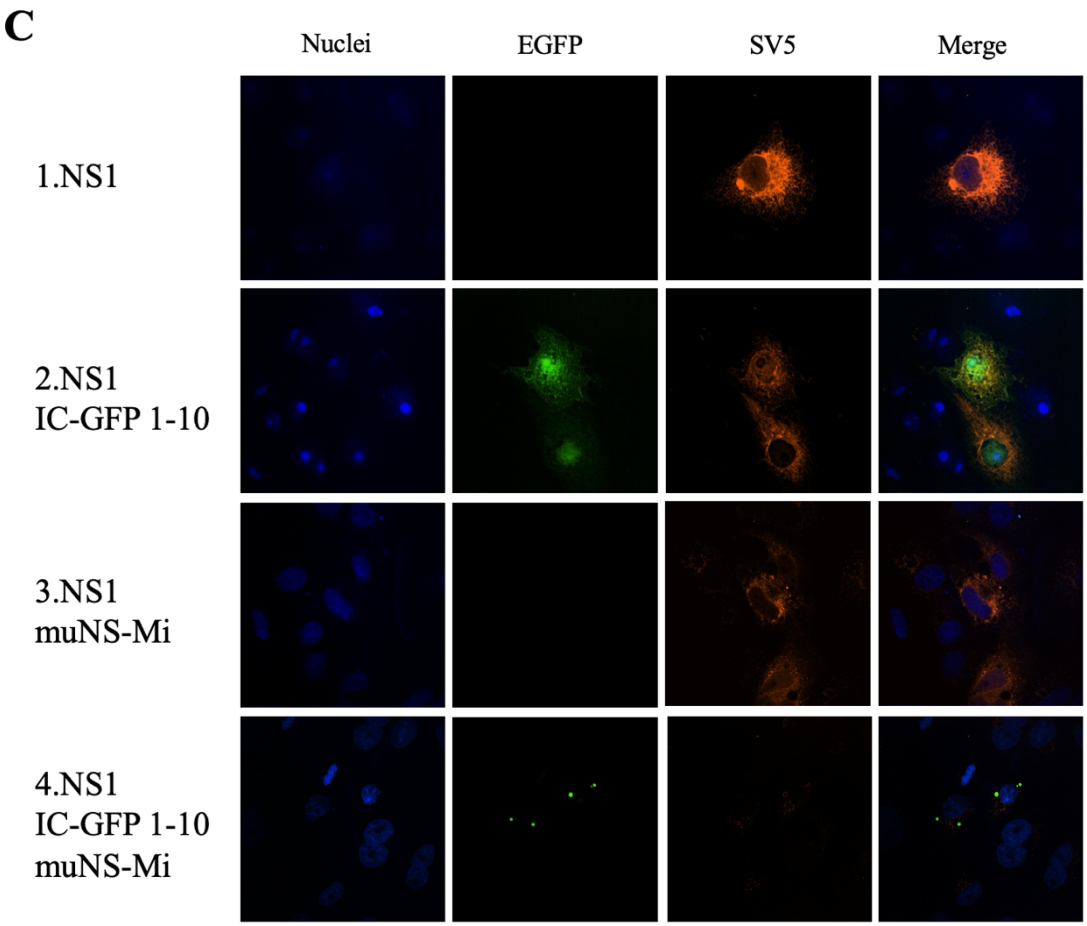

Figure 31. ***Immunofluorescence analysis of the individual expression and co-expression of NS1 constructs with IC-GFP 1-10, muNS-Mi or both of them in different cell lines.*** *EGFP reassembly is detected using the EGFP autofluorescence, MuNS-Mi is shown in red, and nuclei are stained blue with DAPI.* ***A****. Monolayers of CHO cells were transfected with the plasmids encoding the proteins indicated in the left side of the image.* ***B****. Monolayers of HEK293 cells were transfected with the plasmids encoding the proteins indicated in the left side of the image.* ***C****. Monolayers of VERO cells are transfected with the plasmids encoding the proteins indicated in the left side of the image.*

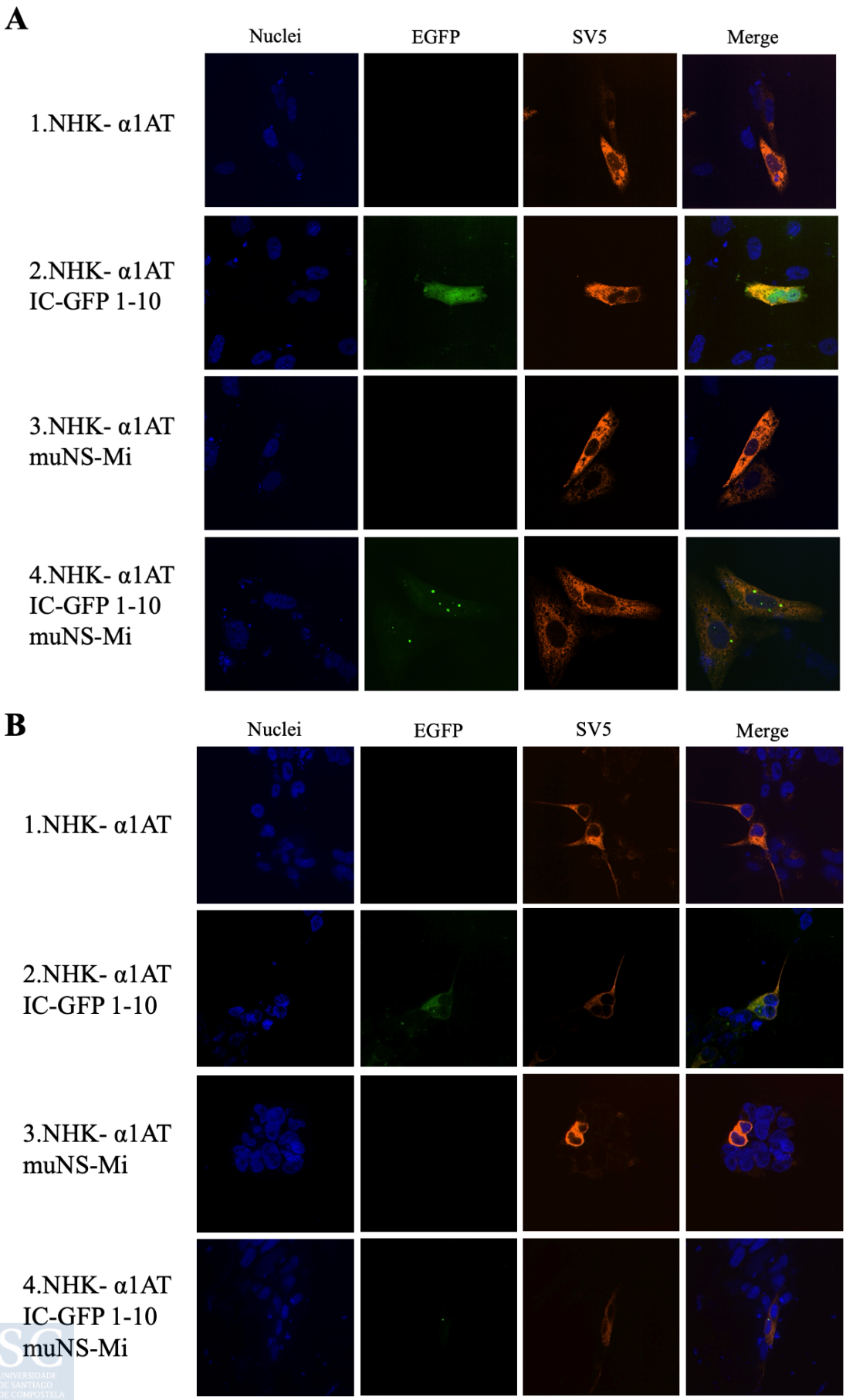

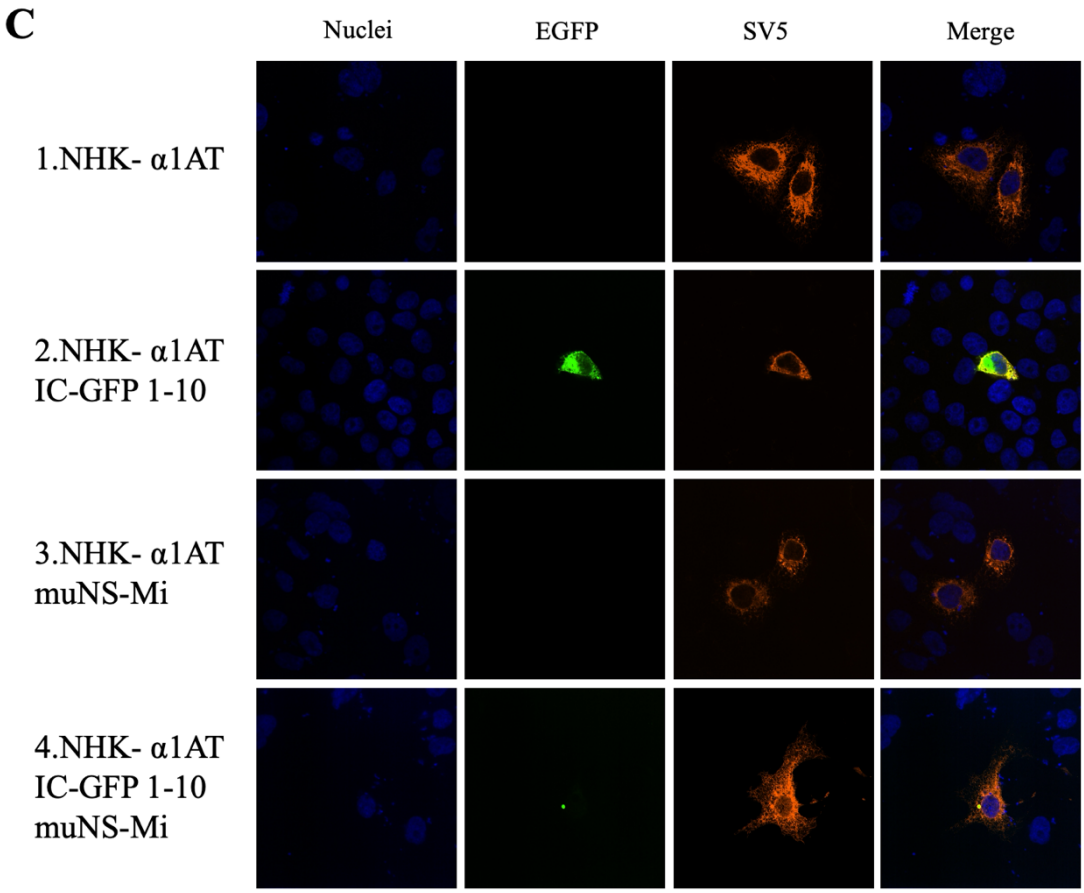

Figure 32. ***Immunofluorescence analysis of the individual expression and co-expression of NHK- α1 antitrypsin with IC-GFP 1-10, muNS-Mi, or both of them in different cell lines.*** *EGFP reassembly is detected using the autofluorescence of EGFP, MuNS-Mi is shown in red, and nuclei are stained blue with DAPI.* ***A****. Monolayers of CHO cells are transfected with the plasmids encoding the proteins indicated in the left side of the image.* ***B****. Monolayers of HEK293 cells are transfected with the plasmids encoding the proteins indicated in the left side of the image.* ***C****. Monolayers of VERO cells are transfected with the plasmids encoding the proteins indicated in the left side of the image.*

From this outcome we can extract that the selected proteins do retro-translocate and, that once in the cytosol, IC-tagged fragments are able to co-localize in the MS and drive the EGFP reassembly, thus being perfectly localized and easily distinguishable from the cell's autofluorescence. The results demonstrated that the IC-Tagging system in combination with BiFC are able to efficiently detect the retro-translocation of NS1 and NHK-alfa1 antitrypsin.

5. Proteasome inhibition increases retro-translocated protein accumulation in the cytosol.

The shown reassembly of EGFP in the MS should be proportional to the amount of ERAD substrates that are dislocated to the cytosol but not yet degraded by the proteasome 26S. Thus, we tested the effect of a proteasome inhibitor, MG-132 (Figure 33) on the detection of the retro-translocated ERAD models. Therefore, the inhibition of the proteasome is expected to produce a

significant accumulation of non-degraded protein in the cytosol, leading to a major number of MS displaying green fluorescence, in turn indicating the specificity of the sensor detection.

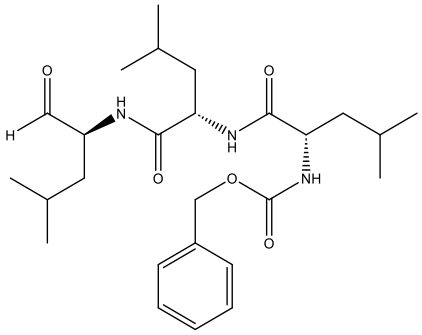

Figure 33. Chemical structure of MG-132.

The first step to observe this effect was to ensure that our system works also in the presence of the proteasome inhibitor. To this approach, cells transfected with either NS1, NHK- α1AT, IC-GFP1-10 and muNS-Mi were incubated with the proteasome inhibitor (10 μM) for 4 hours. After incubation, cells were fixed and immuno-labelled with monoclonal antibodies against SV5. Observation of the treated cells under the fluorescence microscope showed than they follow the same pattern as they do in the absence of the inhibitor in the three different cell lines. Thus, those cells expressing the ERAD models individually presented antibody-derived red fluorescence (Figure 34 and Figure 35, lane 1). In combination with IC-GFP 1-10, the cells presented green fluorescence distributed through the whole cell (Figure 34 and Figure 35,,lane 2). Again, cells co-expressing the ERAD models with only muNS-Mi had no green fluorescence at all (Figure 34 and Figure 35, lane 3), while the co-expression of the ERAD model, IC-GFP 1-10 and muNS-Mi gives rise to intense green fluorescence located in the MS (Figure 34 and Figure 35, lane 4).

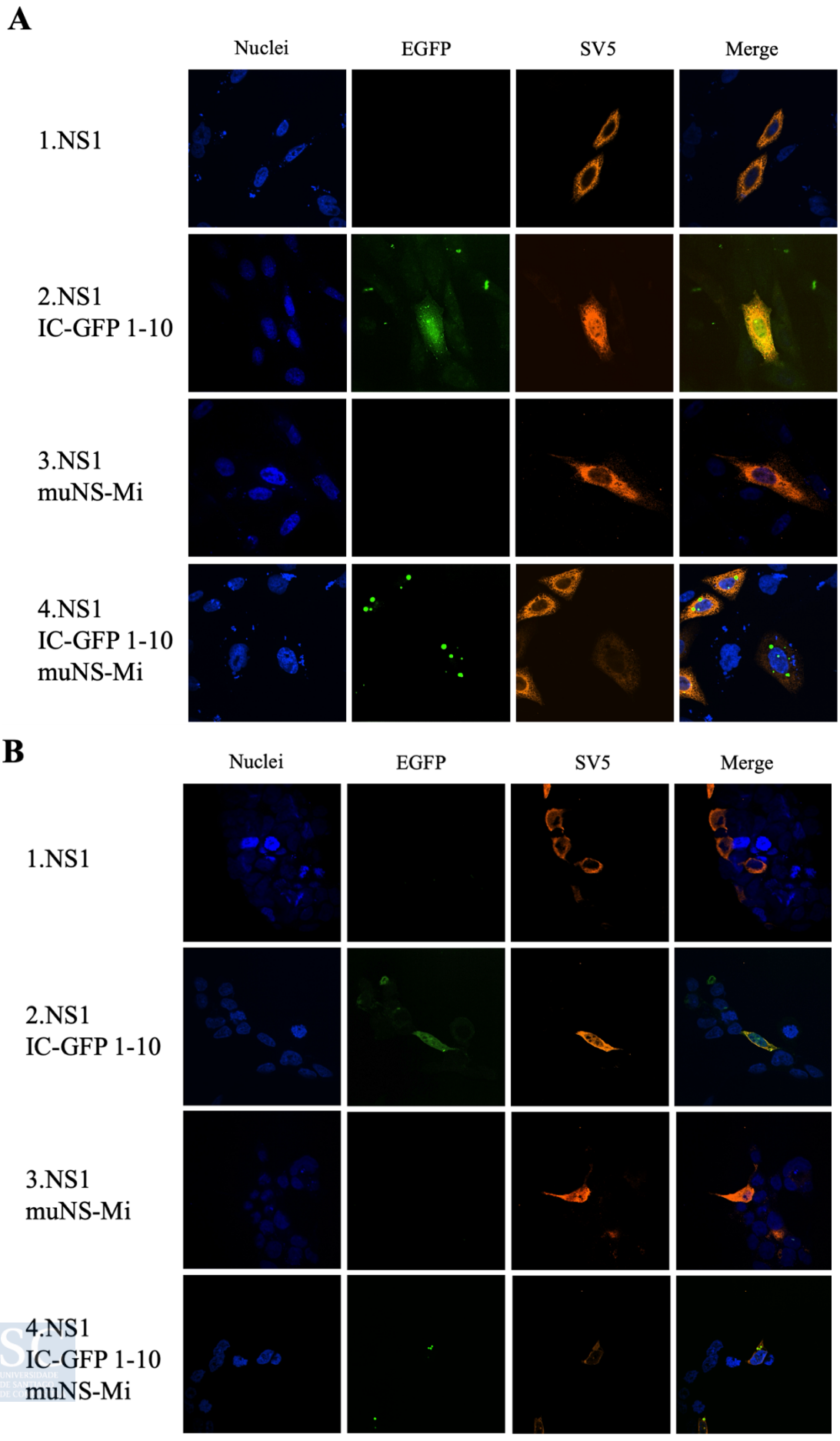

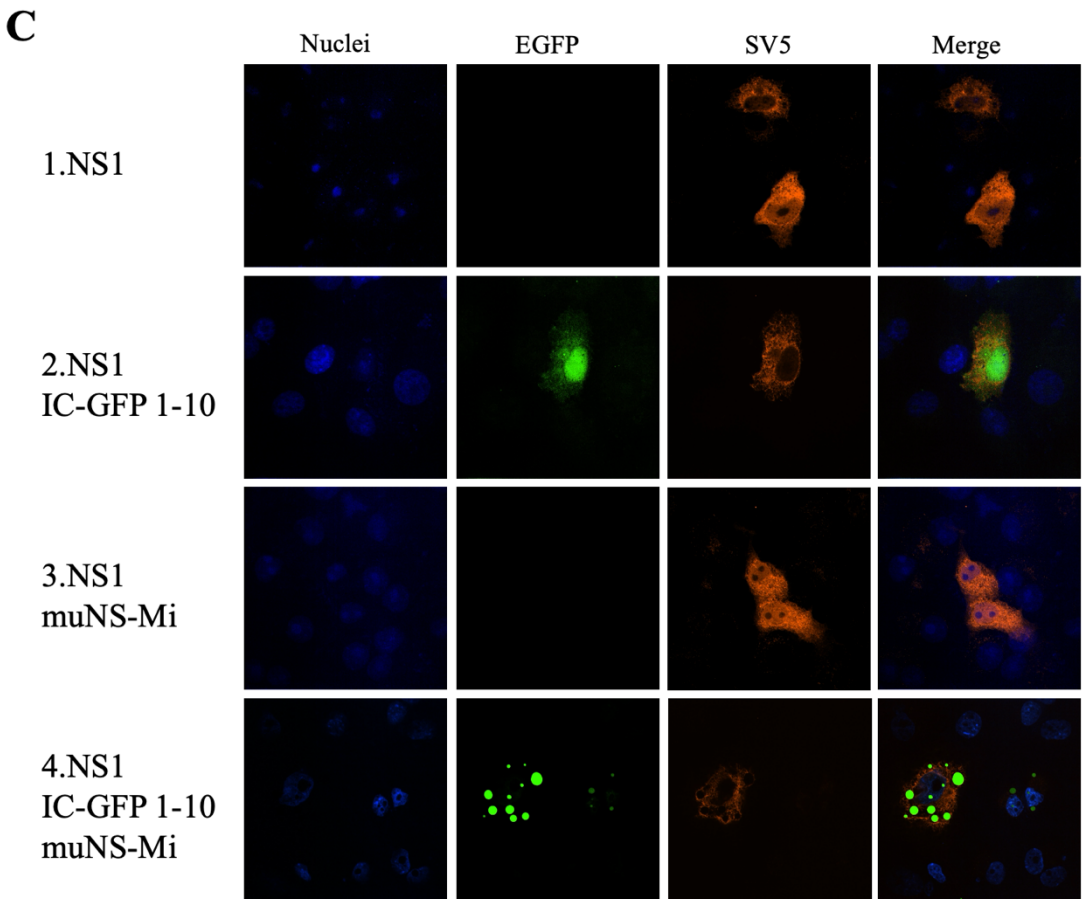

Figure 34. ***Immunofluorescence analysis of the individual expression and co-expression of NS1 with IC-GFP 1-10, muNS-Mi, or both of them in the presence of a proteasome inhibitor in different cell lines.*** *EGFP reassembly is detected using the EGFP autofluorescence, MuNS-Mi is shown red and nuclei are stained blue with DAPI.* ***A****. Monolayers of CHO cells are transfected with the plasmids encoding the proteins indicated in the left side of the image.* ***B****. Monolayers of HEK293 cells are transfected with the plasmids encoding the proteins indicated in the left side of the image.* ***C****. Monolayers of VERO cells are transfected with the plasmids encoding the proteins indicated in the left side of the image.*

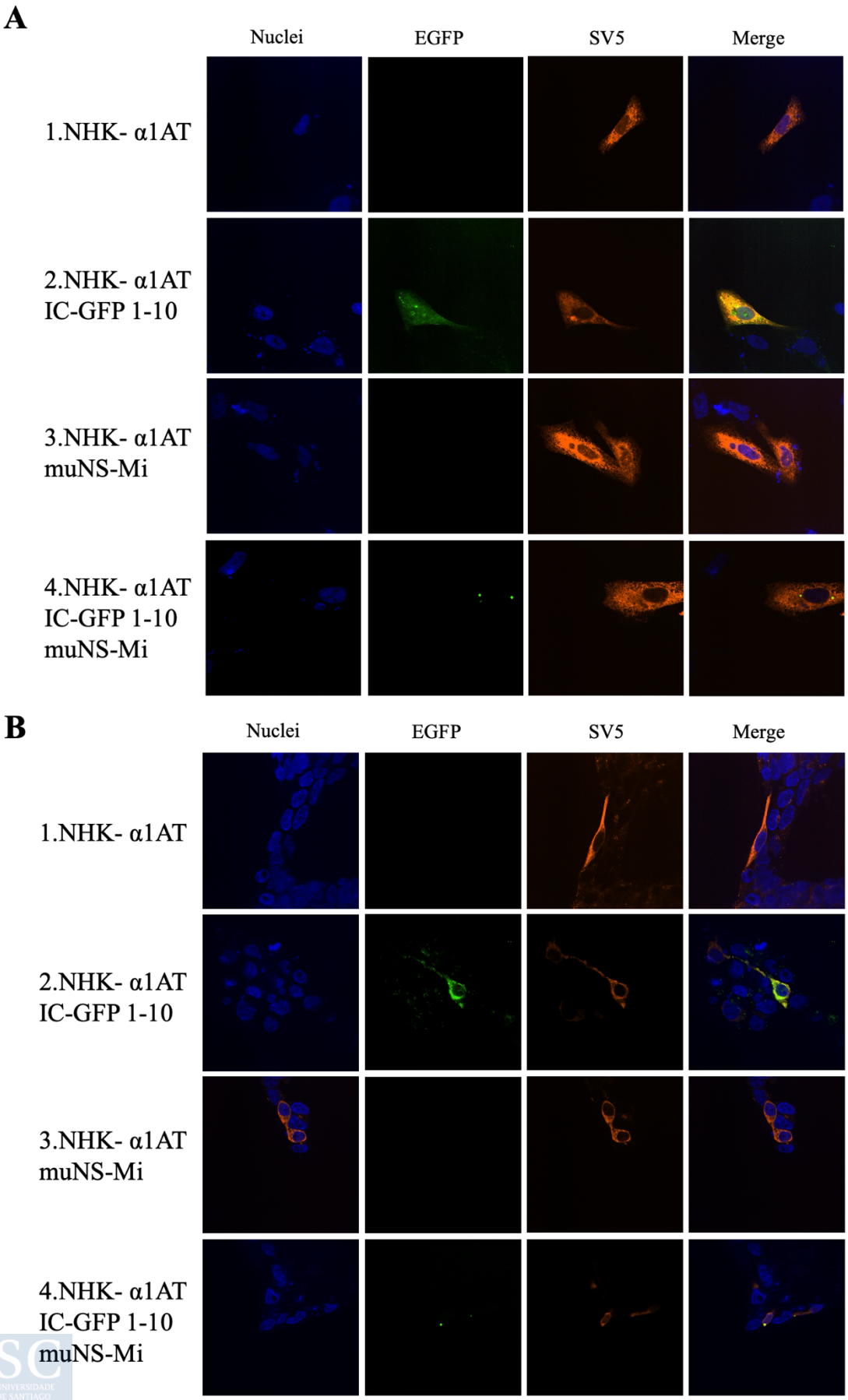

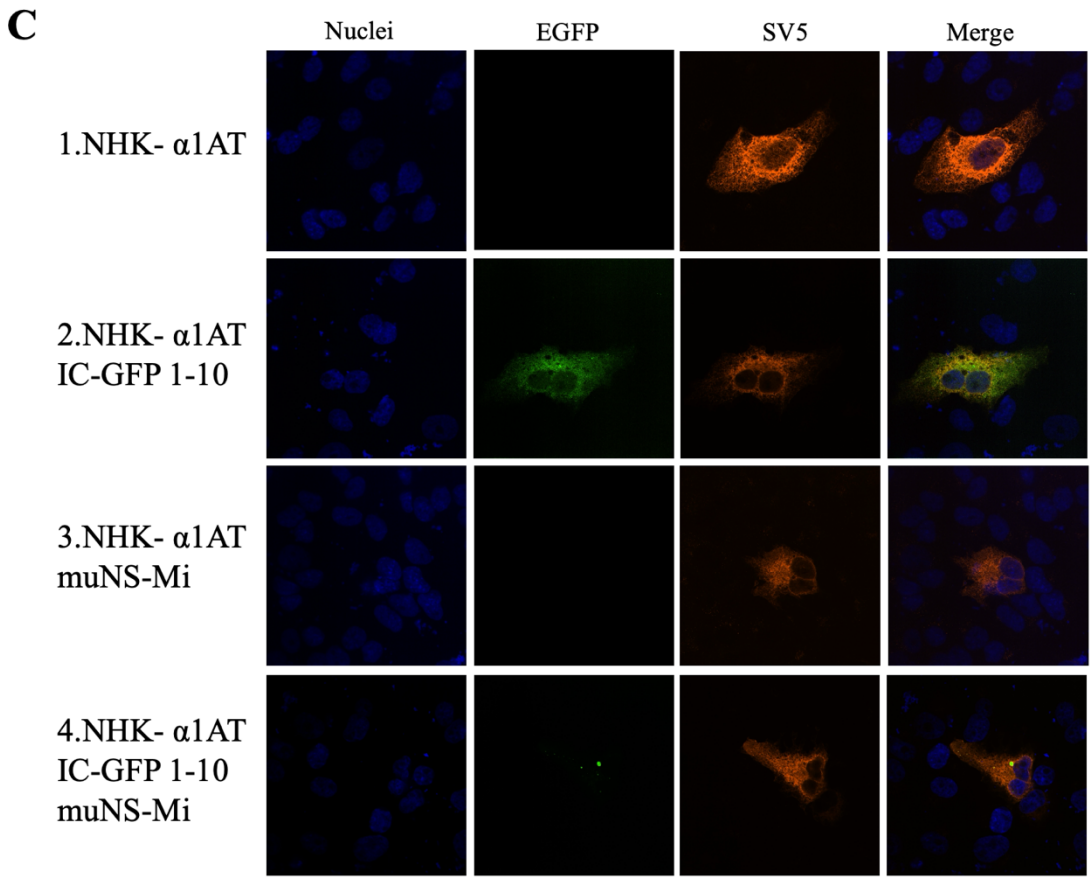

Figure 35. ***Immunofluorescence analysis of the individual expression and co-expression of NHK- α1 antitrypsin with IC-GFP 1-10, muNS-Mi, or both of them in the presence of a proteasome inhibitor in different cell lines.*** *EGFP reassembly is detected using the EGFP autofluorescence, MuNS-Mi is shown red, and nuclei are stained blue with DAPI.* ***A****. Monolayers of CHO cells are transfected with the plasmids encoding the proteins indicated in the left side of the image.* ***B****. Monolayers of HEK293 cells are transfected with the plasmids encoding the proteins indicated in the left side of the image.* ***C****. Monolayers of VERO cells are transfected with the plasmids encoding the proteins indicated in the left side of the image.*

Once the sensor's applicability in these conditions is proved, Western Blot analysis was performed to assess the difference in the cellular protein content either in the presence or absence of proteasome inhibitor. As before, transfected cells with either NS1 and NHK- α1AT, IC-GFP1-10 and muNS were incubated with the proteasome inhibitor (10 μM) for 4 hours. After incubation, cell extracts were used to perform Wester-Blot assay. Monoclonal antibody against SV5 was used to detect the ERAD model constructs and monoclonal antibody against GAPDH were used to normalize all expressions.

The Western-Blot confirmed that, in most cases, the proteasome inhibition increased the level protein content of both ERAD models when expressed individually or when they are co-expressed in the three different cell lines, as expected. Such increase, that corresponds to the non-degraded cytosolic fraction of the protein that has already dislocated from the ER, was very evident for NS1 when expressed in HEK and VERO cells (Figure 36B and C, upper rows) but less clear in

CHO cells (Figure 36A, upper row). The differences in protein abundance were not so evident for NHK- α1AT in all cells tested, although consistently shown by densitometric analysis of the Western-blot patterns (Figure 36A, B, C, lower rows).

A

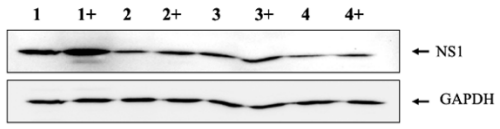

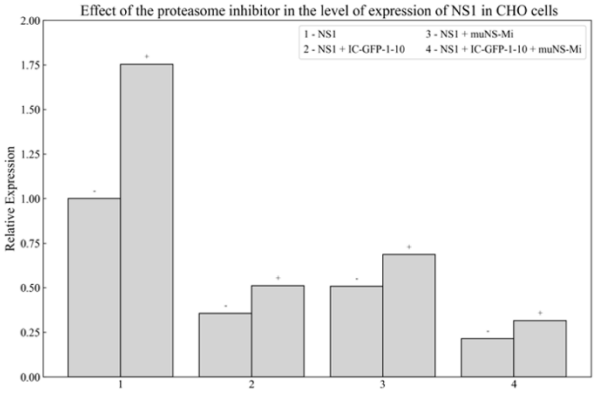

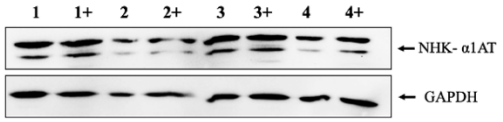

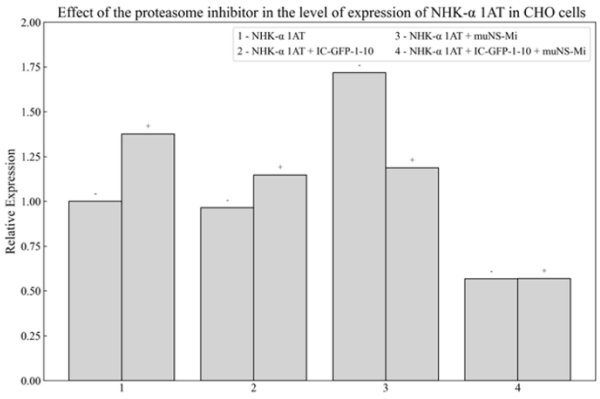

B

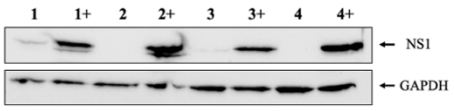

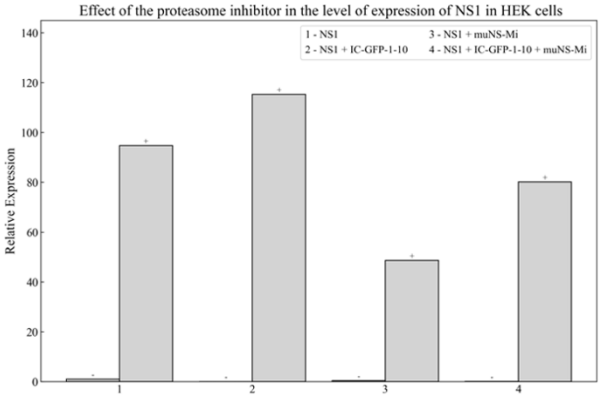

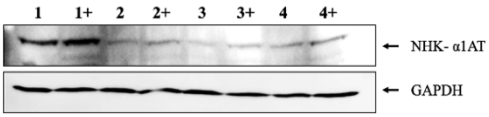

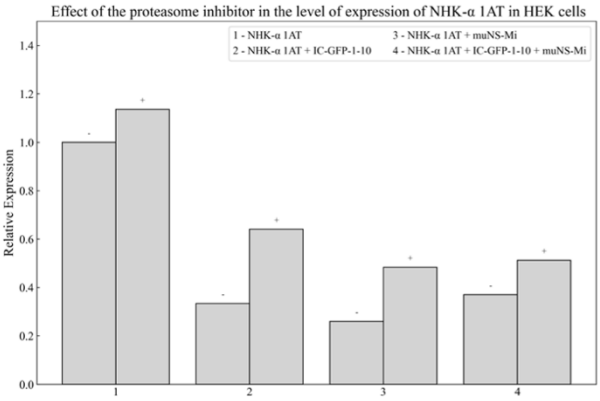

C

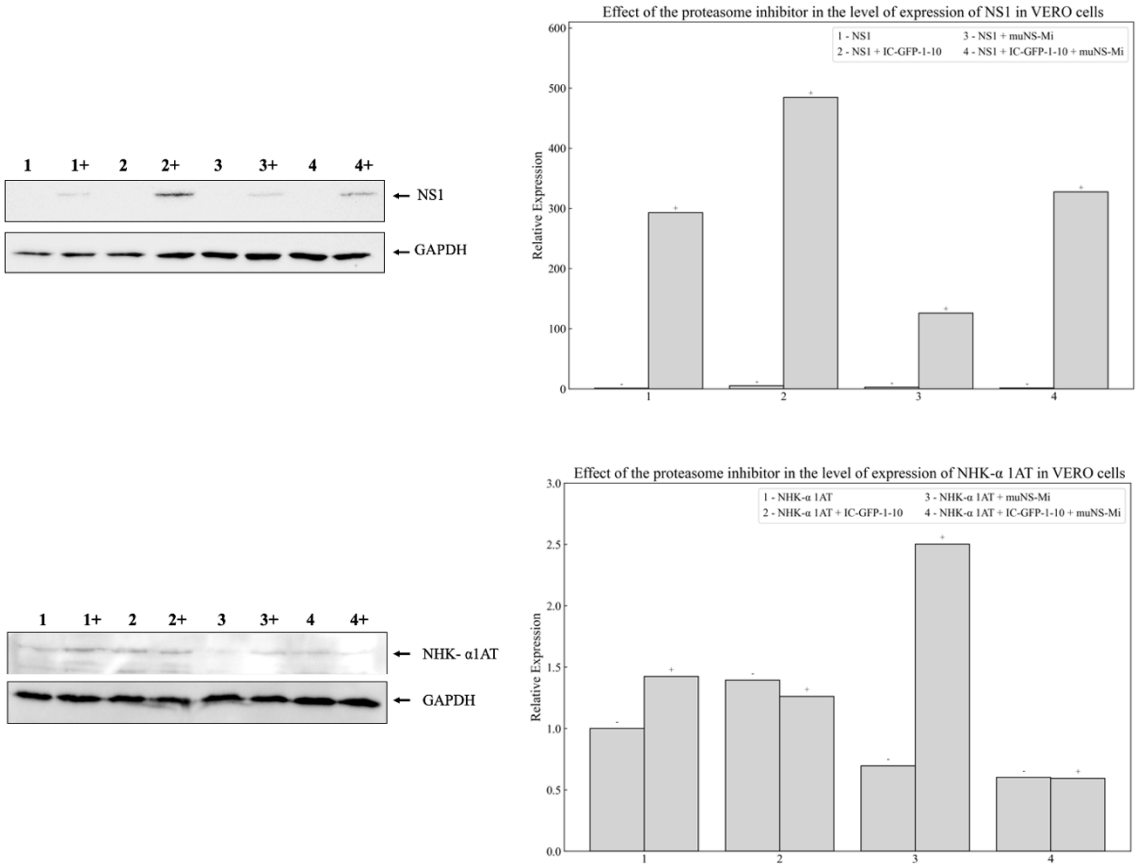

Figure 36. ***Analysis of the changes in the ERAD models cellular content induced by MG-132 by Western-Blot****. Western-blot results of cell extracts of CHO (A), HEK293 (B) and VERO (C) cells and their relative protein content shown by densitometric analysis of the images shown after GAPDH normalization. Data showing '+' above refers to those cells treated with MG-132*

Next, flow cytometry analysis was performed to check if we could quantitatively study the effect of the proteasome inhibitor by means of fluorescence recovery by IC-tagging. Thus, as before, cells transfected with plasmids that direct the expression of either NS1or NHK- α1AT, together or not with IC-GFP1-10 and muNS-Mi, were also alternatively incubated with the proteasome inhibitor (10 μM) for 4 hours. After incubation, cells were harvested and subjected to flow cytometry analysis. The results obtained for the three different cell lines for both ERAD models show a clear pattern (Figure 37). In all the cases the fluorescence displayed by cells co-expressing the ERAD model, IC-GFP1-10 and muNS-Mi undergoes a relevant increase in the presence of the proteasome inhibitor. This effect is also shown in most cells co-expressing each ERAD model and IC-GFP1-10, with the exceptions of NHK- α1AT in HEK cells (Figure 37 B, right panel, lane 2) and NS1in Vero cells (Figure 37 C, left panel, lane 2). On the opposite, the controls did not present relevant variations in fluorescence. Thus, the increase in the fluorescence derived from proteasome inhibition is more reliably detected when the fluorescence is accumulated and concentrated in the MS.

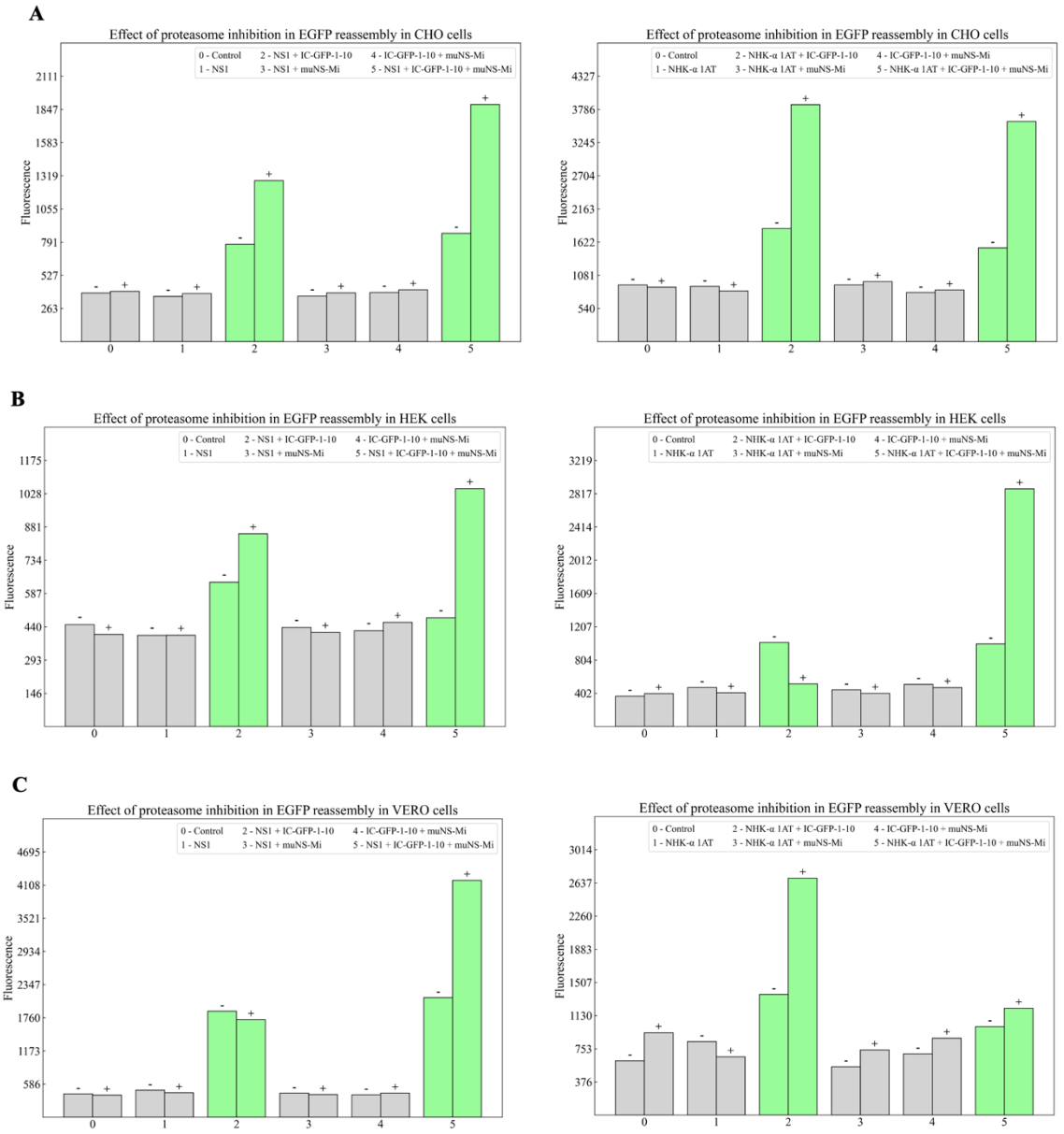

Figure 37. ***Analysis of the changes in EGFP reassembly for both ERAD models in different cell lines****. Cytometry results for EGFP reassembly in CHO (A), HEK293 (B) and VERO (C) for NS1 (left) and NHK- α1AT (right).*

When, instead of measuring total fluorescence, we compared the number of fluorescent events in our cell populations (Figure 38), we observed that the proteasome inhibitor induced an increase in the number of cells that present fluorescence in the majority of the cases. This result is shared by both ERAD models in the three different cell lines but again, the result is more consistent when muNS-Mi is present as, for the same samples as before where muNS-Mi was not present, NHK-α1AT in HEK cells (Figure 38 B, right panel, lane 2) and NS1in VERO cells (Figure 38 C, left panel, lane 2), the results did not match the logic, expected results and a bigger signal was obtained in the absence of the inhibitor.

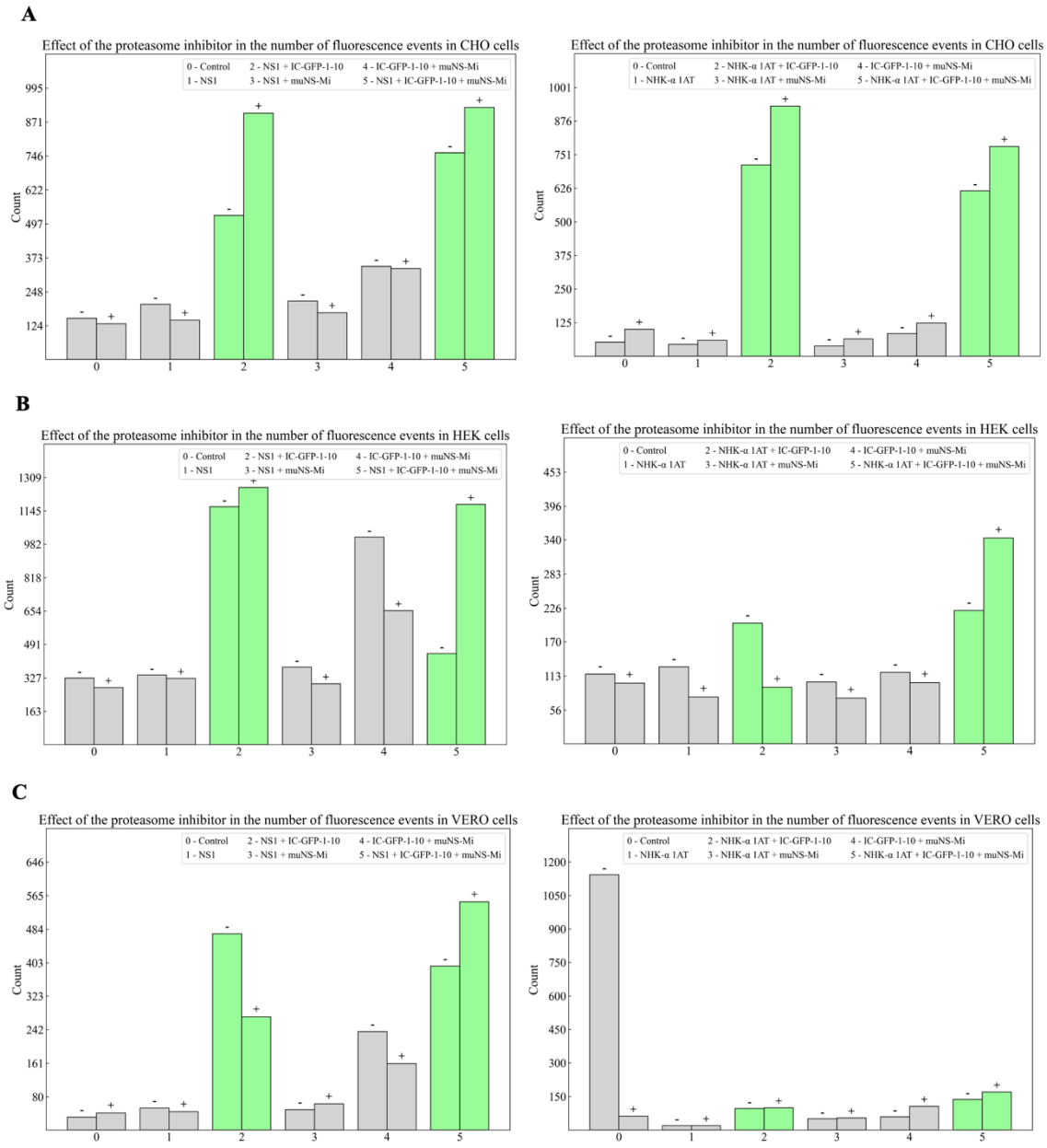

Figure 38. ***Analysis of the changes in the number of fluorescence cells for both ERAD models in different cell lines****. Cytometry results in CHO (A), HEK293 (B) and VERO (C) for NS1 (left) and NHK- α1AT (right).*

Results shown in this section confirms that the sensitivity of the designed fluorescent sensor is not only capable of detecting the effect provoked by the proteasome inhibitor, but also allows a reliable quantification of the retro-translocated proteins that outperforms the Western-blot analysis for this particular application.

6. Discussion.

We can confirm that the new strategy chosen, specifically the selected cleaving site and the insertion of a flexible linker sequence between the IC and the EGFP fragment, enables the

reassembly of EGFP. This reassembly occurs either inside the MS when muNS-Mi is expressed or in the cytoplasm in the absence of muNS-Mi.

Besides that, the IC domain has been demonstrated to have an essential role in the EGFP reassembly, becoming a key player in the sensor's machinery. We hypothesize that this behavior corresponds to an auto-oligomerization promotion of the IC, although further confirmation is required.

The proposed strategy was tested for creating a sensor to detect retrotranslocation models. Results showed that insertion of the ERAD models NS1 and NHK- α1AT in the sensor's gear does not have any impact in the formation of the MS and neither in the reassembly of the EGFP fragments. In addition, the system is able to detect the retrotranslocation of the models and offers easy visualization by concentrating the green fluorescence in a very distinguishable and small space inside the living cell. Moreover, the sensor works efficiently in the presence of a proteasome inhibitor, detecting the protein accumulation of ERAD substrate by changes in cellular protein content and cellular fluorescence.

Considering these results, we can definitively conclude that the selected strategy for the EGFP reassembly is suitable for the design of an autofluorescent biosensor. Besides that, in the specific case of the retro-translocation process, the system offers enough sensitivity to detect the differences in the protein amount provoked by the proteasome inhibition and a reliable way of measuring such differences.

To sum up, our system presents a simple, efficient, and reliable way to detect dislocated molecules either in the presence or absence of proteasome inhibitor. Furthermore, it presents great advantages in front other detection methods. Our sensor does not require the separation of the cytosolic fraction and the coupled degradation has been demonstrated no to impede in the detection of dislocated substrates. Hence it can be considered an appropriate alternative to build up in-vitro cell sensors

CHAPTER II. CANCER VACCINE CANDIDATE DEVELOPMENT USING PROTEIN-BASED PARTICLES.

CHAPTER II. CANCER VACCINE CANDIDATE DEVELOPMENT USING PROTEIN-BASED PARTICLES.

This chapter is the result of a collaboration with the laboratory of Dr. Sandra Diebold at the Medicines and Healthcare products Regulatory Agency (MHRA) in the United Kingdom. Experiments related with the immunostimulatory activity of the vaccine candidate were performed in their site in South Mimms (UK).

1. Introduction.

1.1. Cancer immunotherapy and vaccination.

William B. Coley, who is currently known as the father of immunotherapy, first attempted to harness the immune system's power for cancer treatment in the late 19th century. As an orthopedic surgeon, he observed spontaneous tumor regression in patients with postoperative wound infections. Coley decided to inject over a thousand patients with a mixture of live and inactivated bacteria, known as "Coley's toxin", aiming to induce strong immune and antitumor responses. This event is considered as the first documented cancer immunotherapy. While achieving durable complete remissions, the lack of a known mechanism for Coley's toxin and the risks associated with infecting cancer patients with pathogenic bacteria led oncologists to adopt surgery and radiotherapy as alternative standard treatments in the early 20th century.[99] However, in the last decades immunotherapy has emerged as a fast-growing area in the whole pharmaceutical industry. Specifically, in the field of cancer treatment, immunotherapy is currently attracting the attention of the scientific community due to its promising perspective. These therapies fall into several classes, from CAR-T cells to cancer vaccines. Despite progress in the field, cancer immunotherapy still faces serious challenges regarding mainly to safety issues.

One of the approaches that is gaining the spotlight is the vaccination against unique tumor associated antigen or neoantigens, due to the current landscape in their predicting tools and the decrease in the cost of next-generation sequencing. These vaccines consist of a formulation which usually include a strong adjuvant, or it is adjuvant itself, and tumor proteins or peptides which prime the immune system.[100,101] Figure 39 shows a schematic representation of the pathway followed by these vaccines.

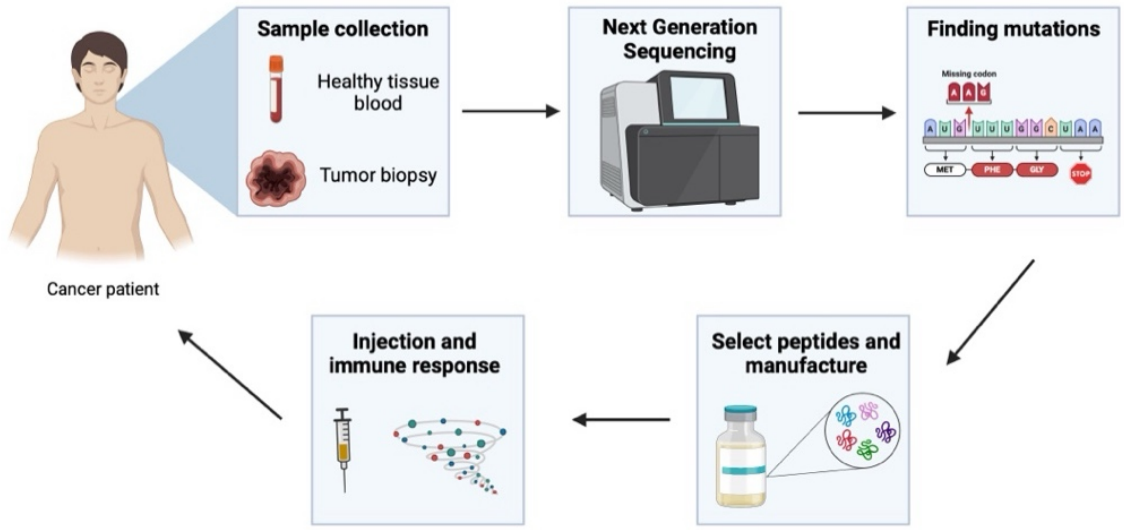

Figure 39. ***Scheme of the theoretical workflow of neoantigen-based vaccines****. The cancer patient undergoes sample collection, either of healthy tissue and the tumor. This biomaterial is subjected to next generation sequencing analysis in order to find the mutations present on the tumor tissue. Once the neoantigens are identified with the help of bioinformatics, the vaccine is manufactured. Vaccine is injected in the patient triggering an immune response.*

Peptide cancer vaccines are based on the administration of specific peptides derived from tumor antigens. These peptides are recognized by pattern recognition receptors (PRRs) and then internalized by antigen presenting cells (APCs), mainly dendritic cells (DCs). Once they are internalized, cells process and present them on their surface via major histocompatibility complex (MHC) molecules. CD8+ CTLs identify the presented peptides on MHC class I molecules, thereby initiating their activation and proliferation. Meanwhile, CD4+ helper T cells recognize peptides presented on MHC class II molecules and emit signaling cues to other immune cells. B cells can be stimulated by peptides presented by DCs, triggering the generation of antibodies tailored to the tumor antigens. Both, antibodies and activated CTLs can directly attach to tumor cells, facilitating their eradication, while inducing a memory response for heightened immune defense (Figure 40). [102]

However, as it has been mentioned before, the use of proteins or peptides as therapeutic agents still confront several hurdles nowadays. In this need of improvement of the therapeutic approach of proteins and peptides is where nanotechnology has emerged, creating nanometric vehicles for these proteins that solve part of their disadvantages.

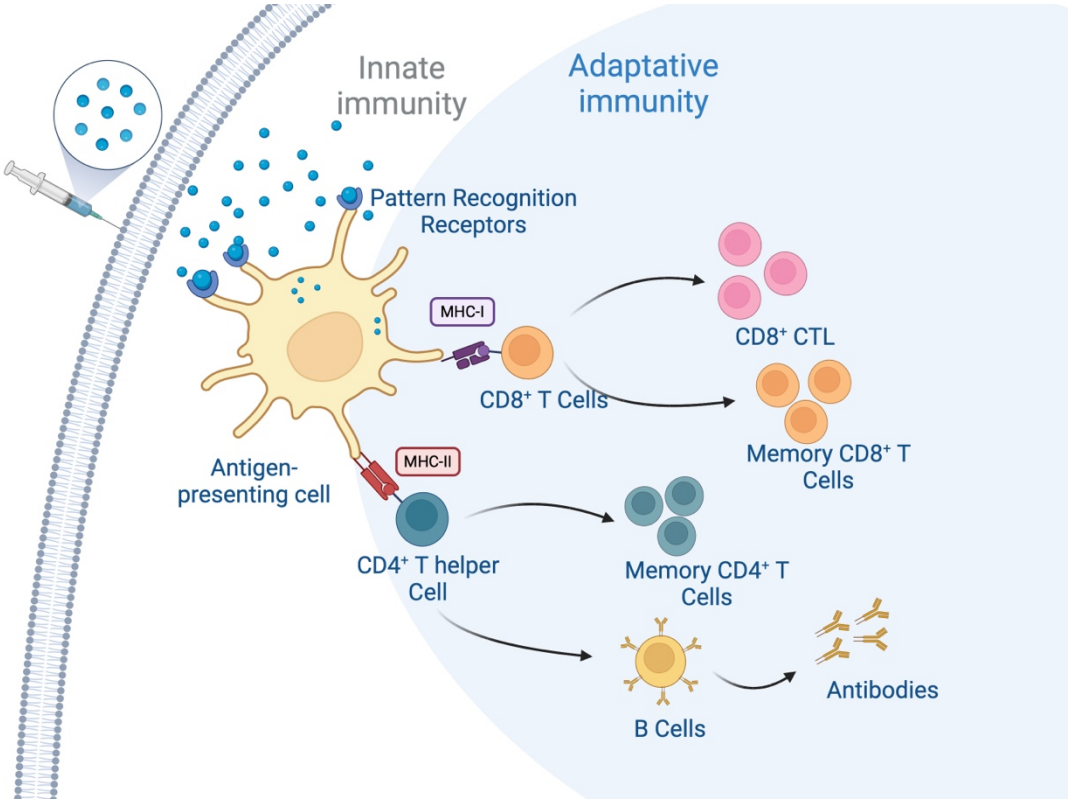

Figure 40. ***Schematization of the immune response provoked by cancer vaccination.***

1.2. Cancer vaccine antigens.

Tumor antigens can be categorized into two broad classes: tumor-associated antigens (TAAs), which are expressed by both the tumor and healthy tissues, and tumor specific antigens (TSAs) or neoantigens, which are exclusively expressed in the tumor lesion.[103]

The antigen selection is crucial for the speed, intensity, and duration of the immune response of the cancer vaccine. Even though neoantigens are theoretically preferred as a target for them, the vast majority of reported immunogenic antigen in pre-clinical stages are those shared with healthy cells (TAAs).[101] Prominent examples of targeted TAAs are human epidermal growth factor receptor 2 (HER2), which is a kinase belonging to the EGFR family, and it is overexpressed in approximately 30% of breast cancers, and prostatic acid phosphatase (PAP), which is expressed on prostate epithelia and increases proportionately with cancer progression. Nevertheless, clinical trials in this field suggest that a very strong immune response is needed to ensure the efficacy of the treatment which is still a great challenge.[104,105]

The main limitation associated to the use of TAAs is the risk of triggering autoimmunity against normal tissues and the low immunogenicity that they present. Additionally, T cells that recognize these antigens may be removed from the immune repertoire during the thymic selection and those

that elude this selection can remain inactive by the peripheral tolerance.[106,107] Besides that, the influence of the complex tumor microenvironment (TME), which is immunosuppressive by nature, is a limiting factor in the stimulation activity of cancer vaccines.[102,108]

The main research directions in this area relies on the increase of immunogenicity of the peptides included into the formulation, by using more immunogenic adjuvant platforms and combining the vaccine with immune checkpoint inhibitors.[100,101]

1.3. Adjuvants.

The term adjuvant comes from the Latin word 'adjuvare', meaning help. The use of adjuvant substances as a delivery and/or accompanying system/substance that increase the immune response of a vaccine candidate is a widely common strategy. Hence, their main aim is to enhance the immunogenicity of the formulation without compromising its tolerability or safety. However, they can also entail long-term immune responses, broaden protection, or provide cross-protection against related pathogens, enhancing immune responses in populations with low responsiveness and potentially reducing the required antigen quantity.[109]

Historically, adjuvants were aluminum salts, oil-in-water emulsions, and lipid aggregates in their majority.[110] One of the main focuses of adjuvant research is on pattern recognition receptors (PRRs) as they constitute the first line in the immune response. PRRs are responsible for the recognition of pathogen-associated molecular patterns (PAMPs) and damage-associated molecular patterns (DAMPs). A large number of different proteins constitute the distinct groups within the PRRs, among which we can remark the Toll-like receptors (TLRs).[111] Both preclinical and clinical evidence underscore the role of Toll-like receptor (TLR)-activating adjuvants in eliciting therapeutically relevant anticancer immune responses by mimicking microbial stimulation.[112] Consequently, it is noteworthy various Toll-like receptor (TLR) agonists have received approval for use in oncological indications (Picibanil, Monophosphoryl lipid A, Imiquimod...).[113]

1.3.1. Protein nanoparticles as delivery systems in cancer immunotherapy.

The use of nanoscale systems as adjuvants is gaining relevance in the cancer immunotherapy field since the approval of Abraxane for metastatic breast cancer in 2005 by the FDA.[114] Among others, protein-based nanoparticles can be highlighted because of their safety and ease of preparation. Besides that, they present considering benefits regarding functionalization and targeting capabilities.[115] Specifically, the use of antigen-derived nanoparticles is proved not only to

maintain their structural integrity, also slowing the rate of antigen release within DCs, thereby enhancing their immunogenicity.[116]

1.4. Toll-like receptors.

TLRs are part of the Type I integral membrane glycoprotein family, which are part of the PRRs. These proteins are distinguished by their extracellular domains comprising variable numbers of leucine-rich-repeat (LRR) motifs and a cytoplasmic Toll/interleukin 1 (IL-1) receptor (TIR) homology domain.[117,118]

While the exact number of genes may vary among different species, most mammalian species possess between 10 to 15 Toll-like receptors (TLRs). In the case of humans, our genome encodes 10 different TLRs (TLRs 1-10). TLRs are categorized into two subgroups based on their cellular localization and corresponding pathogen-associated molecular pattern ligands. One subgroup comprises TLR1, TLR2, TLR4, TLR5, TLR6 and TLR 10, which are situated on cell surfaces and primarily identify microbial membrane components like lipids, lipoproteins, and proteins. The other subgroup consists of TLR3, TLR7, TLR8, and TLR9, which are exclusively expressed within intracellular vesicles such as the endoplasmic reticulum (ER), endosomes, lysosomes, and endolysosomes, where they recognize microbial nucleic acids.[119,120]

In particular, TLR4 identifies bacterial lipopolysaccharide (LPS), a constituent of the cell wall found in gram-negative bacteria, while TLR2 detects gram-positive and fungal cell wall components like lipoteichoic acid and peptidoglycans Additionally, TLR2 forms heterodimers with TLR1 and TLR6, which recognize triacyl and diacyl lipopeptides, respectively. TLR5 recognizes flagellin. TLR10 also forms heterodimers with other TLRs although their ligands remain unclear. On the other hand, TLR3 recognizes double-stranded RNA (dsRNA), while TLR7 and TLR8 detect viral single-stranded RNA (ssRNA), and TLR9 not only detects viral but also bacterial and protozoan DNA (Figure 41).[121]

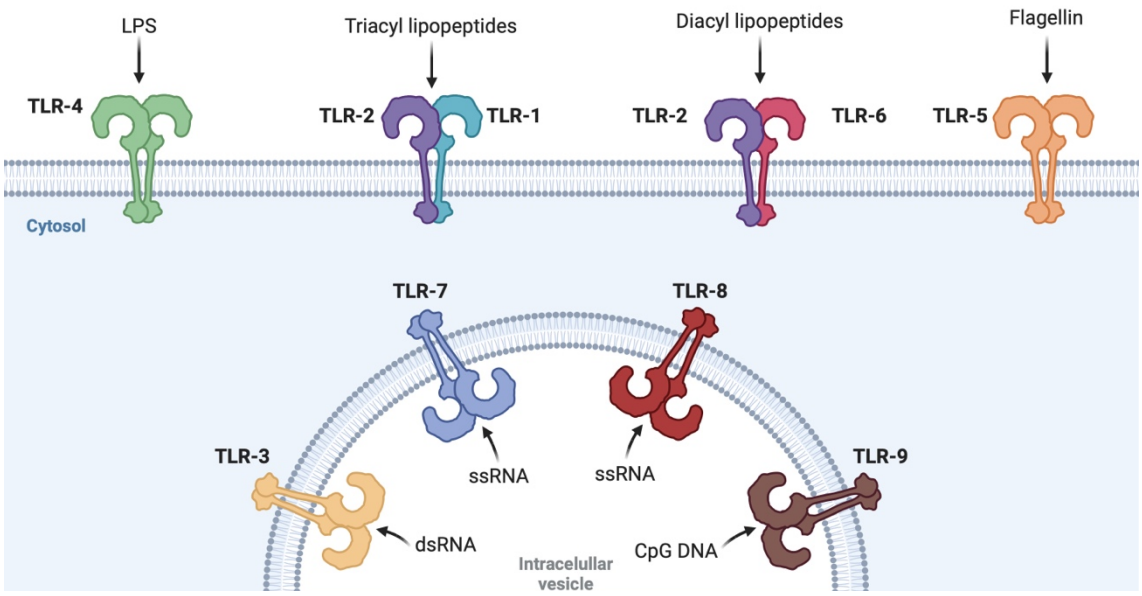

Figure 41. ***Schematic representation of the different TLR localizations and ligands.***

TLRs are expressed on all innate immune cells and a vast majority of non-hematopoietic cells, including macrophages, neutrophils, dendritic cells (DCs), natural killer (NK) cells, and epithelial cells.[118,122]

The whole range of TLR functions is still a matter of study. However, it is well known that, in innate immune cells, the TLR activation entails a pro-inflammatory response by the release of certain cytokines such as tumor-necrosis factor (TNF), interleukin-1β (Il-1β) and interleukin-6 (IL-6) as a direct consequence.[123] In turn, this cytokine release triggers an indirect response, which are the up-regulation of DC maturation markers and the MHC-II in the cell surface.[124] Mature DCs exhibit enhanced antigen-presenting capability and relocate from peripheral tissues to draining lymph nodes. There, they guide the adaptive immune response by activating T lymphocytes. Consequently, DC maturation, provoked by TLR stimulation, serves as a crucial connection between innate and adaptive immunity.[125] The qualitative and quantitative composition of the cytokine pattern induced in response to TLR stimulation varies depending on the receptors activated, the ligands recognized, and the types of cells that are stimulated.[126]

Even though TLR are promising targets in the field of immuno-oncology, they can act as a double-edged sword because it has been demonstrated that chronic inflammation can be directly linked to tumor progression. Inflammatory cells release growth and survival factors, proangiogenic factors, extracellular matrix-modifying enzymes, and reactive oxygen species (ROS), which can contribute to increased mutagenesis, growth, and invasion of cancer cells.[127]

1.5. Cytokines.

Cytokines are low molecular weight secreted or membrane-bound proteins, functioning as critical mediators for intercellular signaling to maintain the immune system's homeostasis. Their production is induced by cells of both innate and adaptive immunity in reaction to microbes and tumor antigens.[128] The variation in the cytokine levels in different biological fluid such us serum, blood, saliva or sweat can serve as a potential markers in diagnosis, staging, and prognosis of various diseases. In consequence, cytokine levels are acknowledged as crucial indicators for assessing clinical disorders. Precise quantification of cytokines levels provides valuable insights in clinical settings to monitor the patient immune status and to tailor therapies for various diseases, including asthma, depression, or cancer.[129]

Based on different criteria, cytokines can be categorized in different ways. Based on their type, cytokines can be categorized into several groups, including tumor necrosis factors (TNFs), interleukins (ILs), lymphokines, interferons (IFNs), colony-stimulating factors (CSFs), and transforming growth factors (TGFs). However, depending on their function they can be classified in pro-inflammatory and anti-inflammatory cytokines. Pro-inflammatory cytokines, such as IL-1β, IL-6, IL-8, IL-12, TNF-α, and interferons, among others, promote inflammatory responses and typically activate immunocompetent cells. Whereas anti-inflammatory cytokines like IL-4, IL-6, IL-10, IL-11, IL-13, IL-1 receptor antagonist (IL-1RA), and TGF-β, act as mediators in the inhibition of inflammation and suppress immune cells. [129] Besides that, there are dual function cytokines, such us IL-6, that through different mechanisms can act either as pro-inflammatory or anti-inflammatory cytokine.[130]

Nevertheless, it is well-known that an intense pro-inflammatory response can lead to chronic inflammation, disrupting the biological homeostasis and leading to different health problems such as cancer, gastrointestinal diseases, and aging.[131]

In the field of cancer, several cytokines have been reported with anti-proliferative or pro-apoptotic activities, limiting tumor cell growth and to indirectly induce the stimulation of the cytotoxic immune activity of immune cells.[132] In 1957, the discovery of IFN-α and its potential anti-tumor activity encouraged the use of cytokines in preclinical and clinical investigation. Thus, in 1986, IFN-α was the first cytokine approved for the treatment of cancer in humans, specifically for hairy cell leukemia (HCL). Apart from IFN-α, only high dose IL-2 was approved, in 1922, for the treatment of advanced renal cell carcinoma (RCC).[132,133] However, the modest efficacy of the use of cytokines as monotherapy has caused them to fall behind, giving way to new therapies.

1.6. OVA neoantigen.

Ovalbumin (OVA) is a harmless chicken protein that is commonly used as a tumor specific antigen or neoantigen model when expressed in the B16 melanoma cell line.[134] Different epitopes of OVA and different ways of presenting the antigen have widely described, and the most common outcome is that OVA neoantigen presents high therapeutic value for further clinical studies.[135–137]

2. Rationale.

Considering the current stage landscape in the field of cancer immunotherapy and the need of an optimal presentation of therapeutics, the aim of the project is to develop a nanoparticle-based vaccine for the B16-OVA pseudo-metastasis model in collaboration with Dr. Sandra Diebold. To this approach, we took advantage of the IC-Tagging system properties. We used the IC-Tagging system to produce protein-based nanoparticles and microparticles that are efficiently loaded with the OVA neoantigen. These preparations are thought to serve as a novel model for cancer vaccination.

2.1. Precedents.

In previous stages of the project, OVA-loaded nanospheres were produced in our laboratory using the bacterial expression system. The immunogenicity of this NS was evaluated, and results indicated that NS induced high levels of IL-6, IL-12-p40 and TNF-α. Besides that, in vivo experiments in mice demonstrated that NS induced antigen-specific CTL responses and an effective anti-tumor immune response in an OVA pseudo-metastasis model.

However, a subsequent Limulus Amebocyte Lysate (LAL) analysis detected the presence of LPS in the antigen-loaded preparations. LPS is a major constituent of the outer membrane of Gram-negative bacteria and elicits a potent innate immune response through the TLR4. Thus, although performed in the presence of Polymyxin B, the previously obtained data are not conclusive enough because of the possible effect of LPS in the immunostimulatory activity of the preparations.

2.2. New approaches: Endotoxin-free expression system and baculovirus expression system.

To overcome this problem, we proposed two different alternatives to produce endotoxin-free preparations using the IC-Tagging methodology.

On the one hand, we proposed to use the bacterial expression system. In this case, OVA-loaded NS were produced using ClearColi® strain. ClearColi are a genetically modified *E.coli* strain that disables the offending endotoxin signal while still retaining competency and protein expression capability. With this approach we were able to produce functionally clean nanospheres of our desired recombinant proteins without eliciting an endotoxin-produced immune response.

On the other hand, we took advantage of the baculovirus expression system in Sf9 insect cells. Using this method, we could generate OVA-loaded microspheres, avoiding the presence of bacterial endotoxin.

3. Nano/microspheres production and characterization.

To produce the OVA-loaded NS, ClearColi competent bacteria were transformed with dual-expression plasmids encoding muNS-Mi and the IC-tagged version of OVA. In this way, NS loaded with OVA were generated and purified easily using simple mechanical methods (Figure 42 A). All manipulations were performed using endotoxin-free reagents and labware in strict sterile conditions. To produce the OVA-loaded MS, we generated recombinant baculovirus of OVA-IC and muNS-Mi. The co-infection of insect cells with both of them produces OVA-loaded MS that can also be purified using simple mechanical methods (Figure 42 B). Both NS and MS were subjected to extensive analysis of size, composition, immunogenic profile, and their pattern of action.

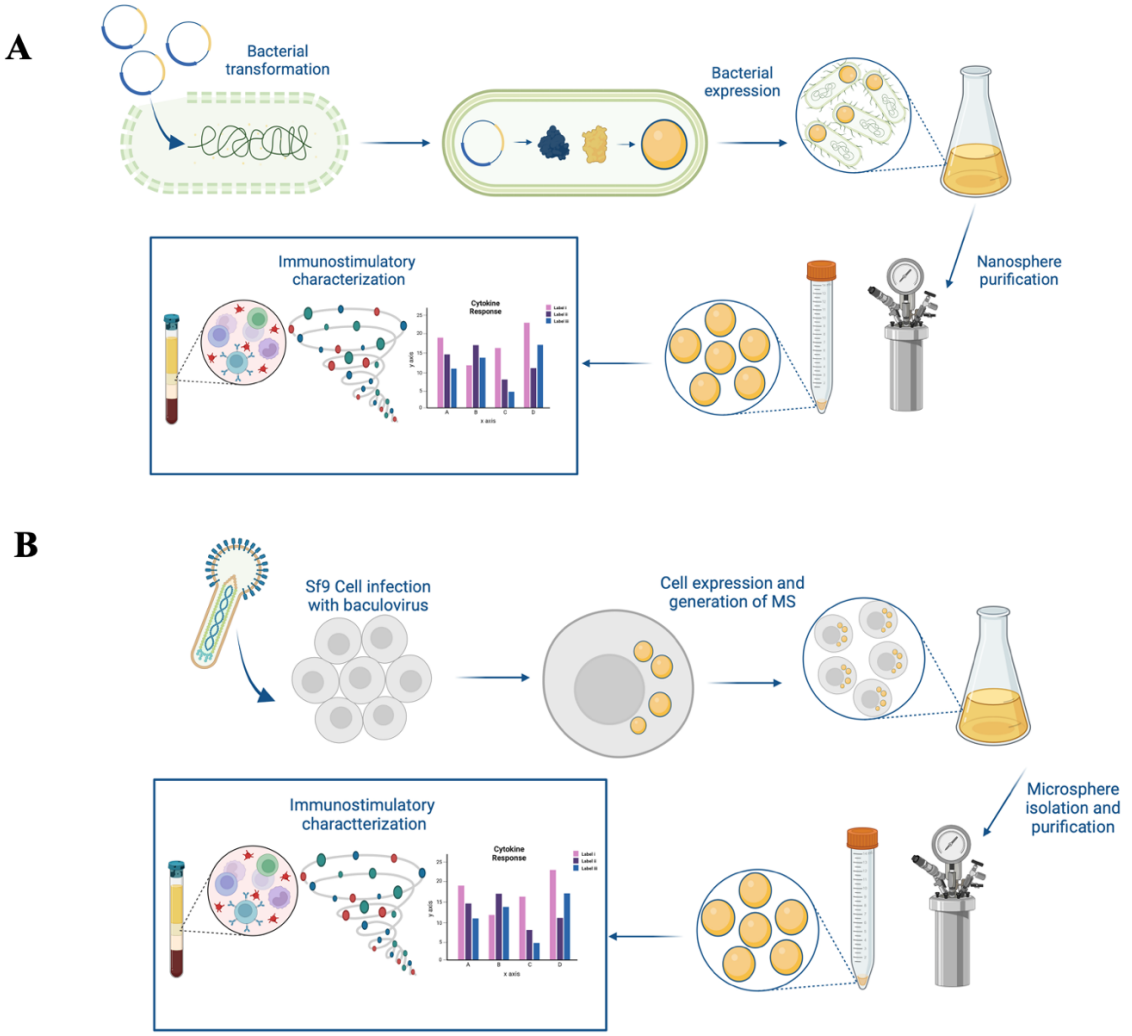

Figure 42. ***Schematic representation of the different OVA-loaded nano/microspheres. A. Production of OVA-loaded NS using bacterial expression system.*** *ClearColi bacteria are transformed with a dual plasmid encoding muNS and OVA-IC. These bacteria produce efficiently OVA-loaded NS that are purified using simple mechanical methods using French press homogenization and centrifugation. This preparation is used for further immunostimulatory testing.* ***A. Production of OVA-loaded MS using baculovirus expression system.*** *Sf9 cells are co-infected with baculovirus expressing OVA-IC and muNS-Mi respectively. Cells produce OVA-loaded MS. Microspheres are easily isolated and purified by sonication and centrifugation for further immunostimulatory testing.*

To assess the correct production and purification, the purified OVA NS and MS were subjected to SDS-PAGE. The Coomassie-staining analysis shows in both cases (Figure 43) two prominent bands at the molecular weights corresponding to OVA-IC and muNS-Mi respectively, assessing the correct expression and co-purification of both proteins.

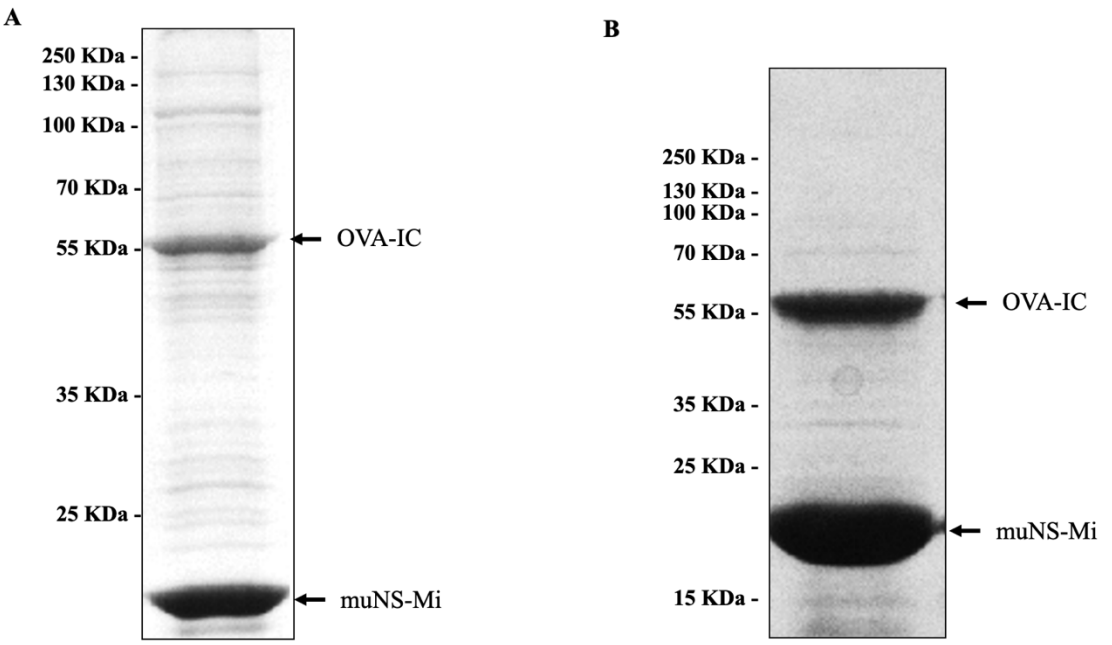

Figure 43. ***Coomassie-stained SDS-PAGE of the purified OVA-loaded NS (A) and MS (B).***

Moreover, the proper dispersion of OVA-loaded particles was checked out using dynamic light scattering (Figure 44). In both cases, the particle size corresponds to what we are expecting. In the case of OVA NS, the mean diameter of the particles is 338 nm. Whereas for OVA MS we obtained a particle size ranging from 1 µM to 3 µM. Finally, their dispersion and appearance were also checked by brightfield optical microscopy (not shown).

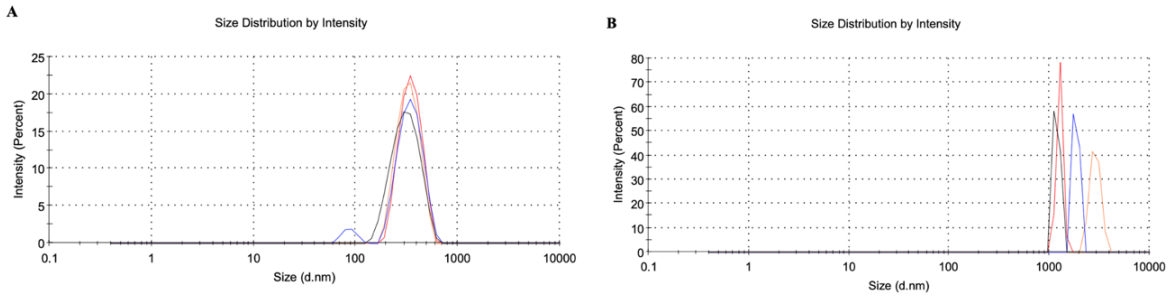

Figure 44. ***Size distribution of OVA NS (A) and OVA MS (B) obtained by DLS measurements.***

4. Endotoxin level test.

Even when the baculovirus-produced MS are supposed to be free of endotoxin, prior to starting the analysis of the cytokine activation profile, they were tested using the LAL test to determine the possible endotoxin or lipopolysaccharide contamination levels on them. In this test, endotoxin or LPS provoke a cascade of reactions that end up with the formation of gel clot, that proves its presence in the tested preparations (Figure 45).

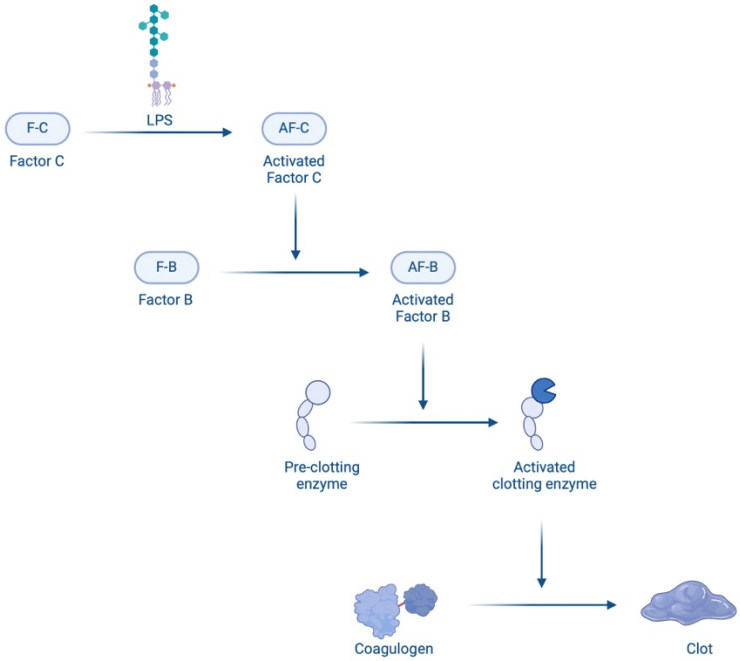

Figure 45. ***Basis of the Limulus amebocyte assay.*** *Upon exposure to endotoxins, factor C is cleaved and thus activated. The activated factor C cleaves and activates factor B, which cleaves and activates the coagulase enzyme. Finally, this active clotting enzyme cleaves another protein called coagulogen. A large number of cleaved coagulogen molecules combine to form a clot. This reaction is very efficient, so the clot forms in only 90 seconds.*

Results obtained in this test confirms that the baculovirus-derived OVA MS contain < 5 IU/ml of endotoxin. With this result we can affirm that the preparation is free of LPS and therefore we can proceed to study its immunostimulatory profile.

5. Cytokine release pattern for OVA-loaded NS.

5.1. Monocyte activation test.

To determine the ability of both OVA-loaded spheres to induce cytokine release, we decided to use the monocyte activation test (MAT) using peripheral blood mononuclear cells (PBMCs). The MAT assay is widely used to quantify pro-inflammatory and pyrogenic contaminants of medicines and vaccines because the use of human blood enables to replicate the early stages of the human immune system. The test is in accordance with the current European Pharmacopoeia (EP) Method C (EP chapter 2.6.30).

The isolation of PBMCs from whole blood samples was performed by centrifugation in the presence of a separation medium. Centrifuged samples were composed of a first upper layer of plasma, being the 55% of the whole sample. In the lower part was the erythrocyte layer, constituting the 45 % of the whole sample, and just in the middle of both layers, there was a tiny buffy coat, that corresponded to less that the 1% of the whole blood sample. In this layer is where

the PBMCs are found. The vast majority of them are lymphocytes and monocytes. Both cell types play a crucial role in the cytokine release, that is why their use is very extended in immunostimulatory assays.

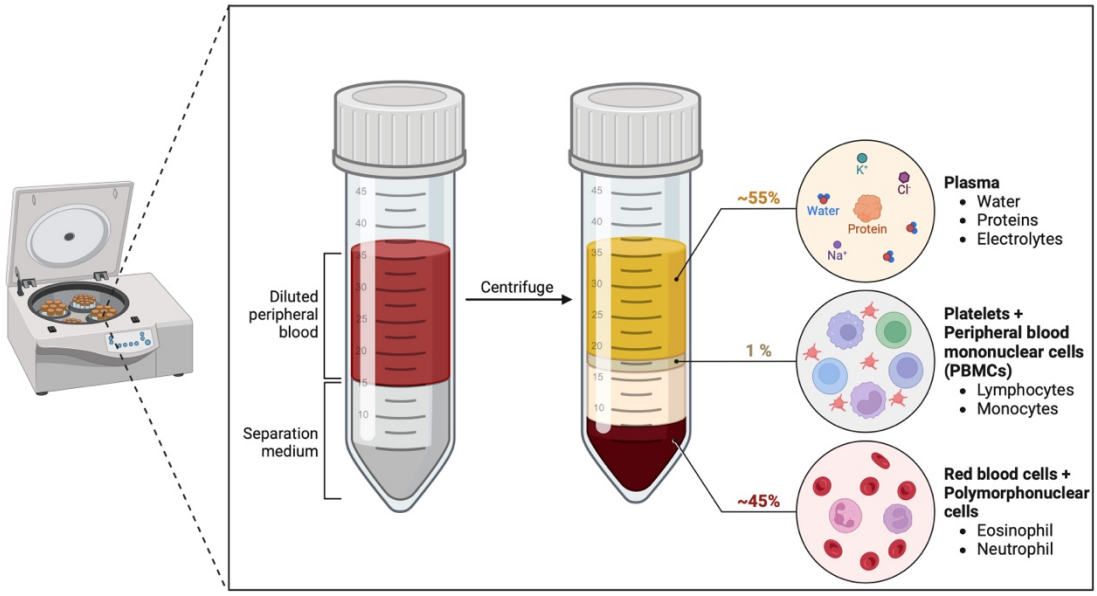

Figure 46. ***PBMCs isolation by centrifugation. Schematical display of cell types across the centrifuged blood sample.***

The PBMCs samples used at the MHRA were previously isolated, cryopreserved and determined of fitness for purpose from apheresis cones provided by the Oxford Blood Transfusion Centre.

The MAT test relies on the incubation of PBMCs with selected stimuli. During the incubation, the TLR receptor of PBMCs detects the presence of pyrogenic/pro-inflammatory substances that enhance the human immune response, activating cytokine release. In a first experiment, named as MAT I, we incubated PBMCs with OVA-loaded NS at different concentrations and different TLR agonists, that were included as further reference points: Pam3CSK4 and LTA (TLR2), polyI:C (TLR3), MPLA4 (TLR4), flagellin (TLR5), R848 (TLR7) and CpG ODN 2006 (TLR9). Besides that, endotoxin standard either with or without polymyxin B, and medium in the absence of cells were also included as controls. This MAT I was performed on PBMCs from 4 different donors and all the samples were measured in triplicates. The selected concentrations were chosen considering results obtained for previous experiments that are not included in this manuscript. After overnight incubation, supernatants were harvested and frozen for subsequent analysis. This MAT supernatants were used to generate a broad cytokine release profile induced by OVA NS.

In a second experiment, named as MAT II, we incubated PBMCs with OVA-loaded NS at different concentrations and we used fewer reference points (See Table 2). This was because the supernatants were additionally used to perform Il-6 and IL-8 quantification by sandwich ELISA

as explained below. Besides that, an endotoxin standard either with or without polymyxin B, and medium in the absence of cells were also included as controls. In this case the MAT II was performed with cells from 2 different donors and all the samples were measured in triplicates. After overnight incubation, supernatants were harvested and frozen for subsequent analysis.

Stimuli	Concentrations MAT I	Concentrations MAT II
Pam3CSK4	200, 100, 50, 25, 12.5, 6.25, 3.125 ng/ml	200, 100, 50, 25, 12.5, 6.25 ng/ml
LTA	25, 12.5, 6.25, 3.125, 1.563, 0.781, 0.391, 0.195 µg/ml	5, 2.5, 1.125, 0.625, 0.313, 0.156 µg/ml
PolyI:C	30 µg/ml	-
MPLA4	300 ng/ml	-
Flagellin	300 ng/ml	-
R848	10µg/ml	-
CpG ODN 2006	10µg/ml	-
Endotoxin std*	30 EU/ml	30 EU/ml
OVA NS	40, 20, 10, 5, 2.5, 1.25, 0.625, 0,313 ng/ml	40, 20, 10, 5, 2.5, 1.25, 0.625, 0.313 µg/ml

Table 2. ***Overview of the concentrations tested for the different stimuli in the MAT I and MAT II.*** *(*) Endotoxin standard was measured +/- polymyxin B (150µg/ml)*

5.2. Multi-cytokine release quantification for OVA-loaded NS in PBMCs.

Next, a selection of the harvested supernatants derived from the MAT I were used to perform a multi-analyte immune assay. We used a LEGENDPLEX™ human inflammation panel. This panel allows the simultaneous quantification of 13 different human cytokines: including IL-1β, IFN-α2, IFN-γ, TNF-α, MCP-1, IL-6, IL-8, IL-10, IL-12p70, IL-17A, IL-18, IL-23, and IL-33. We chose this panel due to the broader dynamic range and the higher sensitive that it offers compared to conventional sandwich ELISA.

The selected stimuli for the multi-analyte assay are summarized below. The assay was performed using the supernatants obtained from MAT I from just three different donors.

Stimuli	Concentrations
Pam3CSK4	200, 100, 50, 25, 12.5 ng/ml
LTA	25, 12.5, 6.25, 3.125 µg/ml
PolyI:C	30 µg/ml
MPLA4	300 ng/ml
Flagellin	300 ng/ml
R848	10µg/ml
CpG ODN 2006	10µg/ml
Endotoxin std	30 EU/ml
OVA NS	40, 20, 10, 5 µg/ml

Table 3. ***Overview of the concentrations tested for the different stimuli in the multi-analyte assay.***

Results obtained in this assay are presented in Figure 47 and Figure 48. They revealed that, undoubtedly, there is no relevant presence of IFN-α, IFN- γ, IL-10, IL-12p70, IL-17A, IL-18 IL-23 and IL-33 in the supernatants of PBMCs incubated with OVA NS.

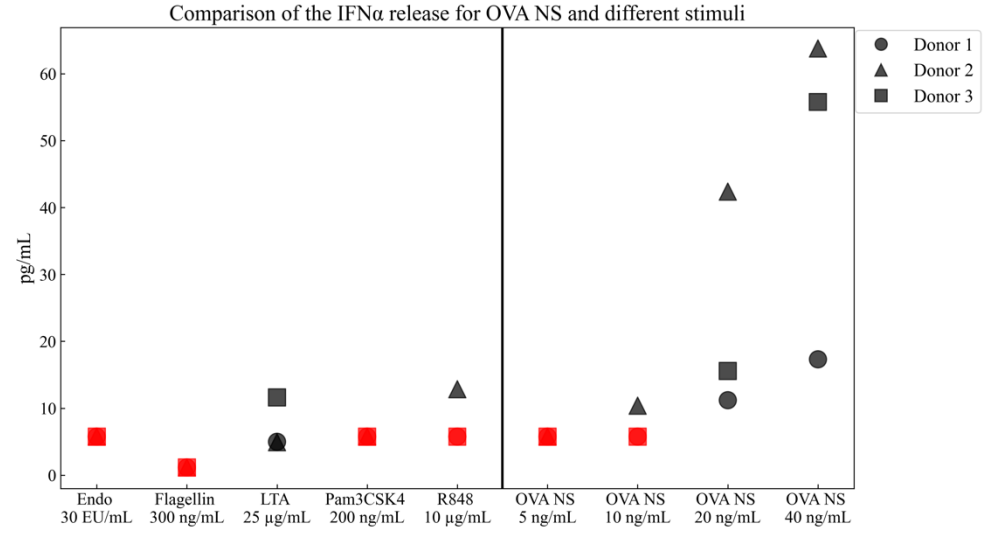

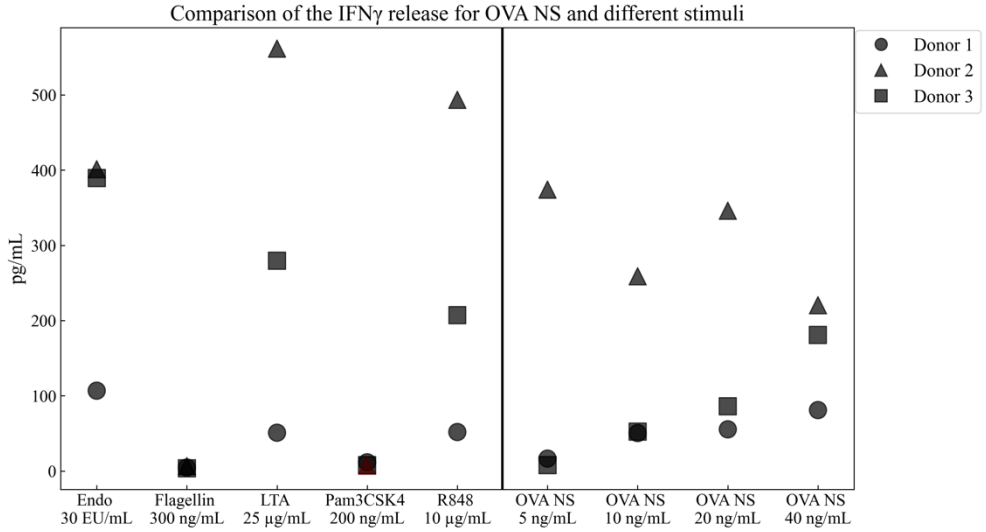

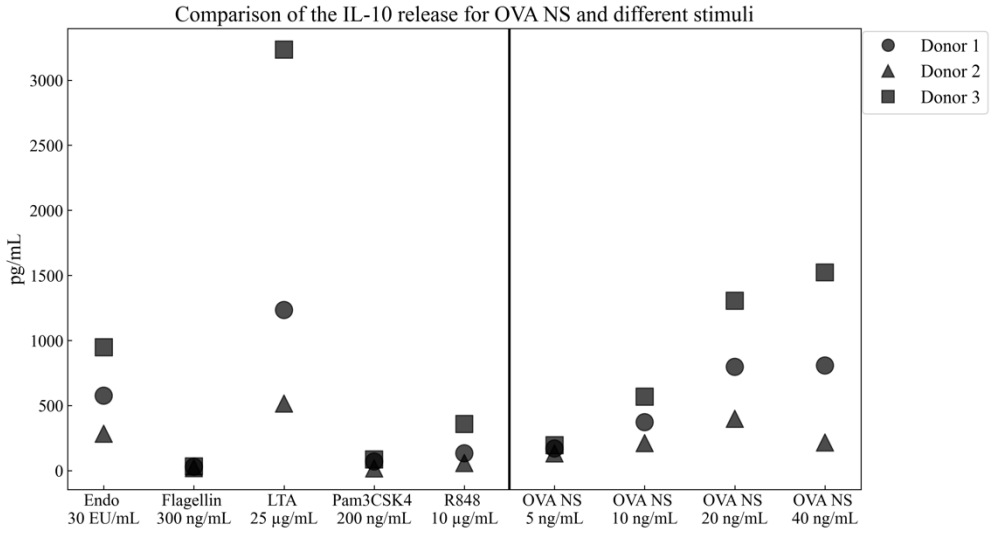

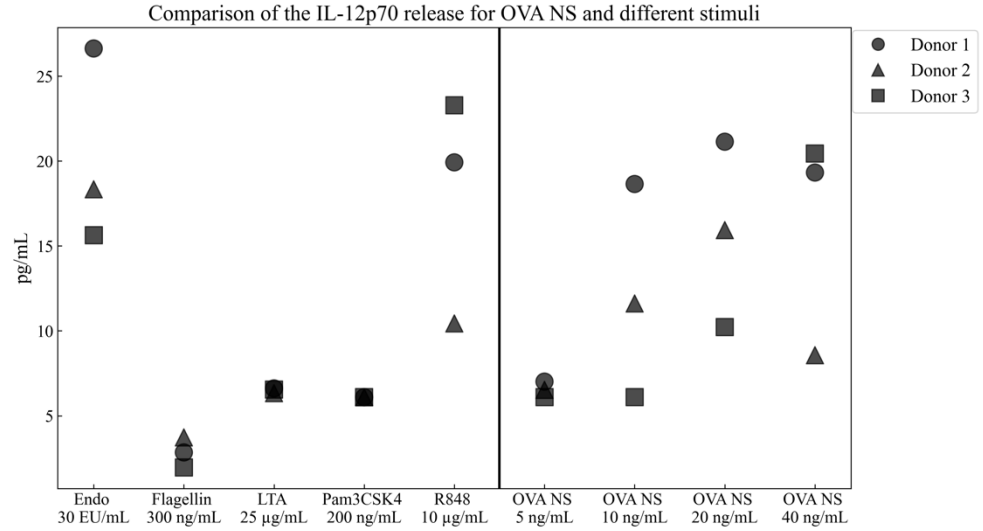

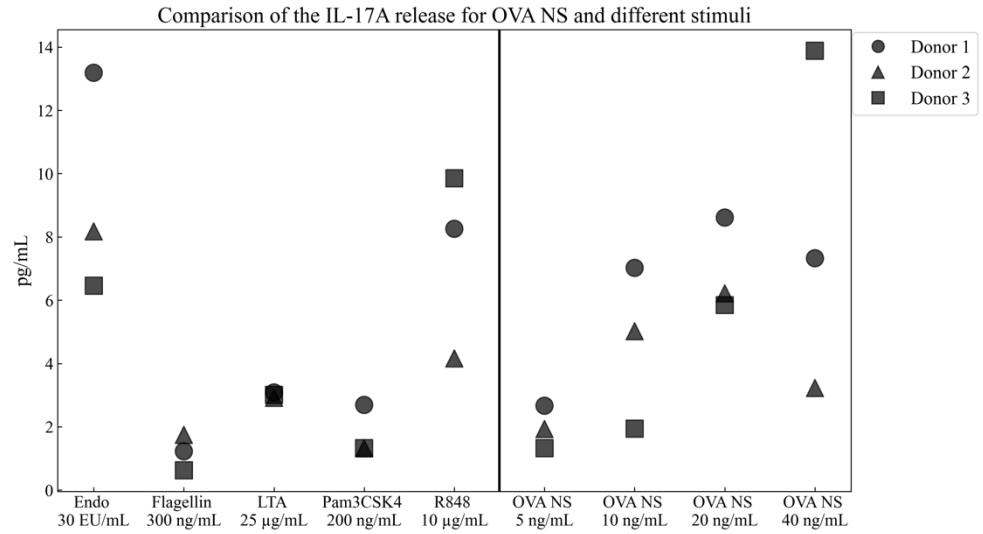

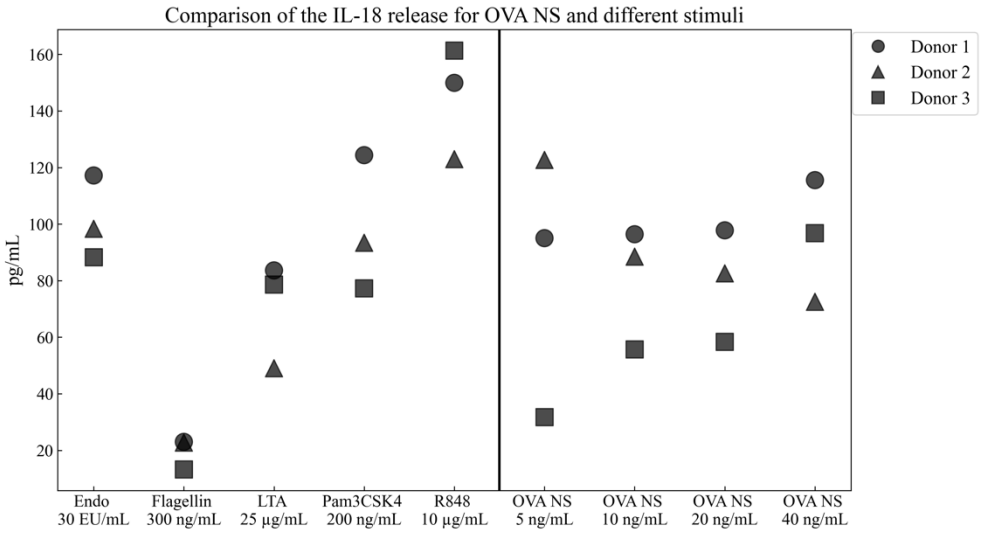

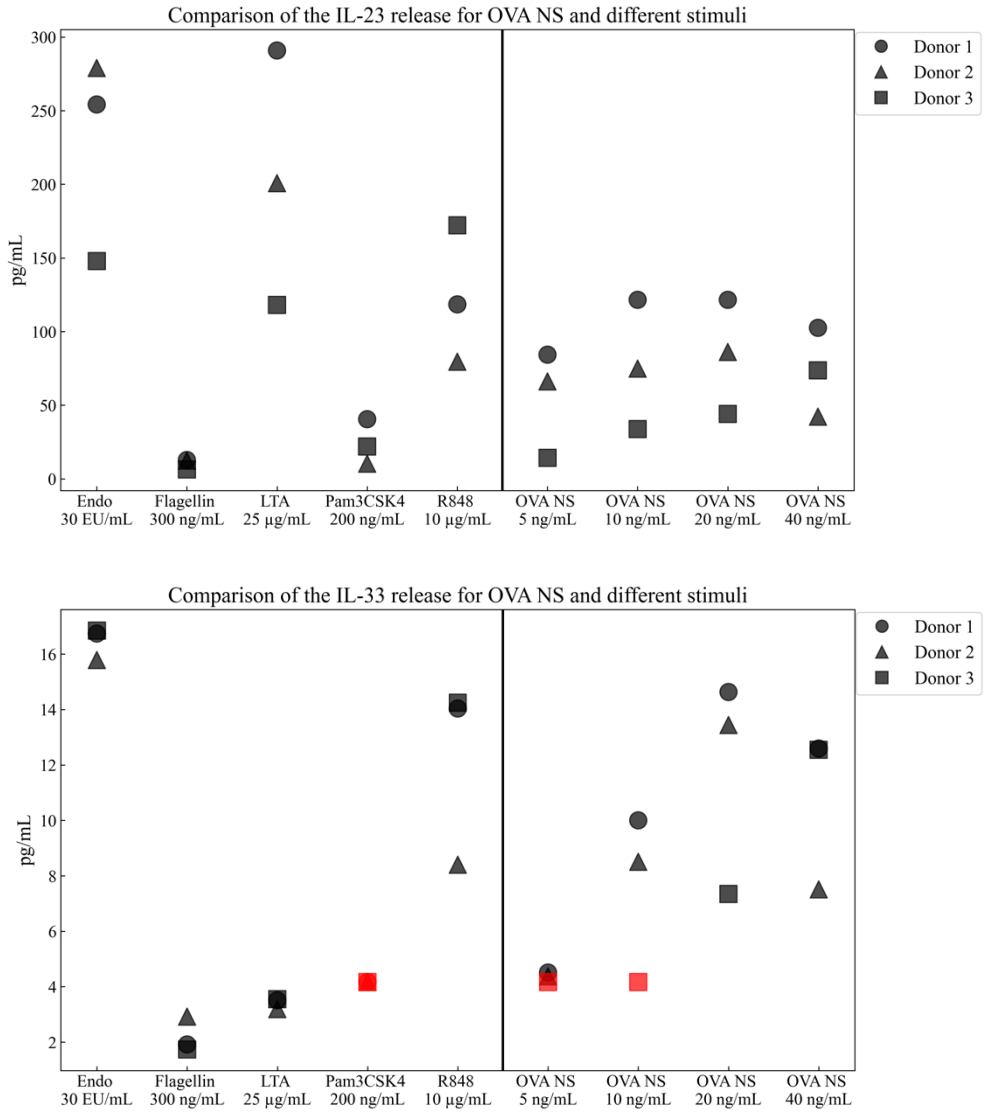

Figure 47. ***Results obtained for the cytokine release for those that do not present relevant levels of release in three different donors from MAT I.*** *Supernatants were measured at different dilutions. Data points out of range are shown in red.*

On the other hand, results obtained for IL-1β, MCP-1, IL-6, IL-8 and TNF-α showed a clear release pattern when PBMCs were incubated with OVA NS. In all the cases the difference in the cytokine release between donors was attributed to the donor's capacity of inducing the cytokine response.

In all the cases we could see how Donor 1 presented higher sensitivity to OVA NS. In the case of IL-1β and MCP-1 the cytokine release increased with the dose of OVA-NS, what indicates that further increase in the concentration of OVA NS may still induce higher responses. On the contrary, the release of TNF-α remains stable while increasing concentration. Moreover, for IL-6 and IL-8 data were above the upper detection limit of the assay even for the lower dose of OVA

NS. This diverse cytokine release showed that, as we expected, the OVA-loaded NS can provoke an immune response in human PBMCs that is translated to an induction of cytokine release.

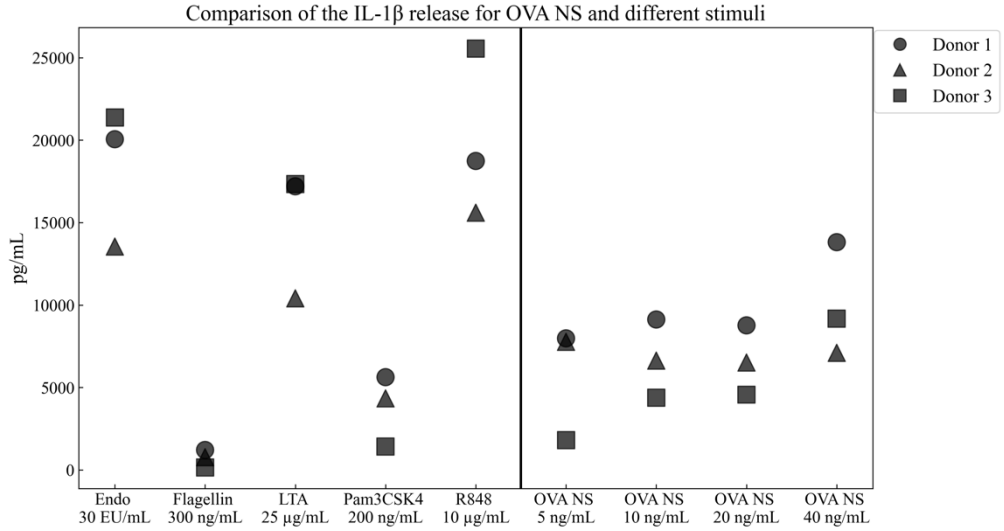

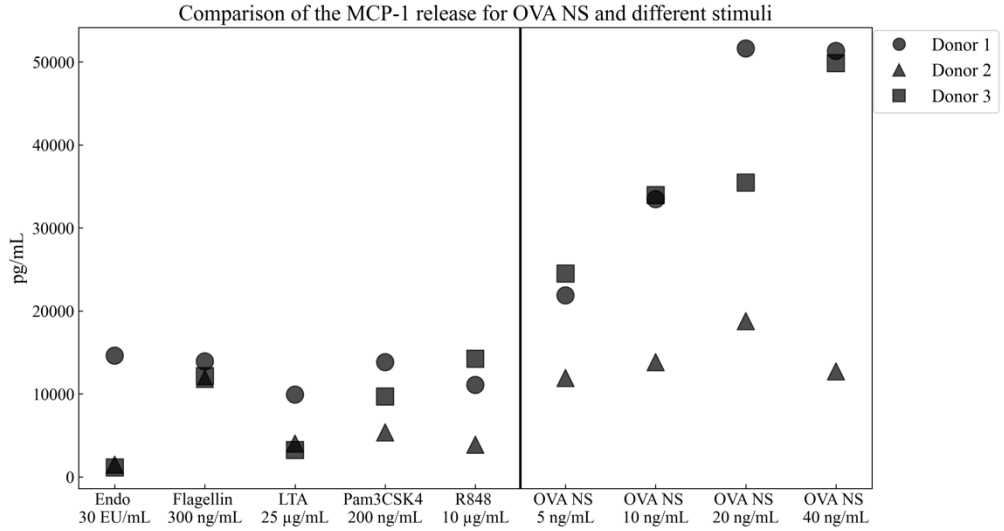

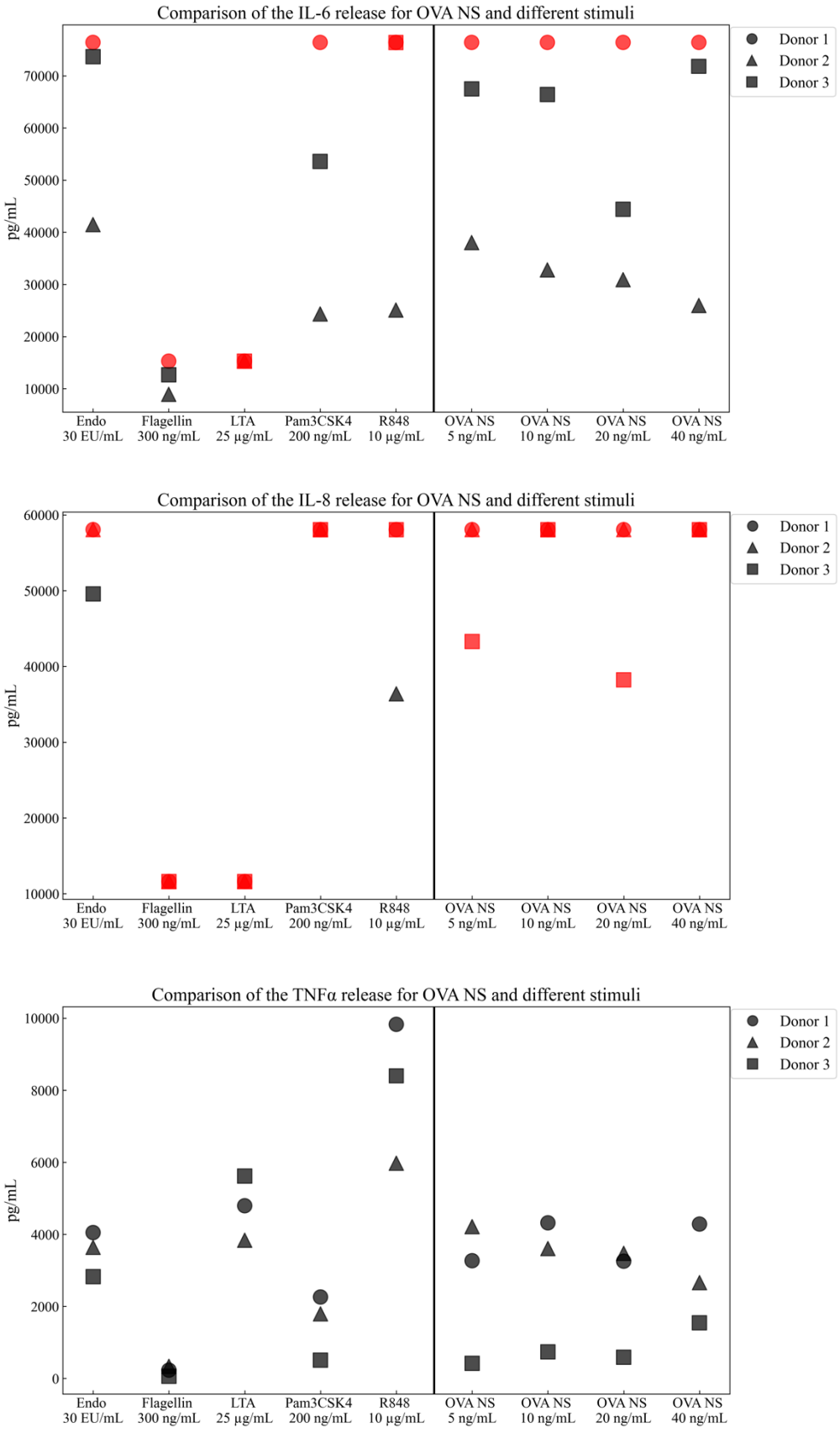

Figure 48. ***Results obtained for cytokine release for those that present relevant levels of release in three different donors from MAT I****. Supernatants were measured at different dilutions. Data points out of range are shown in red.*

5.3. Comparison of cytokine release for OVA-loaded NS in PBMCs and whole blood.

In order to test if the immune response pattern provoked by OVA NS in PBMCs could be compared to the one produced by humans, a multi-analyte assay was performed in which the detection of cytokine release for PBMCs and human blood was carried out in parallel. This assay was performed by Dr. Sandrine Vessillier and Deepa Rajagopal following the standardized protocol dictated by the Medicine and Healthcare products Regulatory Agency of the United Kingdom. To this approach, blood samples were extracted from 5 volunteer donors at MHRA and PBMCs were extracted from these blood samples. In parallel, PBMCs and blood samples were incubated with two reference TLR agonists and the OVA NS at different concentrations (Table 4). Supernatants were analyzed using a V-PLEX Proinflammatory Panel 1 Human Kit. This kit enables the quantification of 10 cytokines simultaneously: IL-1β, IFN-γ, TNF-α, IL-2, IL-4, IL-6, IL-8, IL-10, and IL-12p70.

Stimuli	Concentrations
Pam3CSK4	200 ng/ml
LTA	2.5 µg/ml
OVA NS	5, 2.5, 1.25 µg/ml

Table 4. ***Overview of the concentrations tested for the different stimuli in PBMCs and whole blood.***

In this assay, we determined that all cytokines were induced in response to OVA NS similar to the TLR2 control agonists, Pam3CSK4 and LTA (Figure 49). As expected, greater levels of induction in both assays were obtained for IL-6 and IL-8. Besides that, the cytokine induction pattern was similar between PBMCs and whole blood (WB), except for IL-6 and IL-8. IL-6 presented greater levels of induction in the WB assay, while IL-8 induction levels are higher for PBMCs.

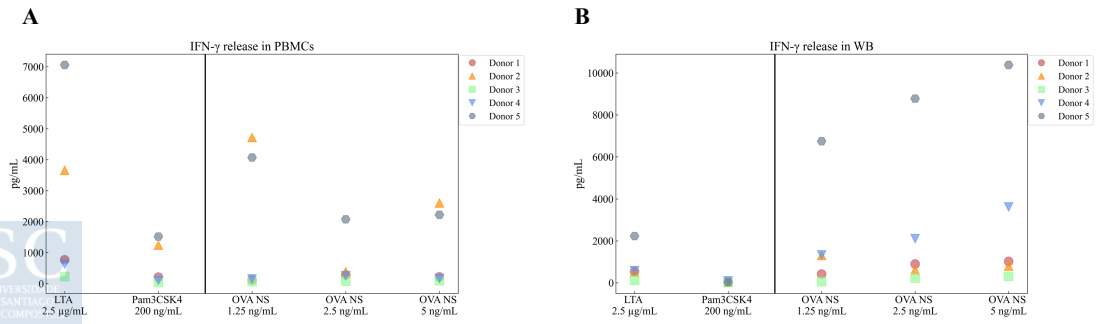

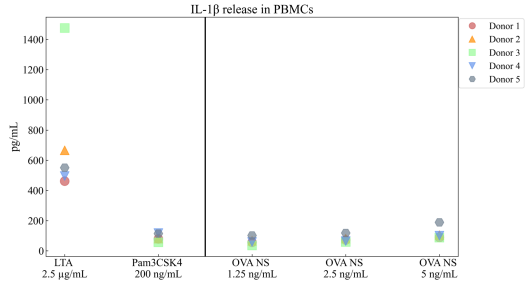

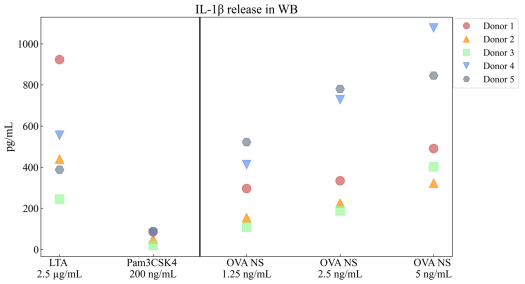

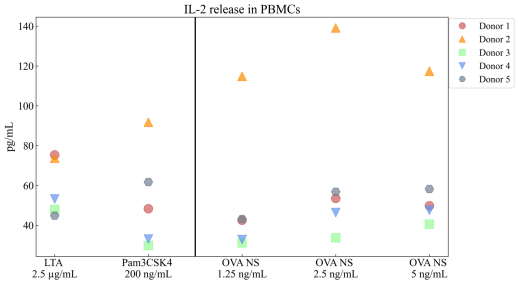

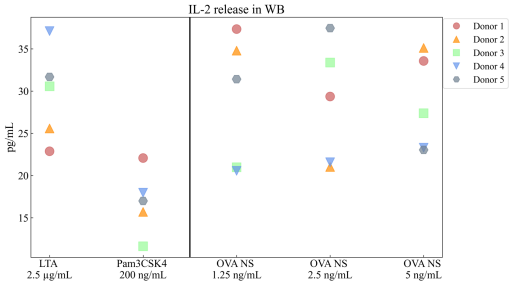

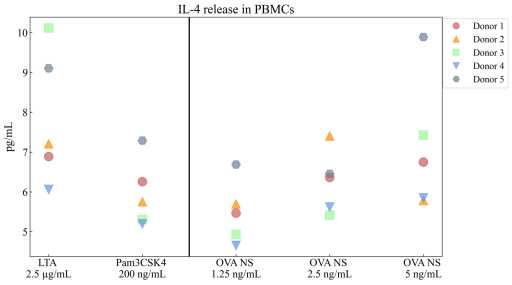

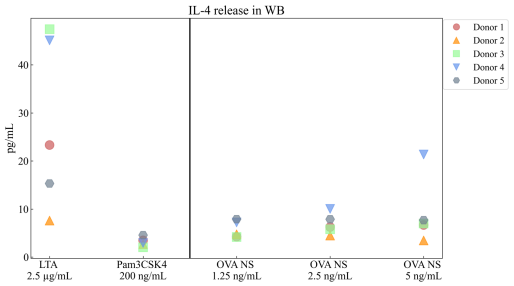

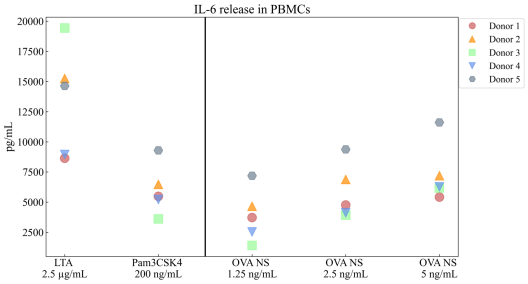

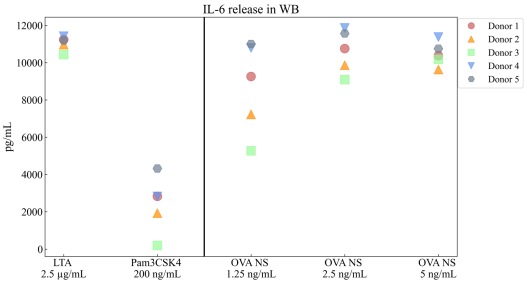

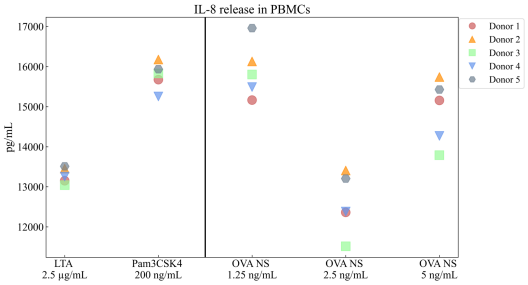

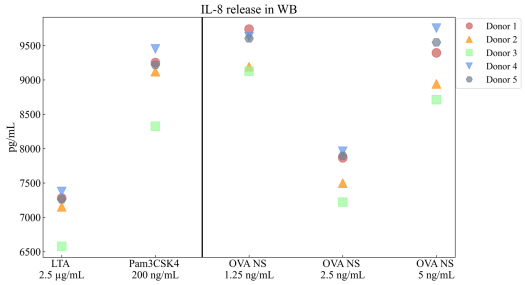

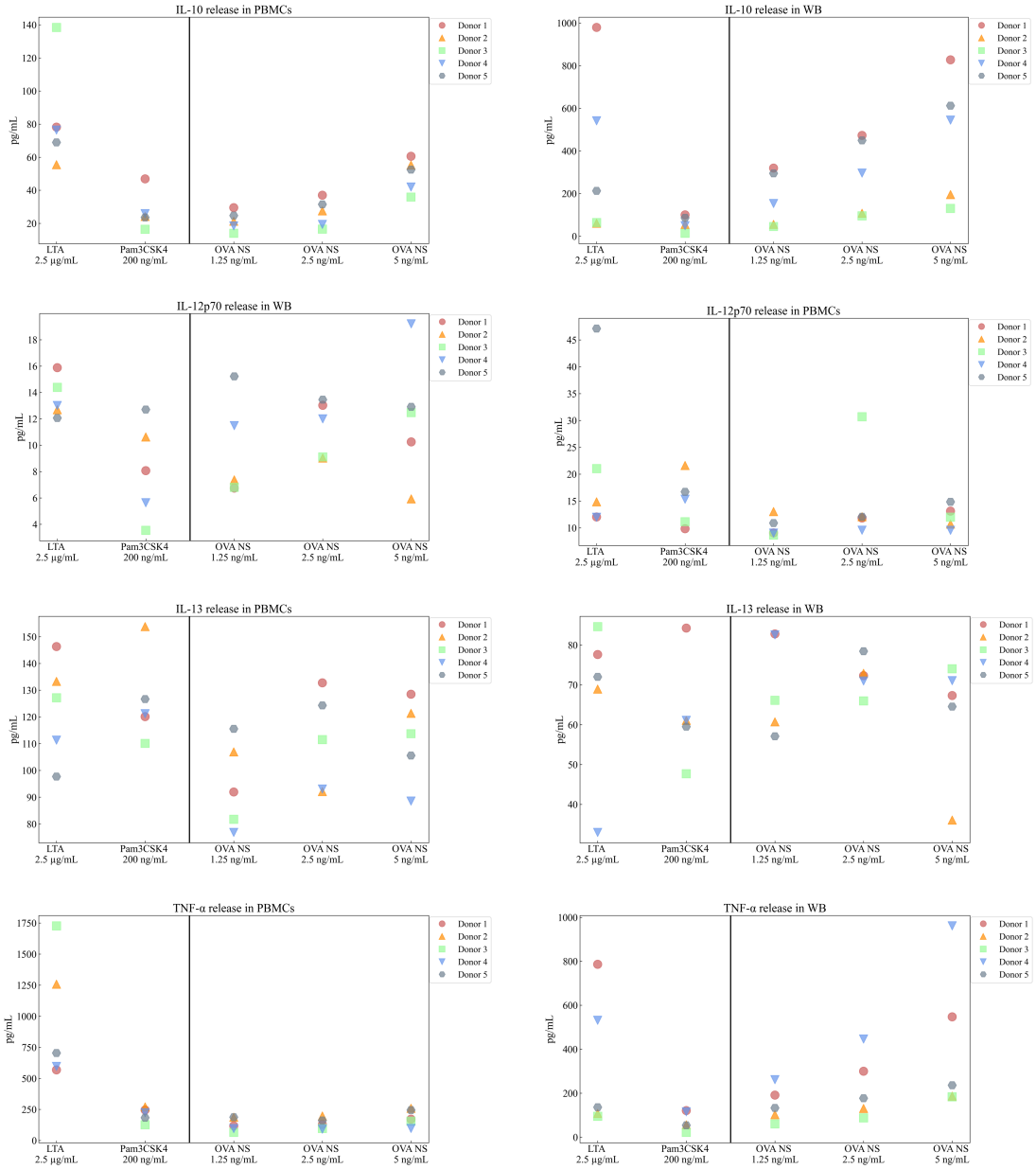

Figure 49. ***Cytokine release induced by OVA NS and TLR2 agonists in PBMCs (A) and in whole blood (B).***

5.4. IL-6 and IL-8 quantification for OVA NS.

As mentioned before, in the multi-analyte assay, it was not possible to properly quantify Il-6 and IL-8 release as data were above the detection limits. Thus, for this purpose we performed sandwich ELISA for both analytes using the supernatants from MAT II. The samples subjected to analysis are summarized in Table 5. Pam3CSK4 and LTA were used as reference points to compare the IL-6 and IL-8 release in PBMCs produced by OVA NS.

	hIL-6 ELISA	hIL-8 ELISA
Pam3CSK4	200, 100, 50, 25, 12.5 and 6.3 ng/ml	200, 100, 50 ng/ml
LTA	5, 2.5, 1.25, 0.625, 0.313, 0.156 µg/ml	5, 2.5, 1.125 µg/ml
Endotoxin std*	30 EU/ml	30 EU/ml
OVA NS	40, 20, 10, 5, 2.5, 1.25, 0.625, 0.313 µg/ml	40, 20, 10, 5, 2.5 µg/ml

Table 5. ***Overview of the stimuli and their concentration tested for the hIL-6 and hIL-8 for OVA NS.*** *(*) Endotoxin standard was measured +/- polymyxin B (150µg/ml)*

Results obtained are shown in Figure 50. We can observe that Donor 5 presents high sensitivity to the reference stimuli and the OVA NS. In the case of IL-6, higher release levels are shown between 2,5 µg/ml and 5 µg/ml of OVA NS, ranging from 20 ng/ml to 27 ng/ml. However, higher levels of IL-8 are obtained for concentrations of OVA NS between 10 µg/ml and 20 µg/ml, that go up to 280 ng/ml.

It is evidenced that the release of IL-8 induced by OVA NS is considerably higher than IL-6. Even though, in both cases, the higher cytokine release induced by the OVA NS was similar to those induced by the higher doses of Pam3CSK4 and LTA. As both cytokines are related with TLR2 and TLR4 pathways, further analysis is required to precisely elucidate which may be the receptors mediating in the immune response induced by OVA NS.

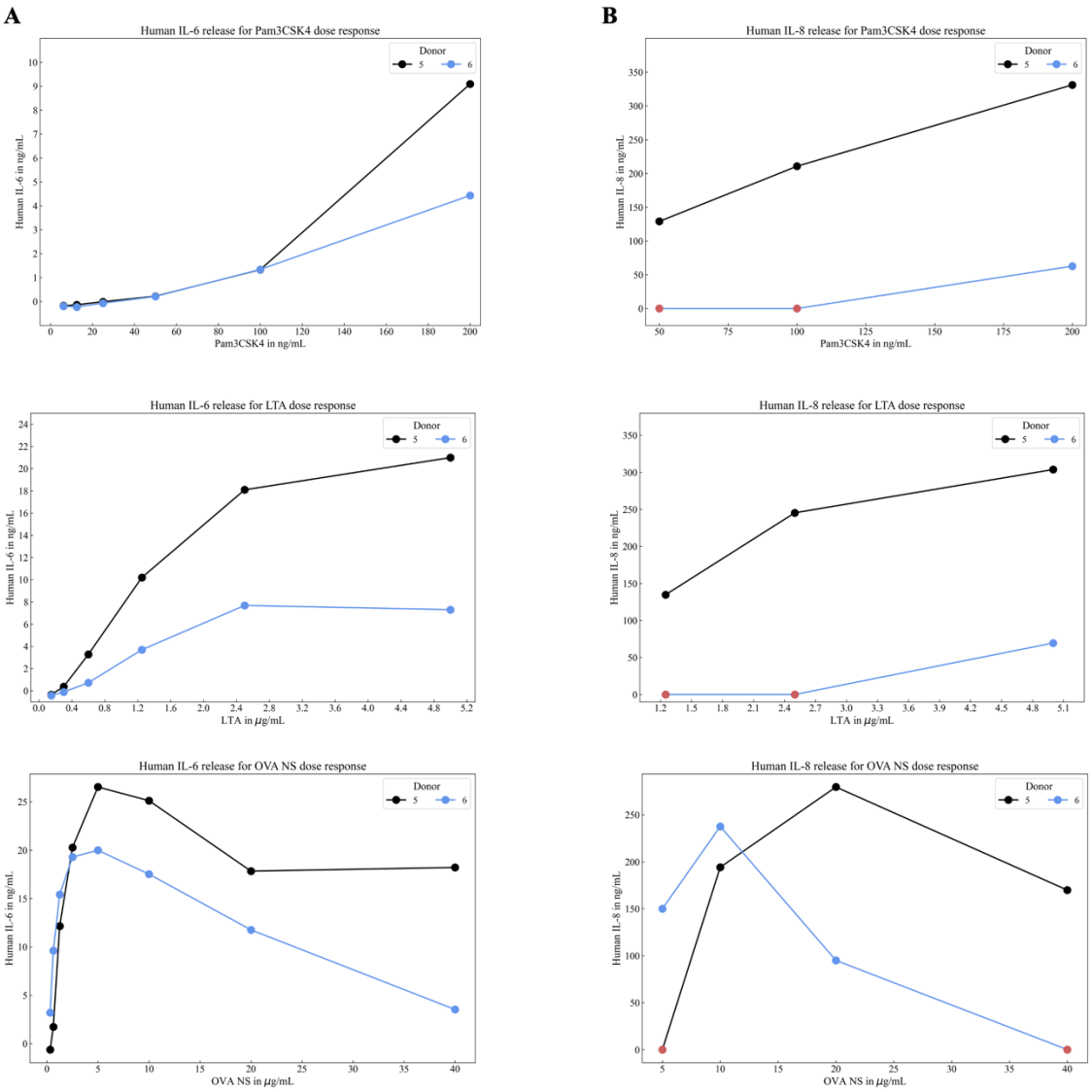

Figure 50. ***Cytokine release for hIL-6 (A) and h-IL-8 (B) induced by reference stimuli and OVA NS.*** *Results obtained using sandwich ELISA. Data points out of range are shown in red.*

6. TLR specific activation for the OVA-loaded NS.

After confirming the immunostimulatory activity of the OVA NS we wanted to gain a better understanding of the mechanism of action of the OVA NS preparations. Hence, we wanted to identify the pattern recognition receptor or receptors that mediate the immunostimulatory activity of NS preparations. To this approach we used different toll like receptors-related transgenic reporter human cell lines. Lines HEK-Blue™ were used: HEK-Blue hTLR2, HEK-Blue hTLR4, HEK-Blue hTLR5, HEK-Blue hTLR9 and HEK-Blue Null1. These cells express the soluble embryonic alkaline phosphatase (SEAP) protein, easily quantified spectrophotometrically using a commercial detection solution, after stimulation with a specific agonist. The HEK-Blue Null1 cell line is the parental cell line of the TLR cell line series and lacks any TLR expression construct.

Thus, cells were incubated with different doses of OVA NS (10, 5, 2.5, 1.25, 0.625, 0.316, 0.156, 0.078 ng/ml) overnight. After incubation, supernatants were harvested for analysis. Results from Figure 51 showed a poor stimulation of TLR4 cells (blue line), while the TLR2-containing cell line (red line) presented high levels of stimulation compared to all the other analyzed TLRs. Thus, the results indicate that TLR2 might be the only one involved in the immune response to the presence of OVA-NS and no TLR4 as we also hypothesized. To confirm these results, we used the cell line THP1-Dual KO-TLR4, that were generated from the THP1-Dual cell line, which is derived from the human THP-1 monocytes, through the stable knockout of the TLR4 gene. These TLR4 knockout cells presented a strong stimulation (Figure 51, grey line), confirming that TLR4 is not involved in the response to OVA NS.

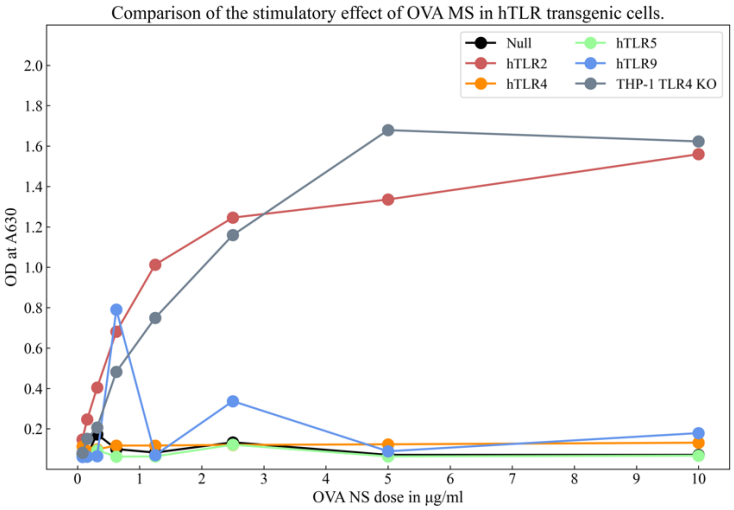

Figure 51. ***Comparison of the stimulatory effect induce by different doses of OVA NS in hTLR transgenic cells and TLR4 KO cells.***

To confirm the involvement of TLR2 in the obtained response, we used TL2-C29, a small-molecule inhibitor of TLR2. The addition of TL2-C29 (100µM) to HEK-Blue hTLR2 reporter cell line blocked almost all the stimulation from the OVA NS (Figure 52, compare the black and red lines), in keeping with the involvement of this receptor in the stimulation by the NS. However, we could also notice that there was still a remaining stimulatory activity when the inhibitor was present, suggesting that maybe TLR2 is not the only PRR entailing the immune response to OVA NS.

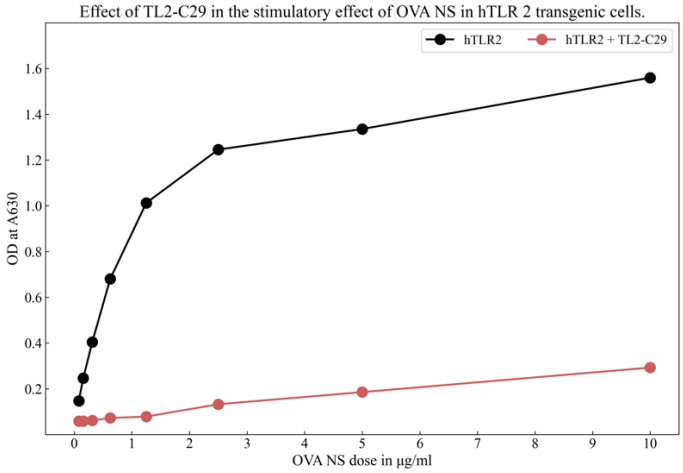

Figure 52. ***Effect of a TL2-C29 in the stimulatory activity of OVA NS at different doses in hTLR2 cells.***

7. IL-6 and IL-8 release for the OVA-loaded MS.

Taking into account the cytokine release pattern obtained for the OVA NS, we expected to observe a similar pattern for the OVA MS. For this purpose, we performed a new MAT assay (MAT III) for three different donors. We incubated PBMCs with the OVA-loaded MS at different concentrations Pam3CSK4 and LTA were used as reference points at different concentrations. Besides that, an endotoxin standard either with or without polymyxin B, and medium in the absence of cells were included as controls (Table 6). Supernatants were harvested and used to perform Il-6 and IL-8 quantification by sandwich ELISA.

Stimuli	Concentrations MAT III.
Pam3CSK4	200, 100, 50, 25, 12.5 and 6.3 ng/ml
LTA	5, 2.5, 1.25, 0.625, 0.313, 0.156 µg/ml
Endotoxin std*	30 EU/ml
OVA NS	20, 10, 5, 2.5, 1.25, 0.625, 0.313 µg/ml

Table 6. ***Overview of the stimuli and its concentration used for MAT and tested for the hIL-6 and hIL-8 for OVA MS.*** *(*) Endotoxin standard was measured +/- polymyxin B (150µg/ml)*

Results obtained in these assays are shown in Figure 53. As we can observe, the pattern of stimulation is different between donors. However, in both cases, the cytokine release obtained is

lower than those induced by the TLR 2 agonists. On top to that, the higher values of cytokine release are induced for the higher doses of OVA MS. This indicates that probably an increase in the dose will increase the cytokine release, although it requires further confirmation.

To conclude, levels of release of IL-6 are notably lower than those for IL-8, as it occurs for OVA NS. For IL-6, we obtain maximum values between 3.5 ng/ml and 1.5 ng/ml. While for IL-8 maximum values range between 42 ng/ml and 14 ng/ml.

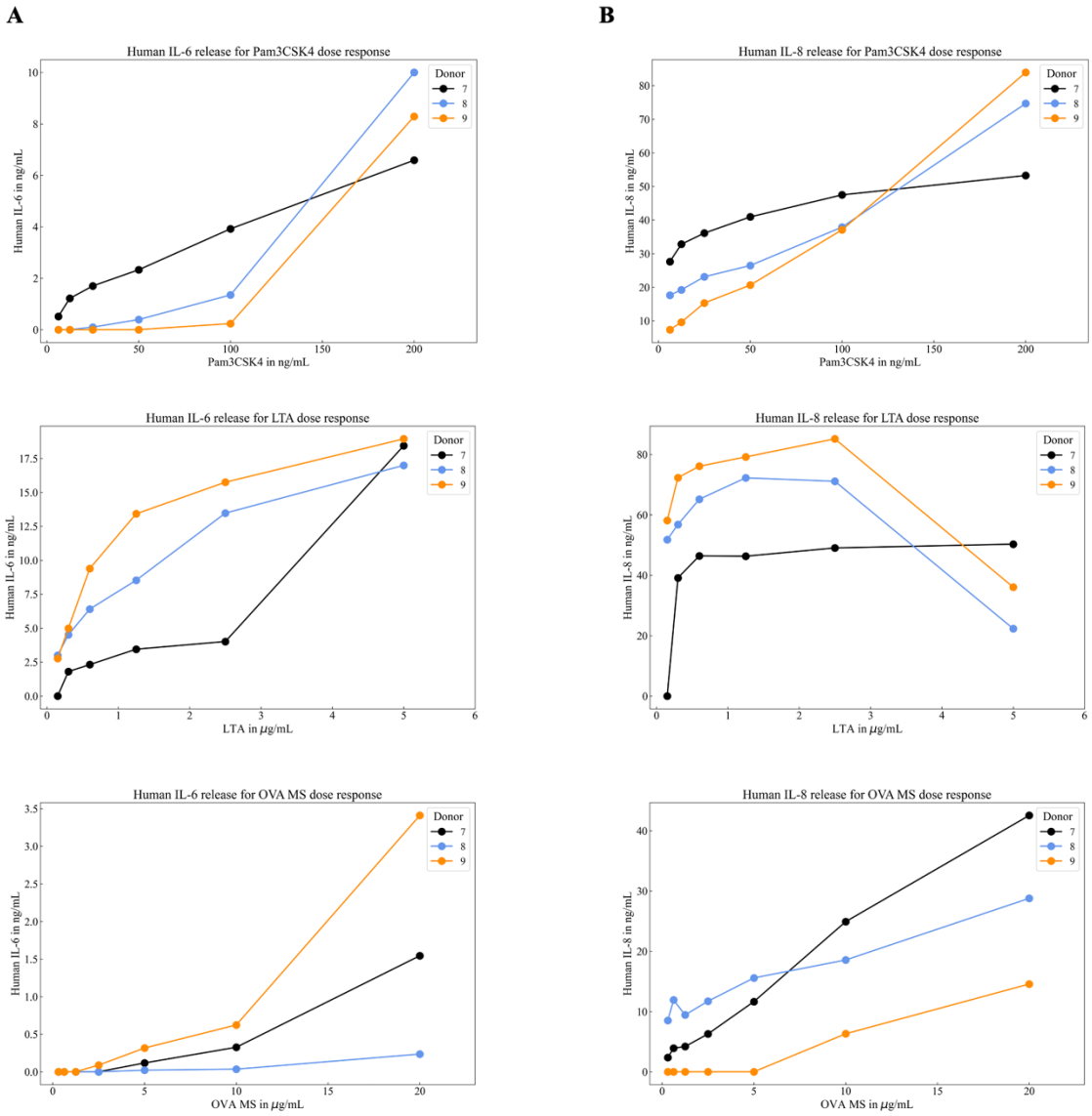

Figure 53. ***Cytokine release for hIL-6 (A) and h-IL-8 (B) induced by reference stimuli and OVA MS.*** *Results obtained using sandwich ELISA.*

8. TLR specific activation for the OVA-loaded MS.

Once we have assessed the IL-6 and IL-8 release of the OVA MS, we aim to elucidate if their mechanism of action follows the same pattern than the OVA NS. For this purpose, we used again

HEK-Blue hTLR2, HEK-Blue hTLR4, and HEK-Blue Null1 that were incubated with different doses of OVA MS (10, 5, 2.5, 1.25, µg/ml) overnight. After incubation, supernatants were harvested for analysis. Results extracted from this study are summarized in (Figure 54). As we can see there is not relevant stimulation of TLR2 and Null cells, contrary to what we expected. In contrast, there is a slight activation in hTLR4 cells. With this result, we cannot elucidate the immune stimulation pattern of the OVA MS, that will require further studies.

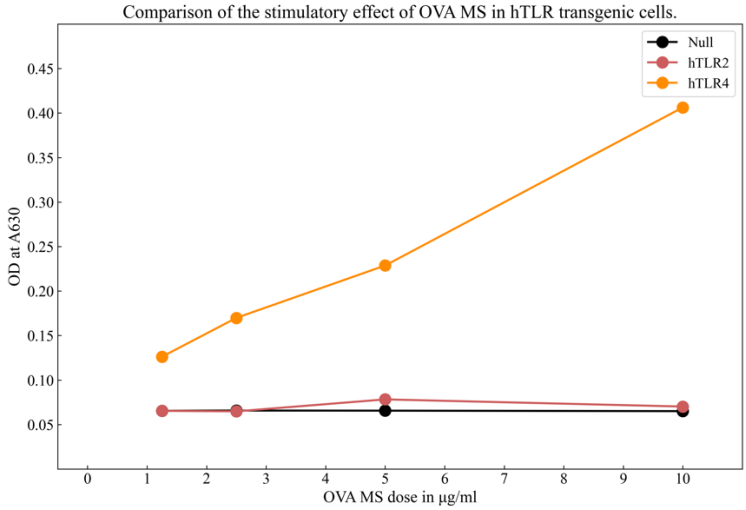

Figure 54. ***Comparison of the stimulatory effect induce by different doses of OVA MS in hTLR transgenic cells.***

9. Comparison of the immune response induced by OVA NS/MS.

After the immunostimulatory analysis of both vaccine candidates, we can definitively conclude that IL-6 and IL-8 release is considerably higher for OVA NS. This outcome may indicate that the immune stimulation induced by OVA MS is weaker, although need to perform a broader study for the cytokine response induced by OVA MS.

We can attribute the immune response induced by OVA NS to a stimulation of the TLR2. However, the pattern recognition receptors mediating in the stimulatory activity of OVA MS remain unclear. This outcome indicates that the particle size might be a key feature in the immune response induced by these spheres, although other aspects like MS aggregation cannot be discarded

10. Discussion.

In this chapter, we developed two different methods to overcome the limitations of the bacterial expression system in the production of a selective cancer vaccine candidate using the IC-Tagging

system. On the one hand, we propose to use the ClearColi® expression technology in combination with the IC-Tagging system. This technology uses genetically modified *E.coli* strain that disables the endotoxin signal. By combining this technology with the IC-Tagging system we were able to produce LPS-free muNS-Mi-derived NS that are loaded with the neoantigen OVA. On the other hand, we used the baculovirus expression system and the IC-Tagging system together to produce OVA-loaded MS. The use of insect cells as the particle factory avoids the presence of the bacterial endotoxin, enabling us to produce endotoxin-free MS. With these two candidates produced, we could perform an intensive study of their immunostimulatory activity and compared whether the differences in size can entail differences on it.

We studied the cytokine induction pattern produce by the OVA NS in PBMCs. Thus, we can assess their stimulatory activity by the release of IL-1β, MCP-1, IL-6, IL-8 and TNF-α in relevant concentration in PBMCs. Besides that, we compared the stimulation pattern induced in PBMCs with the one induced in whole blood, finding that the pattern is very similar in both cases, with the exception of IL-6 release, that is considerably higher in whole blood. This cytokine release may promote antitumor adaptative immunity by inducing the presence of T cells in the TME. On top to that, we can conclude that the OVA NS do trigger a TLR2 mediated pathway, although it may not be the only participant of the immune stimulation provoked by them. The TLR2 stimulation can be a doubled-edge regarding tumor progression, hence further immunostimulatory assays regarding the cytotoxic T lymphocyte stimulation and tumor progression must be performed.

Regarding the immune response induced by OVA MS, we can confirm that the induction of IL-6 and IL-8 release is not as relevant as it is for OVA NS. However, we consider that a deeper study in the cytokine induction profile is required. Moreover, we couldn't elucidate the pattern recognition receptors mediating in the immunostimulatory activity of OVA MS, being a pending point for future studies. These MS tend to aggregate on storage, and this might be also influencing the results that we obtained in this study. Studies are being carried out in our laboratory to try to overcome the aggregation issue and that will undoubtedly help in future experiments with the MS.

Looking ahead to the future, in vivo studies will be performed. We will focus on the study of the cytotoxic T lymphocyte response induced in mice by both candidates. Furthermore, we will study the anti-tumor response enhanced by the OVA loaded NS and MS in mice expressing OVA as a transgene in B16 tumor cells.

CHAPTER III. DESIGN OF A NOVEL VACCINE CANDIDATE METHOD FOR ENVELOPED VIRUSES - SARS-COV-2 AS A MODEL.

CHAPTER III. DESIGN OF A NOVEL VACCINE CANDIDATE METHOD FOR ENVELOPED VIRUSES - SARS-COV-2 AS A MODEL.

1. Introduction.

1.1. Enveloped viruses.

Viruses have developed diverse strategies to infect cells and although some of them remain poorly understood, it is clear that viral structural features are key factors in determining the way they invade their hosts.[138]

Focusing on structural characteristics, all virions share two essential components: the genomic material, either DNA or RNA and the capsid or protein coat. This protein coat, that can be single or multiple layered, is responsible of the structural integrity of the viral genome during infection. [139] Among viral structural proteins, it is common that a nucleocapsid protein is responsible of the formation of the first protein coat that shields the genome.[140]

What differentiates enveloped from non-enveloped viruses are the presence of an outer lipid bilayer usually covered by viral glycoproteins. These proteins are partly inserted in the lipidic envelope and form protrusions on the viral surface. One of their functions is to mediate in the attachment of the virion to the host cell and enable the cell infection. Hence, these proteins are usually the antigens that trigger a protective immune response in susceptible subjects.[140,141] Sometimes, a single viral glycoprotein assumes full responsibility for mediating cell infection. These reasons make the study of the interaction of viral glycoproteins with the host cell receptors a cornerstone in viral vaccine development.[142]

1.2. SARS-Cov2: structure.

Severe acute respiratory syndrome coronavirus 2 (SARS-CoV-2) emerged in 2019, causing an outbreak firstly in China which rapidly spread to the rest of the world, producing a world-wide pandemic without precedents.[143]

SARS-CoV-2, from the family Coronaviridae, genus Betacoronavirus, is a single stranded +RNA virus. Their virions are spherical or ellipsoidal in shape and their size ranges between 100 nm to 116 nm. Their genome stands out for being one of the largest genomes of RNA viruses, containing approximately 30 kb.[144,145] It encodes 16 non-structural proteins, and 4 structural proteins. These

4 structural proteins are named as: Spike (S), Membrane (M), Envelope (E) and Nucleocapsid (N) (Figure 55).[146]

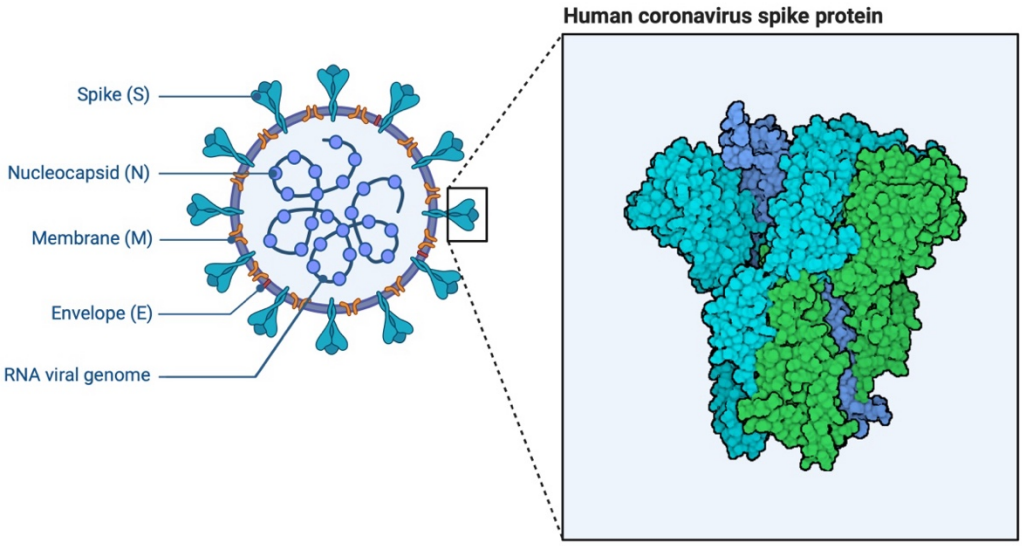

Figure 55. ***Schematic representation of SARS-CoV-2 structure****.*

M protein has been found to play an indispensable role in the viral assembly, by acting as the recruiter of other viral proteins.[147] The E protein is a multifunctional protein that, among other functions, is responsible of forming ion-conductive pores in the host membrane. These pores help in the release of viral particles and the penetration of virus in the cell.[148] The N protein is noteworthy for being the most abundant in the viral particle. Its main function is the RNA binding and its packaging into the nucleocapsid structure. Furthermore, it is implicated in the host cell cycle progression and apoptosis. This protein acts as a highly immunogenic antigen, determining the virulence of the infection and pathogenesis. For this reason, N acts as one of the possible targets in viral vaccination and it can be used as a diagnostic marker of infection.[146,149] However, since the burst of SARS-CoV-2, the S protein has been the one gaining greater attention as is the cell-attachment protein. S protein is a type I transmembrane glycoprotein that mediates in the viral entry into the host cell. This protein forms a trimeric structure that protrudes in the outer part of the viral surface.[150] It can be divided into two different functional domains, named as S1 and S2. S1 contains the receptor binding domain (RBD) that interacts directly with the angiotensin-converting enzyme 2 (ACE2) of the host cell, that acts as a receptor. On the other hand, S2 is the responsible for the fusion to the host cell, by containing the fusion machinery.[151] The S or "spike" protein can exist in two different states preferentially, the prefusion and fusion states, each representing a different structural conformation essential for viral entry. In the prefusion state, S protein can adopt either a closed or open configuration depending on the exposure of the receptor-binding domain (RBD), being these configurations stochastic variants. The receptor-binding site (RBS) remains largely hidden when the RBD are in the down position, regulating interaction with the ACE2 receptor (Figure 56). Once the RBD binds to ACE2, the S protein undergoes a structural

rearrangement, exposing the S2 subunit and inserting the fusion peptide (FP) into the target cell membrane. This leads to refolding into the post fusion form, drawing the viral and cellular membranes together to facilitate fusion and infection.[152]

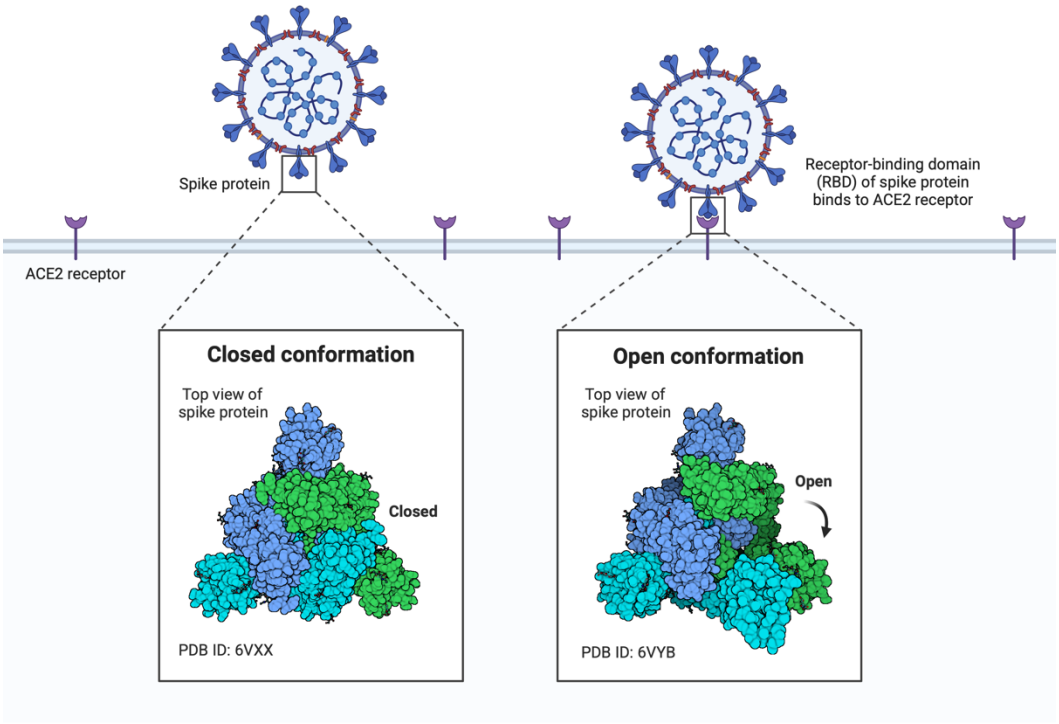

Figure 56. ***Schematic representation of the different conformations of the S protein in its prefusion state.***

Different approaches for the production of SARS-CoV-2 vaccines use particular mutations that stabilize the prefusion state of the S protein to enhance immune response and prevent its spontaneous transition into the post fusion form, thereby maximizing the production of neutralizing antibodies.[152]

1.3. Virus-like particles.

The term 'virus-like particle' (VLP) embraces several biological entities whose architecture mimics the viral structure while lacking genetic material. The usual size for these particles ranges from 2 to 200 nm. These particles gained great importance with the approval of the VLP-based Hepatitis B (HBV) and human papilloma virus (HPV) vaccines in 1986 and 2006 respectively.[153] Studies on both viruses have demonstrated that VLP vaccines induce a robust immune response. They effectively stimulate both cellular and humoral immune responses and present key immune-inducing characteristics, including efficient uptake by dendritic cells (DCs) and neutralizing antibody production.[154,155] As viruses, VLP can be divided in two groups based on their structural characteristics: enveloped and non-enveloped VLP. Enveloped VLPs contain a protein matrix located just inside the host-derived lipid membrane, in which the viral glycoproteins are embedded, whereas non-enveloped VLP lack of the lipid coat and are usually formed by the

spontaneous assembly of genome-free viral capsomers [156] The production of enveloped VLP is more complex, due to the complexity in their composition. Hence, their production still faces great challenges regarding stability and membrane integrity.[157]

2. Objective

The main goal of this chapter was the development of a novel strategy for producing vaccines against enveloped virus, focusing our interest on SARS-CoV-2, taking advantage of the tunable features of the IC-Tagging system.

3. Design and production and characterization of the VLPs.

This section is not shown because it is the subject of a patent application. Hence, it must remain private until intellectual property permissions are registered.

4. Discussion.

In this chapter we developed a novel method for producing VLPs that mimic the structure of SARS-CoV-2. We validated the proper assembly of the particle using various techniques. Besides that, its morphology and dispersion has been thoroughly characterized using various microscopy techniques. These findings highlight the robustness of our production approach and its potential for vaccine development. Moreover, their structural integrity and stability under physiological conditions has also been partially assessed, although more studies are currently being performed to comprehensively characterize VLP stability.

In the future, we will try to further enhance the thermal stability of our particles, what is crucial for the vaccine storage. Besides that, we will conduct immunogenicity studies to assess their ability produce different type of antibodies, in combination with the increase in the amount of B lymphocytes and T lymphocytes. The immune response induced in vivo will be also characterized using different administration ways of the vaccine candidates: intranasal, intraperitoneal and intramuscular administration, in order to optimize its characterization for pre-clinical studies.

To conclude, we hope that this nature-inspired technology may pave a new way to develop a new strategy for the easy design of vaccines against different enveloped viruses. Furthermore, the ease of manufacturing and its low cost will make this vaccine clearly advantageous with respect to the

already produced ones. This last feature will entail a significant approach for the global access to a novel and effective treatment for the disease.

CONCLUSIONS

The results obtained in the course of this doctoral thesis led us to withdraw the following conclusions:

- The cell sensor developed by combining the IC-Tagging system with the bimolecular fluorescence complementation assay efficiently detects the retrotranslocation of two different ERAD substates.

- This sensor presents enough sensitivity to detect and quantify slight changes in protein expression, making it a great alternative compared to the current strategies for detection of retrotranslocated substrates.

- We developed two different cancer vaccine candidates that overcome the contamination produced by bacterial endotoxins. In both cases the neoantigen OVA is encapsulated in either a protein nanoparticle or microparticle respectively.

- Both vaccine candidates present a robust cytokine response, although the difference in the particle size implies changes in the immune stimulatory pathways elicited by the particles.

- We designed a new strategy and protocol to develop vaccines against enveloped viruses. This vaccine presents the advantage of the ease of manufacturing and its low cost of production.

BIBLIOGRAPHY

1. Mertens, P. The dsRNA viruses. *Virus Research* **101**, 3–13 (2004).

2. P. Urbano & Urbano, F. P. The Reoviridae family. *Comp Immunol Microbiol Infect Dis* **17**, 151–161 (1994).

3. Brandariz-Nuñez, A., Menaya-Vargas, R., Benavente, J. & Martinez-Costas, J. A Versatile Molecular Tagging Method for Targeting Proteins to Avian Reovirus muNS Inclusions. Use in Protein Immobilization and Purification. *PLOS ONE* **5**, e13961 (2010).

4. Hulo, C. *et al.* ViralZone: a knowledge resource to understand virus diversity. *Nucleic Acids Res* **39**, D576-582 (2011).

5. Day, J. M. The diversity of the orthoreoviruses: molecular taxonomy and phylogentic divides. *Infect Genet Evol* **9**, 390–400 (2009).

6. Dryden, K. A. *et al.* Early steps in reovirus infection are associated with dramatic changes in supramolecular structure and protein conformation: analysis of virions and subviral particles by cryoelectron microscopy and image reconstruction. *J Cell Biol* **122**, 1023–1041 (1993).

7. Benavente, J. & Martínez-Costas, J. Avian reovirus: structure and biology. *Virus Res* **123**, 105–119 (2007).

8. Rosenberger, J. K., Sterner, F. J., Botts, S., Lee, K. P. & Margolin, A. In vitro and in vivo characterization of avian reoviruses. Pathogenicity and antigenic relatedness of several avian reovirus isolates. *Avian Dis* **33**, 535–544 (1989).

9. Egana-Labrin, S. & Broadbent, A. J. Avian reovirus: a furious and fast evolving pathogen. *J. Med. Microbiol.* **72**, 001761 (2023).

10. Spandidos, D. A. & Graham, A. F. Physical and chemical characterization of an avian reovirus. *J Virol* **19**, 968–976 (1976).

11. Martinez-Costas, J., Varela, R. & Benavente, J. Endogenous enzymatic activities of the avian reovirus S1133: identification of the viral capping enzyme. *Virology* **206**, 1017–1026 (1995).

12. Martínez-Costas, J., Grande, A., Varela, R., García-Martínez, C. & Benavente, J. Protein architecture of avian reovirus S1133 and identification of the cell attachment protein. *J Virol* **71**, 59–64 (1997).

13. Schnitzer, T. J., Ramos, T. & Gouvea, V. Avian Reovirus Polypeptides: Analysis of Intracellular Virus-Specified Products, Virions, Top Component, and Cores. *J Virol* **43**, 1006–1014 (1982).

14. Zhang, X. *et al.* Structure of avian orthoreovirus virion by electron cryomicroscopy and image reconstruction. *Virology* **343**, 25–35 (2005).

15. Grande, A., Rodriguez, E., Costas, C., Everitt, E. & Benavente, J. Oligomerization and cell-binding properties of the avian reovirus cell-attachment protein sigmaC. *Virology* **274**, 367–377 (2000).

16. Shapouri, M. R., Arella, M. & Silim, A. Evidence for the multimeric nature and cell binding ability of avian reovirus sigma 3 protein. *J Gen Virol* **77 (Pt 6)**, 1203–1210 (1996).

17. Benavente, J. & Martínez-Costas, J. Early steps in avian reovirus morphogenesis. *Curr Top Microbiol Immunol* **309**, 67–85 (2006).

18. Duncan, R. The Low pH-Dependent Entry of Avian Reovirus Is Accompanied by Two Specific Cleavages of the Major Outer Capsid Protein μ2C. *Virology* **219**, 179–189 (1996).

19. Rhim, J. S., Jordan, L. E. & Mayor, H. D. Cytochemical, fluorescent-antibody and electron microscopic studies on the growth of reovirus (ECHO 10) in tissue culture. *Virology* **17**, 342–355 (1962).

20. Borodavka, A., Ault, J., Stockley, P. G. & Tuma, R. Evidence that avian reovirus σNS is an RNA chaperone: implications for genome segment assortment. *Nucleic Acids Res* **43**, 7044–7057 (2015).

21. Tourís-Otero, F., Cortez-San Martín, M., Martínez-Costas, J. & Benavente, J. Avian reovirus morphogenesis occurs within viral factories and begins with the selective recruitment of sigmaNS and lambdaA to microNS inclusions. *J Mol Biol* **341**, 361–374 (2004).

22. Bodelón, G., Labrada, L., Martínez-Costas, J. & Benavente, J. Modification of Late Membrane Permeability in Avian Reovirus-infected Cells. *J. Biol. Chem.* **277**, 17789–17796 (2002).

23. Duncan, R., Chen, Z., Walsh, S. & Wu, S. Avian Reovirus-Induced Syncytium Formation Is Independent of Infectious Progeny Virus Production and Enhances the Rate, but Is Not Essential, for Virus-Induced Cytopathology and Virus Egress. *Virology* **224**, 453–464 (1996).

24. Rodríguez-Grille, J., Busch, L. K., Martínez-Costas, J. & Benavente, J. Avian reovirus-triggered apoptosis enhances both virus spread and the processing of the viral nonstructural muNS protein. *Virology* **462**, 49 (2014).

25. Touris-Otero, F., Martínez-Costas, J., Vakharia, V. N. & Benavente, J. Avian reovirus nonstructural protein μNS forms viroplasm-like inclusions and recruits protein σNS to these structures. *Virology* **319**, 94–106 (2004).

26. Brandariz-Nuñez, A., Menaya-Vargas, R., Benavente, J. & Martinez-Costas, J. Avian Reovirus μNS Protein Forms Homo-Oligomeric Inclusions in a Microtubule-Independent Fashion, Which Involves Specific Regions of Its C-Terminal Domain. *J Virol* **84**, 4289–4301 (2010).

27. Yarbrough, D., Rebekka. M Watcher, Kallio, K., Matz, M. V. & Remington, S. J. Refined crystal structure of DsRed, a red fluorescent protein from coral, at 2.0-Å resolution. *PNAS* **98**, 462–467 (2001).

28. Brandariz-Nuñez, A., Otero-Romero, I., Benavente, J. & Martinez-Costas, J. M. IC-tagged proteins are able to interact with each other and perform complex reactions when integrated into muNS-derived inclusions. *J Biotechnol* **155**, 284–286 (2011).

29. Calvo-Pinilla, E. *et al.* Prime-Boost Vaccination Based on Nanospheres and MVA Encoding the Nucleoprotein of Crimean-Congo Hemorrhagic Fever Virus Elicits Broad Immune Responses. *Vaccines* **13**, 291 (2025).

30. Pose-Boirazian, T. *et al.* Chemical and thermal stabilization of CotA laccase via a novel one-step expression and immobilization in muNS-Mi nanospheres. *Sci Rep* **11**, 2802 (2021).

31. Barreiro-Piñeiro, N., Pose-Boirazian, T., Menaya-Vargas, R. & Martínez-Costas, J. M. Production and Purification of Candidate Subunit Vaccines by IC-Tagging Protein Encapsulation. in *Vaccine Technologies for Veterinary Viral Diseases: Methods and Protocols* 27–40 (2022).

32. Brandariz-Nuñez, A., Menaya-Vargas, R., Benavente, J. & Martinez-Costas, J. IC-Tagging and Protein Relocation to ARV muNS Inclusions: A Method to Study Protein-Protein Interactions in the Cytoplasm or Nucleus of Living Cells. *PLOS ONE* **5**, e13785 (2010).

33. Barreiro-Piñeiro, N., Lostalé-Seijo, I., Varela-Calviño, R., Benavente, J. & Martínez-Costas, J. M. IC-Tagging methodology applied to the expression of viral glycoproteins and the difficult-to-express membrane-bound IGRP autoantigen. *Sci Rep* **8**, 16286 (2018).

34. Barreiro-Piñeiro, N. *et al.* Using IC-Tagging Methodology for Production and Purification of Epitope-Loaded Protein Microspheres for Vaccination. in *Vaccine Technologies for Veterinary Viral Diseases: Methods and Protocols* 25–34 (Springer, 2016).

35. Jiménez-Cabello, L. *et al.* Nanoparticle- and Microparticle-Based Vaccines against Orbiviruses of Veterinary Importance. *Vaccines* **10**, 1124 (2022).

36. Marín-López, A. *et al.* VP2, VP7, and NS1 proteins of bluetongue virus targeted in avian reovirus muNS-Mi microspheres elicit a protective immune response in IFNAR(−/−) mice. *Antiviral Res.* **110**, 42–51 (2014).

37. Marín-López, A. *et al.* Microspheres-prime/rMVA-boost vaccination enhances humoral and cellular immune response in IFNAR(-/-) mice conferring protection against serotypes 1 and 4 of bluetongue virus. *Antiviral Res.* **142**, 55–62 (2017).

38. Marín-López, A. *et al.* Cross-protective immune responses against African horse sickness virus after vaccination with protein NS1 delivered by avian reovirus muNS microspheres and modified vaccinia virus Ankara. *Vaccine* **38**, 882–889 (2020).

39. Dimitrov, D. S. Therapeutic Proteins. in *Therapeutic Proteins: Methods and Protocols* 1–26 (2012).

40. Leader, B., Baca, Q. J. & Golan, D. E. Protein therapeutics: a summary and pharmacological classification. *Nat Rev Drug Discov* **7**, 21–39 (2008).

41. Reichert, J. M. Trends in development and approval times for new therapeutics in the United States. *Nat Rev Drug Discov* **2**, 695–702 (2003).

42. Pillai, O. & Panchagnula, R. Insulin therapies – past, present and future. *Drug Discov. Today* **6**, 1056–1061 (2001).

43. Goeddel, D. V. *et al.* Expression in Escherichia coli of chemically synthesized genes for

human insulin. *PNAS* **76**, 106 (1979).

44. Ebrahimi, S. B. & Samanta, D. Engineering protein-based therapeutics through structural and chemical design. *Nat Commun* **14**, 2411 (2023).

45. Otvos, L. & Wade, J. D. Current challenges in peptide-based drug discovery. *Front. Chem.* **2**, (2014).

46. Ilangala, A. B., Lechanteur, A., Fillet, M. & Piel, G. Therapeutic peptides for chemotherapy: Trends and challenges for advanced delivery systems. *Eur. J. Pharm. Biopharm.* **167**, 140–158 (2021).

47. Joseph, M., Trinh, H. M. & Mitra, A. K. Peptide and Protein-Based Therapeutic Agents. in *Emerging Nanotechnologies for Diagnostics, Drug Delivery and Medical Devices* 145–167 (2017).

48. Bouzo, B. L., Calvelo, M., Martín-Pastor, M., García-Fandiño, R. & de la Fuente, M. In Vitro-In Silico Modeling Approach to Rationally Designed Simple and Versatile Drug Delivery Systems. *J Phys Chem B* **124**, 5788–5800 (2020).

49. Lu, Y., Sun, W. & Gu, Z. Stimuli-responsive nanomaterials for therapeutic protein delivery. *J. Control. Release.* **194**, 1–19 (2014).

50. Di, L. Strategic Approaches to Optimizing Peptide ADME Properties. *AAPS J* **17**, 134–143 (2015).

51. Yadav, S. C., Kumari, A. & Yadav, R. Development of peptide and protein nanotherapeutics by nanoencapsulation and nanobioconjugation. *Peptides* **32**, 173–187 (2011).

52. Phogat, N., Kohl, M., Uddin, I. & Jahan, A. Interaction of Nanoparticles With Biomolecules, Protein, Enzymes, and Its Applications. *Precis. Med.* 253–276 (2018).

53. Wilczewska, A. Z., Niemirowicz, K., Markiewicz, K. H. & Car, H. Nanoparticles as drug delivery systems. *Pharmacol Rep* **64**, 1020–1037 (2012).

54. Duhem, N., Danhier, F. & Préat, V. Vitamin E-based nanomedicines for anti-cancer drug delivery. *J. Control. Release* **182**, 33–44 (2014).

55. Farokhzad, O. C. & Langer, R. Impact of Nanotechnology on Drug Delivery. *ACS Nano* **3**, 16–20 (2009).

56. He, H., Liu, L., Morin, E. E., Liu, M. & Schwendeman, A. Survey of Clinical Translation of Cancer Nanomedicines-Lessons Learned from Successes and Failures. *Acc Chem Res* **52**, 2445–2461 (2019).

57. Anselmo, A. C. & Mitragotri, S. Nanoparticles in the clinic. *Bioeng. Transl. Med* **1**, 10–29 (2016).

58. Shan, X. *et al.* Current approaches of nanomedicines in the market and various stage of clinical translation. *Acta Pharm. Sin. B.* **12**, 3028 (2022).

59. Kaitin, K. I., DiCerbo, P. A. & Lasagna, L. The New Drug Approvals of 1987, 1988, and 1989: Trends in Drug Development. *J. Clin. Pharmacol.* **31**, 116–122 (1991).

60. Anselmo, A. C. & Mitragotri, S. Nanoparticles in the clinic: An update. *Bioeng. Transl. Med* **4**, e10143 (2019).

61. Rios-Doria, J. *et al.* Doxil Synergizes with Cancer Immunotherapies to Enhance Antitumor Responses in Syngeneic Mouse Models. *Neoplasia* **17**, 661–670 (2015).

62. Meo, S. A., Bukhari, I. A., Akram, J., Meo, A. S. & Klonoff, D. C. COVID-19 vaccines: comparison of biological, pharmacological characteristics and adverse effects of Pfizer/BioNTech and Moderna Vaccines. *Eur Rev Med Pharmacol Sci* **25**, 1663–1669 (2021).

63. Joudeh, N. & Linke, D. Nanoparticle classification, physicochemical properties, characterization, and applications: a comprehensive review for biologists. *J. Nanotechnol.* **20**, 262 (2022).

64. Mitragotri, S. & Stayton, P. Organic nanoparticles for drug delivery and imaging. *MRS Bull.* **39**, 219–223 (2014).

65. Mauter, M. S. & Elimelech, M. Environmental Applications of Carbon-Based Nanomaterials. *Environ. Sci. Technol.* **42**, 5843–5859 (2008).

66. Yuan, X., Zhang, X., Sun, L., Wei, Y. & Wei, X. Cellular Toxicity and Immunological Effects of Carbon-based Nanomaterials. *Part. Fibre Toxicol* **16**, 18 (2019).

67. Cho, S.-J. *et al.* Characterization and magnetic properties of core/shell structured Fe/Au nanoparticles. *J. Appl. Phys.* **95**, 6804–6806 (2004).

68. Kohane, D. S. Microparticles and nanoparticles for drug delivery. *Biotechnol. Bioeng.* **96**, 203–209 (2007).

69. Modi, D., Hussain, M. S., Ainampudi, S. & Prajapati, B. G. Long acting injectables for the treatment of prostate cancer. *J. Drug Deliv. Sci. Technol.* **100**, 105996 (2024).

70. Sambrook, H., Fritsch, E. F. & Maniatis, T. *Molecular Cloning: A Laboratory Manual*. vol. 30 (Cold Spring Harbor, 1990).

71. Pose Boirazian, T. Novel protein immobilization approaches for the development of vaccine candidates and enzymatic reactors. (2021).

72. Laemmli, U. K. Cleavage of Structural Proteins during the Assembly of the Head of Bacteriophage T4. *Nature* **227**, 680–685 (1970).

73. Luirink, J. & Sinning, I. SRP-mediated protein targeting: structure and function revisited. *Biochimica et Biophysica Acta (BBA) - Molecular Cell Research* **1694**, 17–35 (2004).

74. Matlack, K. E. S., Mothes, W. & Rapoport, T. A. Protein Translocation: Tunnel Vision. *Cell* **92**, 381–390 (1998).

75. Nyfeler, B., Michnick, S. W. & Hauri, H.-P. Capturing protein interactions in the secretory pathway of living cells. *PNAS* **102**, 6350–6355 (2005).

76. Lemus, L. & Goder, V. Regulation of Endoplasmic Reticulum-Associated Protein Degradation (ERAD) by Ubiquitin. *Cells* **3**, 824–847 (2014).

77. Matlack, K. E. S., Misselwitz, B., Plath, K. & Rapoport, T. A. BiP Acts as a Molecular

Ratchet during Posttranslational Transport of Prepro-α Factor across the ER Membrane. *Cell* **97**, 553–564 (1999).

78. Nakatsukasa, K. & Brodsky, J. L. The Recognition and Retrotranslocation of Misfolded Proteins from the Endoplasmic Reticulum. *Traffic* **9**, 861–870 (2008).

79. Wiseman, R. L., Mesgarzadeh, J. S. & Hendershot, L. M. Reshaping endoplasmic reticulum quality control through the unfolded protein response. *Mol.Cell* **82**, 1477–1491 (2022).

80. Kleizen, B. & Braakman, I. Protein folding and quality control in the endoplasmic reticulum. *Curr. Opin. Cell Biol.* **16**, 343–349 (2004).

81. Elia, F., Yadhanapudi, L., Tretter, T. & Römisch, K. The N-terminus of Sec61p plays key roles in ER protein import and ERAD. *PLOS ONE* **14**, e0215950 (2019).

82. Christianson, J. C. & Ye, Y. Cleaning up in the endoplasmic reticulum: ubiquitin in charge. *Nat Struct Mol Biol* **21**, 325–335 (2014).

83. Bedford, L., Paine, S., Sheppard, P. W., Mayer, R. J. & Roelofs, J. Assembly, Structure and Function of the 26S proteasome. *Trends Cell Biol* **20**, 391–401 (2010).

84. Christianson, J. C. *et al.* Defining human ERAD networks through an integrative mapping strategy. *Nat Cell Biol* **14**, 93–105 (2012).

85. Afshar, N., Black, B. E. & Paschal, B. M. Retrotranslocation of the Chaperone Calreticulin from the Endoplasmic Reticulum Lumen to the Cytosol. *Mol Cell Biol* **25**, 8844–8853 (2005).

86. Wahlman, J. *et al.* Real-Time Fluorescence Detection of ERAD Substrate Retrotranslocation in a Mammalian In Vitro System. *Cell* **129**, 943–955 (2007).

87. Lee, Y.-K., Brewer, J. W., Hellman, R. & Hendershot, L. M. BiP and Immunoglobulin Light Chain Cooperate to Control the Folding of Heavy Chain and Ensure the Fidelity of Immunoglobulin Assembly. *Mol Biol Cell* **10**, 2209–2219 (1999).

88. Bole, D. G., Hendershot, L. M. & Kearney, J. F. Posttranslational association of immunoglobulin heavy chain binding protein with nascent heavy chains in nonsecreting and secreting hybridomas. *J Cell Biol* **102**, 1558–1566 (1986).

89. Leitzgen, K., Knittler, M. R. & Haas, I. G. Assembly of immunoglobulin light chains as a prerequisite for secretion. A model for oligomerization-dependent subunit folding. *J Biol Chem* **272**, 3117–3123 (1997).

90. Cowan, N. J., Secher, D. S. & Milstein, C. Intracellular immunoglobulin chain synthesis in non-secreting variants of a mouse myeloma: Detection of inactive light-chain messenger RNA. *J. Mol. Biol.* **90**, 691–701 (1974).

91. Lomas, D. A. & Mahadeva, R. α1-Antitrypsin polymerization and the serpinopathies: pathobiology and prospects for therapy. *J Clin Invest* **110**, 1585–1590 (2002).

92. Sifers, R. N., Brashears-Macatee, S., Kidd, V. J., Muensch, H. & Woo, S. L. A frameshift mutation results in a truncated alpha 1-antitrypsin that is retained within the rough endoplasmic

reticulum. *J Biol Chem* **263**, 7330–7335 (1988).

93. Zimmer, M. Green Fluorescent Protein (GFP): Applications, Structure, and Related Photophysical Behavior. *Chem. Rev.* **102**, 759–782 (2002).

94. Yang, F., Moss, L. G. & Phillips, G. N. The molecular structure of green fluorescent protein. *Nat Biotechnol* **14**, 1246–1251 (1996).

95. Kodama, Y. & Hu, C.-D. Bimolecular fluorescence complementation (BiFC): A 5-year update and future perspectives. *BioTechniques* **53**, 285–298 (2012).

96. Ghosh, I., Hamilton, A. D. & Regan, L. Antiparallel Leucine Zipper-Directed Protein Reassembly: Application to the Green Fluorescent Protein. *J. Am. Chem. Soc.* **122**, 5658–5659 (2000).

97. Barreiro Piñeiro, N. IC-Tagging: Plataforma universal para la producción de microesferas proteicas para aplicaciones biotecnológicas. (Universidade de Santiago de Compostela, 2018).

98. Cabantous, S., Terwilliger, T. C. & Waldo, G. S. Protein tagging and detection with engineered self-assembling fragments of green fluorescent protein. *Nat Biotechnol* **23**, 102–107 (2005).

99. Esfahani, K. *et al.* A Review of Cancer Immunotherapy: From the Past, to the Present, to the Future. *Curr. Oncol.* **27**, 87–97 (2020).

100. Riley, R. S., June, C. H., Langer, R. & Mitchell, M. J. Delivery technologies for cancer immunotherapy. *Nat Rev Drug Discov* **18**, 175–196 (2019).

101. Ye, Z., Qian, Q., Jin, H. & Qian, Q. Cancer vaccine: learning lessons from immune checkpoint inhibitors. *J Cancer* **9**, 263–268 (2018).

102. Kaczmarek, M. *et al.* Cancer Vaccine Therapeutics: Limitations and Effectiveness—A Literature Review. *Cells* **12**, 2159 (2023).

103. Tay, B. Q. *et al.* Evolution of Cancer Vaccines—Challenges, Achievements, and Future Directions. *Vaccines* **9**, 535 (2021).

104. Lin, M. J. *et al.* Cancer vaccines: the next immunotherapy frontier. *Nat Cancer* **3**, 911–926 (2022).

105. Liu, J. *et al.* Cancer vaccines as promising immuno-therapeutics: platforms and current progress. *Journal of Hematology & Oncology* **15**, 28 (2022).

106. Buonaguro, L. & Tagliamonte, M. Selecting Target Antigens for Cancer Vaccine Development. *Vaccines (Basel)* **8**, 615 (2020).

107. Dash, B., Shapiro, M. J., Chung, J. Y., Arocha, S. R. & Shapiro, V. S. Treg-specific deletion of NKAP results in severe, systemic autoimmunity due to peripheral loss of Tregs. *J. Autoimmun.* **89**, 139 (2018).

108. Bowen, W. S., Svrivastava, A. K., Batra, L., Barsoumian, H. & Shirwan, H. Current challenges for cancer vaccine adjuvant development. *Expert Rev. Vaccines* **17**, 207–215 (2018).

109. Duthie, M. S., Windish, H. P., Fox, C. B. & Reed, S. G. Use of defined TLR ligands as

adjuvants within human vaccines. *Immunol. Rev.* **239**, 178–196 (2011).

110. Di Pasquale, A., Preiss, S., Tavares Da Silva, F. & Garçon, N. Vaccine Adjuvants: from 1920 to 2015 and Beyond. *Vaccines* **3**, 320–343 (2015).

111. Takeuchi, O. & Akira, S. Pattern Recognition Receptors and Inflammation. *Cell* **140**, 805–820 (2010).

112. Paston, S. J., Brentville, V. A., Symonds, P. & Durrant, L. G. Cancer Vaccines, Adjuvants, and Delivery Systems. *Front. Immunol.* **12**, (2021).

113. Iribarren, K. *et al.* Trial Watch: Immunostimulation with Toll-like receptor agonists in cancer therapy. *Oncoimmunology* **5**, (2015).

114. Villano, J. L., Mehta, D. & Radhakrishnan, L. Abraxane® induced life-threatening toxicities with metastatic breast cancer and hepatic insufficiency. *Invest. New Drugs* **24**, 455–456 (2006).

115. Lohcharoenkal, W., Wang, L., Chen, Y. C. & Rojanasakul, Y. Protein Nanoparticles as Drug Delivery Carriers for Cancer Therapy. *Biomed Res. Int.* **2014**, 180549 (2014).

116. Shao, K. *et al.* Nanoparticle-Based Immunotherapy for Cancer. *ACS Nano* **9**, 16–30 (2015).

117. Medzhitov, R. Toll-like receptors and innate immunity. *Nat Rev Immunol* **1**, 135–145 (2001).

118. Duan, T., Du, Y., Xing, C., Wang, H. Y. & Wang, R.-F. Toll-Like Receptor Signaling and Its Role in Cell-Mediated Immunity. *Front. Immunol.* **13**, (2022).

119. Iwasaki, A. & Medzhitov, R. Toll-like receptor control of the adaptive immune responses. *Nat Immunol* **5**, 987–995 (2004).

120. Fore, F., Indriputri, C., Mamutse, J. & Nugraha, J. TLR10 and Its Unique Anti-Inflammatory Properties and Potential Use as a Target in Therapeutics. *Immune Netw* **20**, e21 (2020).

121. Kawai, T. & Akira, S. The role of pattern-recognition receptors in innate immunity: update on Toll-like receptors. *Nat Immunol* **11**, 373–384 (2010).

122. McClure, R. & Massari, P. TLR-Dependent Human Mucosal Epithelial Cell Responses to Microbial Pathogens. *Front Immunol* **5**, 386 (2014).

123. Medzhitov, R. Recognition of microorganisms and activation of the immune response. *Nature* **449**, 819–826 (2007).

124. Diebold, S. S. Activation of dendritic cells by toll-like receptors and C-type lectins. *Handb Exp Pharmacol* 3–30 (2009) doi:10.1007/978-3-540-71029-5_1.

125. Akira, S., Takeda, K. & Kaisho, T. Toll-like receptors: critical proteins linking innate and acquired immunity. *Nat Immunol* **2**, 675–680 (2001).

126. Reis e Sousa, C. Toll-like receptors and dendritic cells: for whom the bug tolls. *Semin Immunol* **16**, 27–34 (2004).

127. Urban-Wojciuk, Z. *et al.* The Role of TLRs in Anti-cancer Immunity and Tumor Rejection. *Front. Immunol.* **10**, (2019).

128. Lee, S. & Margolin, K. Cytokines in Cancer Immunotherapy. *Cancers* **3**, 3856–3893 (2011).

129. Liu, C. *et al.* Cytokines: From Clinical Significance to Quantification. *Adv. Sci.* **8**, 2004433 (2021).

130. Boshtam, M., Asgary, S., Kouhpayeh, S., Shariati, L. & Khanahmad, H. Aptamers Against Pro- and Anti-Inflammatory Cytokines: A Review. *Inflammation* **40**, 340–349 (2017).

131. Lin, W.-W. & Karin, M. A cytokine-mediated link between innate immunity, inflammation, and cancer. *J Clin Invest* **117**, 1175–1183 (2007).

132. Berraondo, P. *et al.* Cytokines in clinical cancer immunotherapy. *Br J Cancer* **120**, 6–15 (2019).

133. Conlon, K. C., Miljkovic, M. D. & Waldmann, T. A. Cytokines in the Treatment of Cancer. *J Interferon Cytokine Res* **39**, 6–21 (2019).

134. Habibi, N. *et al.* Engineered Ovalbumin Nanoparticles for Cancer Immunotherapy. *Adv. Ther.* **3**, 2000100 (2020).

135. Karandikar, S. H. *et al.* Identification of epitopes in ovalbumin that provide insights for cancer neoepitopes. *JCI Insight* **4**, e127882 (2019).

136. Jenika, D. *et al.* In vivo assembly of epitope-coated biopolymer particles that induce anti-tumor responses. *npj Vaccines* **9**, 1–11 (2024).

137. van der Maaden, K. *et al.* Ovalbumin-coated pH-sensitive microneedle arrays effectively induce ovalbumin-specific antibody and T-cell responses in mice. *Eur. J. Pharm. Biopharm.* **88**, 310–315 (2014).

138. Klasse, P. J., Bron, R. & Marsh, M. Mechanisms of enveloped virus entry into animal cells. *Adv. Drug Deliv. Rev.* **34**, 65–91 (1998).

139. Gelderblom, H. R. Structure and Classification of Viruses. in *Medical Microbiology* (ed. Baron, S.) (University of Texas Medical Branch at Galveston, 1996).

140. Holland Cheng, R. *et al.* Nucleocapsid and glycoprotein organization in an enveloped virus. *Cell* **80**, 621–630 (1995).

141. Morein, B. & Simons, K. Subunit vaccines against enveloped viruses: virosomes, micelles and other protein complexes. *Vaccine* **3**, 83–93 (1985).

142. Rey, F. A. & Lok, S.-M. Common Features of Enveloped Viruses and Implications for Immunogen Design for Next-Generation Vaccines. *Cell* **172**, 1319–1334 (2018).

143. Acuti Martellucci, C. *et al.* SARS-CoV-2 pandemic: An overview. *Adv. Biol. Regul.* **77**, 100736 (2020).

144. Peacock, T. P., Penrice-Randal, R., Hiscox, J. A. & Barclay, W. S. SARS-CoV-2 one year on: evidence for ongoing viral adaptation. *J Gen Virol* **102**, 001584 (2021).

145. Hardenbrook, N. J. & Zhang, P. A structural view of the SARS-CoV-2 virus and its assembly. *Curr. Opin. Virol.* **52**, 123–134 (2022).

146. Wu, W., Cheng, Y., Zhou, H., Sun, C. & Zhang, S. The SARS-CoV-2 nucleocapsid protein: its role in the viral life cycle, structure and functions, and use as a potential target in the development of vaccines and diagnostics. *Virol J* **20**, 6 (2023).

147. Zhang, Z. *et al.* Structure of SARS-CoV-2 membrane protein essential for virus assembly. *Nat Commun* **13**, 4399 (2022).

148. Kuzmin, A., Orekhov, P., Astashkin, R., Gordeliy, V. & Gushchin, I. Structure and dynamics of the SARS-CoV-2 envelope protein monomer. *Proteins:Struct., Funct., Bioinf.* **90**, 1102–1114 (2022).

149. Kang, S. *et al.* Crystal structure of SARS-CoV-2 nucleocapsid protein RNA binding domain reveals potential unique drug targeting sites. *Acta Pharm. Sin. B.* **10**, 1228–1238 (2020).

150. Tortorici, M. A. *et al.* Structural basis for human coronavirus attachment to sialic acid receptors. *Nat Struct Mol Biol* **26**, 481–489 (2019).

151. Walls, A. C. *et al.* Structure, Function, and Antigenicity of the SARS-CoV-2 Spike Glycoprotein. *Cell* **181**, 281-292.e6 (2020).

152. Carnell, G. W. *et al.* SARS-CoV-2 Spike Protein Stabilized in the Closed State Induces Potent Neutralizing Responses. *J Virol* **95**, e0020321 (2021).

153. Zeltins, A. Construction and characterization of virus-like particles: a review. *Mol Biotechnol* **53**, 92–107 (2013).

154. Netter, H. J., Woo, W.-P., Tindle, R., Macfarlan, R. I. & Gowans, E. J. Immunogenicity of recombinant HBsAg/HCV particles in mice pre-immunised with hepatitis B virus-specific vaccine. *Vaccine* **21**, 2692–2697 (2003).

155. Harro, C. D. *et al.* Safety and immunogenicity trial in adult volunteers of a human papillomavirus 16 L1 virus-like particle vaccine. *J Natl Cancer Inst* **93**, 284–292 (2001).

156. Nooraei, S. *et al.* Virus-like particles: preparation, immunogenicity and their roles as nanovaccines and drug nanocarriers. *J. Nanobiotechnology* **19**, 59 (2021).

157. Dai, S., Wang, H. & Deng, F. Advances and challenges in enveloped virus-like particle (VLP)-based vaccines. *J Immunol. Sci.* **2**, (2018).

DECLARATION OF CONFLICT OF INTEREST.

Chapter 3 is the subject of a patent application of which I am one of the authors. I affirm that all research, data analysis, and conclusions presented in this work have been conducted with academic integrity and without any financial, personal, or professional interests that could influence its content with the only exception of the mentioned patent.

DECLARATION OF FIGURES AUTHORSHIP.

I declare that all figures and tables included in my thesis titled "IC-Tagging System: From Protein Tracking to Therapeutic Applications" are of my own authorship, except where otherwise indicated. Any figures not created by me are properly credited to their respective sources.

Figures of my own authorship were created with BioRender under a paid subscription.

PERMISSION TO PUBLISH IMAGES AND FIGURES.

- Figure **3.** Avian reovirus entry under an electron microscope. (Adapted with permissions from ref 17, Copyright © 2006, Springer Nature).

Order Summary

Licensee:	Miss. Paula sanchez Gascon
Order Date:	Mar 19, 2025
Order Number:	5992391480954
Publication:	Springer eBook
Title:	Early Steps in Avian Reovirus Morphogenesis
Type of Use:	Thesis/Dissertation
Order Total:	0.00 EUR

- **Figure 5.** Immunofluorescence of muNS and different truncation mutants and their capability to generate inclusions. Protein muNS and the different versions were observed in green by indirect immunofluorescence and nuclei were stained blue with DAPI. Amino acid composition of each protein is stated by residue numbers. (Adapted with permissions from ref 26, Copyright © 2010 American Society for Microbiology.)

Order Summary:
Order date: 19 Mar 2025
Order number: 1590011
No. of items: 1
Order total: 0,00 EUR
Order license ID link(s): 1590011-1.

- **Figure 7.** A. Immunofluorescence analysis of the roles of the different domains of muNS in the formation of viral inclusions. (Adapted with permissions from ref 26, Copyright © 2010 American Society for Microbiology) B. Punctual mutations of residues H487 and 489 and their effect in viral inclusion formation. In both images protein muNS and the different versions were observed in green by indirect immunofluorescence and nuclei were stained blue with DAPI. (Adapted with permissions from ref 26, Copyright © 2010 American Society for Microbiology).

Order Summary:
Order date: 19 Mar 2025
Order number: 1590014
No. of items: 1
Order total: 0,00 EUR
Order license ID link(s): 1590014-1.

- **Figure 10.** Immunofluorescence analysis showing the distribution of the dsRed protein in the cell in the absence (upper panel) or presence (lower panel) of MS. Protein dsRed is observed in red, muNS is labelled with green antibody and nuclei were stained blue with DAPI. The presence of the IC tag at the C or N terminus of DsRED is indicated in the drawings. (Adapted with permissions from ref 28, Copyright © 2011 Elsevier B.V)

Order Summary

Licensee:	Miss. Paula sanchez Gascon
Order Date:	Mar 19, 2025
Order Number:	5992441476032
Publication:	Journal of Biotechnology
Title:	IC-tagged proteins are able to interact with each other and perform complex reactions when integrated into muNS-derived inclusions
Type of Use:	reuse in a thesis/dissertation
Order Total:	0.00 EUR

- **Figure 11.** Comparison of microscopy images of eukaryotic and prokaryotic-produced viral inclusions. A. Bright field imagen of MS produced in Sf9 cells via baculovirus expression system. B. Electron microscopy image of NS produced in BL21 bacteria, showing the production of one NS per bacteria (Adapted with permissions from 29, Copyright © 2025 by the authors).

Figure 13. Immunofluorescence analysis of the validation of the interaction of p53 and Tag. MuNS is labelled with green antibody, Tag is labelled with red antibody and nuclei were stained blue with DAPI. The expressed proteins are indicated for each panel at the left of the figure. (Adapted with permissions from ref 32 Copyright © 2010 by the authors).

The IC-Tagging system is a molecular tagging technology credited with multiple applications. In this thesis we explore three different potential applications in protein tracking and int the therapeutic field.

First, an innovative sensor was designed to monitor protein retro-translocation in vitro, providing key insights into this cellular process. Additionally, the therapeutic potential of the system was investigated through the development of a vaccine candidate for immunotherapy in the B16-OVA pseudo-metastasis model, that triggers an effective immune response. Finally, a prototype vaccine for enveloped viruses was designed, opening new possibilities in the field of viral vaccination.

These advancements highlight the versatility of IC-Tagging in both basic research and biomedical applications.